Texas A&M University
Mechanical Engineering Department
Turbomachinery Laboratory
Tribology Group

A Shimmed Bump Foil Bearing: Measurements of Drag Torque, Lift Off Speed, and Identification of Stiffness and Damping Coefficients

TRC-B&C-01-2014

Research Progress Report to the TAMU Turbomachinery Research Consortium

A Research Progress Report

By

Joshua David Norsworthy

Research Assistant

And

Luis San Andrés

Mast-Childs Tribology Professor

Principal Investigator

May 2014

Shimmed Bump-Type Foil Bearings For Oil-Free Turbomachinery

TRC Project, TEES # 32513/1519 F3

Executive Summary

This report presents measurements characterizing the static and dynamic performance of a BFB configured with shims of two thicknesses (30 μm and 50 μm). Parameters of interest include drag torque, lift off speed, and the estimation of force coefficients of a BFB with shims (30 μm and 50 μm) and compares those results to those of the original BFB (without shims).

Drag torque measurements during shaft acceleration tests up to 50 krpm show that lift off speed of the original bearing and the shimmed bearings increases linearly with specific load (*W/LD*). The bearing with 50 μm shims has a lift off speed slightly higher than the original bearing while the bearing with 30 μm shims has a lift off speed comparable to the original bearing. The bearing with 50 μm shims lifts off at ~ 25 krpm while the original bearing and the bearing with 30 μm shims lift off at ~20 krpm (both under a specific load *W/LD*~ 20 kPa). The peak friction factor during rub condition ($f=T/RW$) for the original bearing (f~0.3) is constant with specific load (*W/LD*), while the bearings with shims show larger friction factors that decrease with specific load (*W/LD*). Once airborne, the original bearing and the shimmed bearings show similar (within 15%) friction factors that decrease with increasing specific load.

The bearing force coefficients are estimated over a frequency range of 200-450 Hz, under a specific load ~14.3 kPa. The bearing displacement amplitude (20 μm) is small compared to the nominal radial clearance (120 μm). The shims have an unremarkable effect on the bearing direct stiffness coefficients. The cross coupled stiffness and damping coefficients are smaller than the direct ones for the original and shimmed bearings. The shims significantly increase the direct damping coefficients (especially in the static load direction). The bearing loss factor (γ~0.39-0.48) is largely unaffected by excitation frequency and shim thickness. Evidently, shimmed bearings dissipate the same amount of mechanical energy as the original bearing (without shims).

Measurements of the TC shaft vibration conducted as the shaft operates at 50 krpm (833 Hz) show that even without significant changes in the bearing stiffness due to the shims, the shimmed BFB are able to reduce subsynchronous whirl motions of the TC shaft.

Shimming, therefore is a simple, economical way of increasing damping in BFBs thereby improving rotordynamic performance. Shimming does however offer some undesirable characteristics such as higher startup torque requirements. Note however, that once airborne, the drag power losses of a shimmed BFB are similar to those of the original bearing.

Table of Contents

Measurement of Drag Torque, Lift Off Speed, and Identification of Frequency Dependent Stiffness and Damping Coefficients of a Shimmed Bump-Type Foil Bearing

Luis San Andrés and Joshua Norsworthy, May 2014

Page

List of Tables

Page

List of Figures

Page

Nomenclature

$a_{\underline{X}(t)}, a_{\underline{Y}(t)}$	Bearing accelerations along $\underline{X}$ and $\underline{Y}$ directions [m/s^2]
$\bar{A}_{\underline{X}(\omega)}, \bar{A}_{\underline{Y}(\omega)}$	DFT of $\underline{X}$ and $\underline{Y}$ bearing accelerations [m/s^2]
$C_{\alpha\beta}$	Damping coefficients; $\alpha, \beta = X, Y$ [Ns/m]
c_{nom}	Nominal radial clearance [m]
D	Top foil (bearing) diameter, $D = 2 \times R$ [m]
D_A	Inner diameter of the assembled bearing [mm]
D_o	Bearing cartridge outer diameter [mm]
D_I	Bearing cartridge inner diameter [mm]
D_s	Shaft outer diameter [mm]
E	Top foil elastic modulus [Pa] or [N/ m^2]
f	T/WR. Drag or friction factor [-]
F_i^j, i,j = $\underline{X}, \underline{Y}$	DFT amplitdues of the excitation forces [N]
F_o	Excitation force at the lowest excitation frequency [N]
F_s	Applied static load [N]
ΔF	Time rate of change in the excitation force [N]
$\{H_{\alpha\beta}\}_{\alpha\beta=X,Y}$	$K_{\alpha\beta}+j\omega\, C_{\alpha\beta}$. Bearing impedances [N/m]
h	Gas film thickness [m]
i	Imaginary unit, $\sqrt{-1}$
$\{K_{S\beta}\}_{\beta=\underline{X},\underline{Y}}$	Squirrel cage stiffness coefficients [N/m]
$K_{\alpha\beta}$	Stiffness coefficients; $\alpha, \beta = X, Y$ [N/m]
K_{eq}	Equivalent stiffness [N/m]
L	Bearing axial width [mm]
L_T	Torque lever arm [mm]
M_B	Mass of the bearing [kg]

M_s	Estimated system mass (Bearing + squirrel cage) [kg]
N_B	Number of bumps [-]
P	Hydrodynamic pressure in gas film [Pa]
P_a	Ambient pressure [Pa]
P_r	Contact pressure [Pa]
R	Rotor radius [m]
T	δ K_s L. Drag torque [Nmm],
$T_{breakaway}$	*Breakaway* drag torque [Nmm]
t	Time [s]
t_t	Top (thin) foil thickness [m]
W	Net static load [N]
W_B	Bearing weight [N]
X,Y and $\underline{X}$,$\underline{Y}$	Coordinate system for the inertial axes [m]
x', y'	Bearing displacements relative to the journal [m]
$\bar{x}'_{(\omega)}, \bar{y}'_{(\omega)}$	DFT of bearing $\underline{X}$,$\underline{Y}$ displacements relative to the journal [m]
γ	Structural loss factor [-]
θ	Top foil angular coordinate [rad]
θ_p	Angular distance between shims [rad]
μ	Gas viscosity [Pa-s]
υ	Poisson's ratio [-]
τ	Shear stress [N/m^2]
φ	Angle of rotation from X to $\underline{X}$ axes
Ω	Rotor speed [krpm]
ω	Excitation frequency [rad/s]

ACRONYMS

DFT	Discrete Fourier Transform Operator
EOM	Equation of Motion
BFB	Bump type gas foil bearing
TC	Turbocharger

TS	Torque screwdriver

Introduction

Gas foil bearings (GFBs), in particular bump type foil bearings, provide reliable, low friction support to high-speed micro turbomachinery (<400 kW) [1]. Figure 1 presents a schematic view of a typical bump type foil bearing (BFB) comprised of one or more bump foil strip layers, a top foil, and a bearing cartridge. A spinning rotor pulls gas by viscous shearing into the wedge formed by the rotor outer diameter and the bearing inner surface thus generating hydrodynamic pressure that lifts the rotor from contact with the bearing. The thin gas film allows for no wear on the rotor and inherently offers lower drag power than oil lubricated bearings due to the low viscosity of the working gas. The load support is due to reaction forces provided by the gas film and are transmitted to the bump foil structure. Adequate mechanical energy dissipation, arising from the dry friction from the relative motion of the bump foil strip with both the top foil and the bearing cartridge, is critical for the stable operation of a rotor-bearing system (RBS).

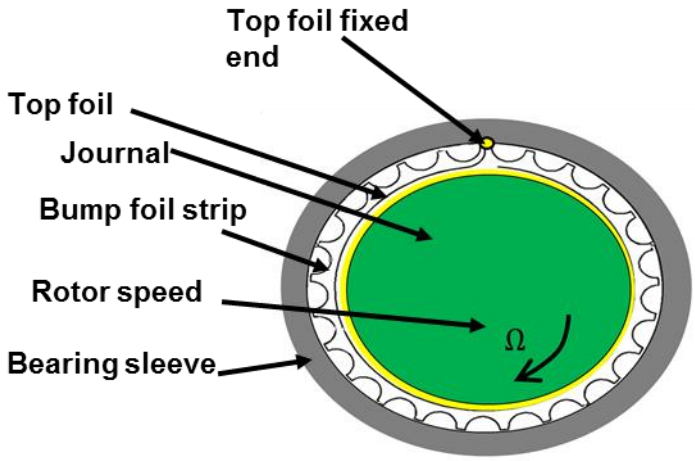

Figure.1 Schematic representation of a first generation bump-type foil bearing.

BFBs typically come in three variations termed generation I, II, and III bearings[1]. Chen *et al*. [2] and DellaCorte *et al.* [3] detail the manufacturing procedures for the construction of the bump foil strip and top foil of generation I and II BFBs The simplest BFB, a generation I type, contains a single bump foil strip as depicted in Figure 1. A generation II bearing contains various separate bump foil strips that line around the

[1] The design of generation III BFBs is patented, and in many situations, remains proprietary information.

bearing inner surface. Multiple bump foil strips create axially and circumferentially varying stiffness and damping characteristics. Generation III GFBs include complex arrangements of multiple bump foil strips along and around the bearing inner surface to further tailor the bearing stiffness and damping characteristics[2].

BFBs are applied routinely in aircraft Air Cycle Machines (ACMs). In a more recent laboratory setting, gas foil bearings have proven reliable support elements for automotive turbochargers [4,5]. A low drag power loss, tolerance to misalignment, and reliable high temperature operation are advantages that GFBs offer to microturbomachinery [1]. However, rotors supported on BFBs are known to display large subharmonic motions [6].

The stiffness and damping coefficients of the elastic bump foil strips largely determine the rotordynamic performance and stability of a rotor supported on gas bearings. As shown in Refs.[4,6]; mechanical preload, through the placement of metal shim strips axially along the interior of the bearing, effectively increases the onset rotor speed of instability and decreases the magnitude of subsynchronous vibrations in BFB supported rotors. Shimming is a simple, low cost technique to reduce large amplitude subsynchronous whirl motions in RBSs, thereby improving their rotordynamic stability.

The present work will advance prior research by characterizing the performance of shimmed BFBs through the identification of rotor lift off and shut down events as well as the identification of frequency dependent force coefficients while airborne (with journal rotation).

Literature Review

Designers and manufactures of advanced turbomachinery seek operation at increasingly higher speeds, with lighter and more compact units with increased reliability (fewer moving parts), thus making gas film lubrication preferable over traditional oil lubrication. The low viscosity of a gas inherently reduces the load capacity of gas lubricated bearings when compared to oil lubricated bearings. However, the

[2] Gas lubricant leaking from the edges of the bearing reduces the hydrodynamic pressure leading to a lower load capacity and bearing stiffness [1]. Modifying the bump foil structure allows the bearing design to maintain an adequate minimum film thickness throughout its operation, while minimizing gas leakage from the edges of the bearing, thereby improving the bearing stiffness and load capacity [1]

advantage of eliminating an oil supply system and the ensuing lower drag power losses make gas bearings a desirable alternative in lightly load turbomachinery [1].

Block and Van Rossum [7] introduced the first compliant surface (foil) bearing in 1953. Note that the first foil bearing does not contain an elastic “bump” undestructure; it simply contains a top foil. The bearing compliance aided in solving issues related to high temperature and high speed operation by tolerating thermal and centrifugal expansion of a rotor. By tolerating misalignment and allowing larger film thicknesses, the compliant support also offered an improved load capacity and reliability over that of a fixed arc bearing,.

The forced performance of BFBs encompasses the bearing load capacity, drag torque, rotor lift off speed, as well as the force coefficients (stiffness and damping); all of which are affected by the physical properties and geometry of the bump foil complaint understructure. The bump foil strip, usually a corrugated plate, is idealized as discrete elastic spring elements. The analysis of GFBs is complicated due to the interaction between the fluid film, and the deformation of the compliant foils (solid mechanics), plus the complex nature of dry friction systems. Currently, computational models of GFBs are capable of reliable and accurate predictions; however, the actual implementation of GFB is limited and relies upon extensive trials.

A critical review of the recent experimental work seeking to characterize and predict the performance of gas foil bearing (GFB) technology follows. The first section reviews the literature that pertains to the effects of environmental conditions (pressure, temperature, lubricant density, etc.) on BFB load capacity. The second section details literature pertaining to foil bearing rotordynamic force coefficients (with and without journal speed). The third section discusses the literature pertaining to transient rotor start up events, i.e., drag torque and lift off and shut down events. Finally, the fourth section details the performance characteristics of rotors supported on gas foil bearings.

The load capacity of bump foil bearings

The structural properties of the spring structure greatly affect the BFB static and dynamic forced performance. Parameters affecting the bearing load capacity include the bump foil geometry and materials, as well as the environment temperature and pressure.

In 1982 Heshmat *et al*. [8] showed that the bump foil of a BFB can be tailored to enhance its load capacity and rotordynamic stability. The bump foil strip layer of a generation I foil bearing is split into multiple strips axially that stretch circumferentially, effectively turning a generation I bearing into a generation II bearing. The bearing top foil is also sputter coated with a thin layer of copper and then heat treated. Splitting the bump foil strip layer allows for axially varying stiffness characteristics while coating the bearing with copper increases the damping properties. The generation II bearing shows a 60% increase in load capacity over an uncoated bearing.

In 1994 Heshmat [9] measured the load capacity and static load-deflection behavior of a generation II bearing (L=31mm, D=35mm). The static load versus deflection behavior is highly nonlinear with hysteresis loops evidencing mechanical energy dissipation. Alas, the dissipated mechanical energy is not quantified. The author reports that the bearing with an axially varying stiffness (generation II) is able to support a load of 727 N (673 kPa specific load) at a rotor speed of 132 krpm, which is a two-fold improvement over generation I bearings. The introduction of axially and circumferentially varying stiffness characteristics marks a dramatic step in the evolution of BFBs.

Environmental conditions, such as temperature and pressure, affect the physical properties of a bump foil strip and the top foil. Also note that temperature and pressure also alter the density and viscosity of the gas lubricant. Bruckner and Puleo [10] investigate the effects of temperature and pressure on the load capacity of a 35 mm diameter by 27 mm long generation III foil bearing. The test pressure range is 0.1- 2.5 atm and the temperature increases up to 500°C. Note that the bearing inner surface is uncoated however the shaft surface has a proprietary coating. The bearing load capacity is found to increase with increasing gas pressure, and to decrease with an increasing gas

temperature. Note that an increase in temperature causes an increase in the gas lubricant viscosity. Since the hydrodynamic gas film pressure is proportional to lubricant viscosity, the bearing load capacity should increase with temperature.

The observed behavior of the load capacity with respect to increasing temperature reported in Ref.[10] is attributed to a softening effect observed in the bump foil layer at high (~500°C) temperatures. Below 0.5 atm (a mild vacuum) the load capacity drops steeply, indicating a "starved" gas bearing, i.e., when the lubricant density is too low (too few gas molecules) for the bearing to support a load. Ref. [10] demonstrates that GFBs fail to provide adequate load support when operating at pressures below ambient.

In an effort to encourage the implementation of gas foil bearings, DellaCorte [11] presents a "Rule of Thumb" (ROT) for the prediction of BFB load capacity. The ROT, $W=D_o\,(L \text{ x } D)(D \text{ x } \Omega)$, relates the bearing load capacity (W) to the bearing projected area (L x D), and (two times) the surface velocity (D x Ω). D_o is an experimentally determined load capacity coefficient. For example a generation III bearing has a load capacity coefficient (D_o) four times larger than that of a similarly sized generation I BFB operating at the same shaft speed. The ROT is based on extensive empirical evidence from many types of BFBs (generations I, II, and III), as well as multileaf type gas journal bearings. However, the ROT is over ten years old, and ignores critical bearing operating conditions including the environmental pressure, and temperature.

Despite the advances and steady improvements in static load capacity, BFBs still remain a highly specialized technology with few applications. As designers of advanced turbomachinery seek to support larger loads at higher shaft speeds, some of the characteristics of foil bearings present challenges. Each bump foil bearing is highly engineered, not a ready off the shelf item, and leads to scalability issues. DellaCorte and Bruckner [12] discuss the current state of the art and future challenges for oil free turbomachinery. While the operating minimum film thickness increases with rotor speed and decreases with applied load, the authors argue about practical upper and lower bounds to the film thickness. The viscous drag power loss in BFBs is dissipated as heat; a fraction is carried by the gas film, and the rest is conducted into to the rotor and top

foil. The bearing top foil, being thin, is susceptible to thermal distortions brought on by increasing the shaft speed and static load, thus eventually causing rubbing. This is the lower bound of the film thickness, i.e., the smallest film thickness that is maintained for operation without contact, at a given speed and load.

Remarkably, there exists an upper limit to the film thickness or a maximum film thickness. Recall that a minimum film thickness is needed to lift the rotor. DellaCorte and Bruckner [12] note a maximum film thickness as that above which the gas lubricant leaks from the bearing edges, effectively reducing the hydrodynamic pressure that keeps the rotor afloat. DellaCorte and Bruckner [12] report experimental results for a generation I BFB identifiying the upper and lower bounds to the film thickness in a as 25μm and 5μm, respectively.

According to the DellaCorte's ROT for bearing load capacity [11], gas foil bearings are capable of supporting business jet class turbofan engines and (with increases in bearing diameter) large size compressors (with rotors weighing ~ 2400-9800N). The author notes that the load capacity does not truly limit the implementation of gas foil bearing technology. The authors suggest the limiting factors for the scaling of gas foil bearings are the bearing structural properties (stiffness, damping), and the stresses and strains on the rotor due to high shaft speeds (which cause rotor growth and distortions). Ultimately, Ref. [12] suggests hybrid bearings as the next step in the evolution of the BFB. Hybrid bearings would utilize air pressurization or electromagnetic technology as a means of increasing damping (when crossing critical speeds), and eliminating rotor wear from rubbing during start and stop.

Bump foil bearing force coefficients

Structural force coefficients (no journal rotation)

Bearing force coefficients, stiffness and damping, are critical mechanical parameters that determine its ability to control rotor vibrations. Note that each BFB is custom built and, as a result, even similar sized BFBs may show different stiffness and damping properties as well as load capacity [1]. The variability in BFB performance complicates

the bearing selection process, making BFB implementation, based solely on predictions and design guidelines, unlikely to succeed. In actuality, the successful implementation of GFBs relies on the use of design guidelines and ROTs, in conjunction with extensive experimentation. DellaCorte *et al*. [1] introduces a simple, empirically derived "rules of thumb" or guidelines for the prediction of stiffness and damping in BFBs, as they did in Ref. [9]. A BFB's stiffness (K) and damping (C) range from 2500-7500 (L x D) lb_f/in^3 and C~ 0.1-10 (L x D) $lb_f/in./in^2$ respectively. Note that these ROTs are not a function of surface speed, like the ROT for load capacity [10]. This shows one of the inadequacies of the ROT, as the stiffness and damping properties of a BFB change greatly with the operating rotor speed and the excitation frequency. In actuality, radial bearings are two degrees of freedom mechanical elements best characterized by four stiffness and four damping coefficients, all depending on the excitation frequency, rotor speed and whirl (excitation) frequency, as well as the rotor displacement amplitude [1,8,12,13].

Kim *et al*. and San Andrés *et al.* [13-16] identify the frequency dependent force coefficients of the BFB understructure without journal rotation. Kim *et al.* [12] investigate the effects of temperature and excitation frequency on the structural force coefficients of a generation II BFB. The structure of the BFB contains multiple arcuate bump strips that line the inner surface of the bearing cartridge. Dynamic load tests, conducted with single frequency load excitations, show that the BFB structural stiffness increases (up to 57%) with increasing excitation frequency (~40-200Hz) and dynamic load amplitude (~13-31N) and decreases (by 58%) with an increasing operating temperature (~22-188°C). The increase in stiffness is due to the bumps sticking during loading (regions where the bump displacement does not change under changes in load, which is typical of systems with dry friction). The stiffness of the BFB decreases with an increase temperature due to an increase in the radial clearance. The damping coefficients decrease significantly with increasing excitation frequency and shaft temperature.

Rubio and San Andrés [14, 15] conduct an extensive investigation on the structure of BFBs (without journal rotation). Ref. [14] evaluates the effects of bump geometry, preload, bearing angular orientation and dry friction coefficients on the structural

stiffness of a generation II BFB. Increasing the shaft diameter effectively introduces a mechanical preload into the bearing. Experimental results show that bearing structural stiffness increases nonlinearly with shaft deflection and mechanical preload (shaft diameter). A simple predictive tool, based on Iordanoff's equations for bump stiffness [16] and neglecting the interaction of adjacent bumps, delivers predictions that agree with the experimental results. Note also that increases in the dry friction coefficient cause the bump structural stiffness to increase.

Ref. [15] reports measurements of the BFB structural stiffness and equivalent viscous damping coefficient, or its equivalent dry friction coefficient, for operation under dynamic loads and moderate temperature. Mechanical energy dissipation or damping is critical for rotor bearing systems to safely traverse critical speeds (system natural frequencies). Coulomb dry friction, or viscous type damping, or structural type damping are models used to characterize the mechanical energy dissipated in a BFB structure.

Test results in Ref. [15] show that the equivalent viscous damping coefficient in a generation II BFB is strongly dependent (inversely proportional) on the excitation frequency and load amplitude. For load excitations well above the system natural frequency the test results show small viscous damping. The estimated dry friction force increases as the natural frequency is approached and also with dynamic load amplitude (up to 20 N). The bearing dry friction coefficient ranges from 0.05 to 0.2 for the applied load range, and remains uniform for excitation frequencies below the natural frequency. Above the natural frequency, the dry friction coefficient decreases at a steep rate due to dramatic reductions in the excitation load amplitude. Recall from linear vibrations theory that at the system natural frequency small loads can cause large displacements. Also note that a resonance around the natural frequency greatly affects the measurements, making the identification of viscous damping and or dry friction in this region unreliable.

Note that the mechanical energy dissipation in a BFB, a combination of hysteretic damping and dry friction, is best quantified by a structural loss factor.

Rotordynamic force coefficients (GFB operating with journal rotation)

During operation (journal rotation enabling lift off) the compliant bump foil understructure is in series with the gas film; which, thin by necessity, does contribute stiffness and damping force coefficients.

Matta *et al.* [17] describe a test rig for the identification of frequency dependent dynamic force coefficients of BFBs ($L=D$=30 mm) operating with journal rotation i.e., rotordynamic force coefficients. This test rig features an electric spindle which drives a shaft (30 mm) up to 60 krpm. Hybrid journal bearings support the shaft. The test bearing floats atop an overhung section of the test rotor and is supported by a soft elastic structure known as a "squirrel cage". The squirrel cage enables proper position of bearing on the journal. The mass and stiffness of the squirrel cage are estimated prior to dynamic load tests. Two orthogonally positioned electromagnetic shakes, suspended from a metal frame, apply dynamic loads while a spring is used to apply static loads. Typically dynamic load excitations containing a single frequency are employed in parameter identification; however, tests to cover a large frequency range can be time consuming and arduous. Other alternatives include sine sweep load excitations, a sinusoidal waveform containing a successive frequency range, and pseudorandom excitations containing equal amplitude sine waves of different frequencies. Matta *et al.* employ pseudorandom excitations (50-450Hz) in their dynamic load tests. The parameter identification consists of a nonlinear minimization of the first order transfer function (X/F i.e., displacement/force). In general results show that the bearing direct stiffness increases with excitation frequency (50-450 Hz), static load (15 N, 20 N), and speed (15-25 krpm). The damping coefficients are largely unaffected by static load but also decrease with excitation frequency and journal speed. In a subsequent paper, Rudloff *et al*. [18] also use two shakers to excite a floating bearing and. The study is quite comprehensive and shows that the force coefficients in generation I BFBs are strong functions of the excitation frequency (100-600Hz); however, the magnitude of the force coefficients is largely unaffected by rotor speed.

Chirathadam and San Andrés [19] report rotordynamic force coefficients (direct and cross coupled coefficients as well as the bearing loss factor) for a first generation BFB (L= 38.0 mm, D=36.5 mm) operating over a higher frequency range than in Ref. [15] (200-400Hz). Orthogonally mounted shakers excite a test bearing floating on a turbocharger driven rig. Measurements are conducted with a journal speed of 50 krpm (833Hz). The bearing motion amplitude is 25 μm and the bearing clearance is 0.11 mm. The direct stiffness coefficients of the BFB increase significantly with excitation frequency while the cross coupled stiffness coefficients are small (~0). The stiffness is higher in the Y-direction than the X-direction indicating some circumferential non uniformity in the bearing bump structure. The direct equivalent viscous damping coefficients also increase with excitation frequency. The authors note that the large magnitude forces applied to the bearing may play a role on the observed behavior. The cross coupled damping coefficients are also small. The bearing structural loss factor (γ) ~ 0.2-0.4, is largely independent of frequency. The loss factor (γ) is slightly higher when there is journal rotation than without.

Conlon *et al.* [20] compare the load capacity and force coefficients of similarly sized (L=D=70 mm) generation I and II bearings. A static load (W/LD~ 714 kPa) and dynamic loads (W/LD~ 91 kPa) are applied to both bearings. For static loads (with no journal rotation) the generation I bearing demonstrates higher structural stiffness coefficients than a generation II bearing. The freely moving bump foil strips of a generation II bearing are less constrained than the single bump foil strip of a generation I bearing, which leads to the lower structural stiffness shown in the generation II BFB. Load capacity tests (W/LD~41 kPa to 142 kPa) confirm that friction (power) losses increase with both static load and rotor speed. In general, the generation II BFB demonstrates a load capacity twice as high as the generation I BFB due to an improved pressure generation capability. While the static stiffness of the generation II bearing is lower than the generation I, the dynamic force coefficients (stiffness and damping) are significantly larger than those of the generation I bearing. The authors attribute this result to a higher

degree of nonlinearity in the force coefficients (stiffness and damping) of the generation II.

Measurements of Drag Torque

During rotor start up and shut down, due to the lack of a gas film, the rotor rubs on its bearings thus generating both heat and wear of components. Reducing the amount of time the rotor and bearing are in contact is important for the health of the rotor-bearing system. Rudloff *et al*. [18] report measurements of bearing start up torque and lift off shaft speed for a generation I BFB. Drag torque measurements are carried out for increasing specific loads (W/LD~7-35 kPa) and for increasing shaft speeds (15.6 krpm-35 krpm). There are two distinct regions of high drag torque, one associated with the rotor lift off and the other with touch-down. These regions have the highest drag torque due to the contact of the rotor with the bearing inner surface. Note that the drag torque upon either rotor start up or shut down is due to friction (between the rotor and bearing surfaces), while drag torque during operation is due to the viscous shearing of the gas film. The shaft lift off speed, typically between 2.7 krpm and 5 krpm, increases for increasing static loads.

Chirathadam and San Andrés [19] demonstrate that the drag power loss of a BFB (L/D~1) increases with rotor speed as well as increasing static load. Also Ref. [19] shows that the peak startup drag torque increases significantly with increasing static load. This result is not surprising given that static loads increase the friction force by increasing the contact pressure on the bearing inner surface.

Radil *et al.* [21] state that, in general, foil bearing failure is due in large part to thermal gradients brought on by a large viscous power loss. The authors present a 3D performance for a generation III BFB (L=35mm, D=27mm). The map relates the power loss, static load (max. 12 kPa), and operating speed (max. 55krpm) to aid in the design and selection of BFBs that operate away from thermal gradients that could lead to thermal runaway and ultimately bearing failure. The performance map is divided into two regions; one dominated by high loads and low shaft speeds (highly loaded region), and a lightly loaded region dominated by low loads and high shaft speeds. The authors suggest designing foil bearings to operate in the "lightly loaded" region of the

performance map. The lightly loaded region is a landscape where the film thickness supports the desired load while maintaining a low viscous drag power loss. Increasing the static load or decreasing shaft speed transitions the bearing to the highly loaded region and exposes the bearing to large increases in drag power loss. Foil bearings are susceptible to thermal runaway if operating in the highly loaded region. Ultimately, the performance map presents a tool for assessing if a generation III BFB is operating in a thermally safe region, and for determining a safety margin (allowable deviations in load or shaft speed) for the bearing to operate without risking failure.

Characteristics of rotors supported on foil bearings[3]

Research also focuses on studying the rotordynamic response of rotors supported on BFBs. Rotors supported on BFBs often show large and potentially catastrophic subharmonic whirl motions that may synchronize with the shaft speed or lock at a system resonant frequency misleadingly termed a rotordynamic instability [22, 23]. What follows is a brief review of the research pertaining to the persistence of subsynchronous whirl motions in BFB supported rotors.

Rubio and San Andrés [4] demonstrate that an increase in air feed pressurization reduces the amplitude of subsynchronous whirl motions in a rotor supported on BFBs and while it crosses system natural frequencies. External pressurization has no effect on the rotor synchronous motion amplitude response for operation well above critical speeds. A model of GFBs with side pressurization advanced in Ref. [4] predicts increased direct stiffness and damping coefficients as well as reduced cross-coupled stiffness coefficients as the feed pressure rises. Decreased cross-coupled stiffnesses increase the stability of rotor-bearing systems (RBS). Ref.[4] thus reports a method to reduce subsynchronous whirl motion amplitudes, thereby improving the stability of a RBS.

Kim and San Andrés [22] observe large amplitude (56 μm) subharmonic motions in speed coast down measurements of a rotor supported on BFBs. The whirl motions have a

[3] Portions of this section reproduced from Ref. [26] with permission.

frequency equal to 1/2 and 1/3 of the synchronous speed. Subsynchronous vibrations are ascribed to the nonlinear stiffness characteristics of the FB structure and are exacerbated by the presence of rotor imbalance. Kim and San Andrés note that the performance of RBS is largely dependent on the underspring structural characteristics and that foil bearings implementation into a RBS requires careful design with the entire system in consideration. Ref. [23] reviews the prior literature giving many more examples of RBSs displaying subsynchronous motion responses.

Heshmat *et al.* [8] propose a "three pad" bearing as a means enhancing the stability of BFBs operating at high speeds (<100krpm). The "three pad" bearing consists of three separate (equal length) sections of bump and top foils, each welded to the inner surface of the bearing cartridge. These sections featured bumps of varying pitch such that the stiffness increasing toward the weld location, thereby improving convergence and enhancing the generation of hydrodynamic film pressure. A rotor supported on a pair of three pad bearings shows stable operation up to 120 krpm with only small subsynchronous vibration components.

Kim and San Andrés [4] investigate the dynamic response of a rotor supported on mechanically preloaded (shimmed) foil bearings. The preload, introduced by affixing metal shims to the inner surface of the bearing cartridge, effectively introduces a hydrodynamic wedge that increases the hydrodynamic film pressure, leading to an increase in load capacity. The shims also create an angular stiffness gradient similar to that of the "three pad" bearing discussed above [9]. Rotor coast down responses are obtained for a rotor supported on both BFBs with and without shims. The response of a rotor supported on bearing without shims shows large amplitudes subsynchronous whirl motion (50 μm) for rotor speeds ranging from 27 krpm and 50 krpm with low feed pressure (0.35 bar). Under the same test conditions, the rotor supported on shimmed bearings shows smaller subsynchronous whirl amplitudes (20 μm) over a smaller shaft speed range (38 krpm to 50 krpm). The tests results in Ref. [4] demonstrate that mechanical preload reduces the severity of rotor subsynchronous whirl motions as well

as delays their onset. This information has the potential to extend the life of high-speed rotating machinery.

In Ref. [6] a pressurized air driven TC is revamped to incorporate one test BFB and a thrust foil bearing. Rotor speed coast down experiments (from 82 krpm) were conducted for bearings with and without shims. Rotor response data from waterfall plots demonstrate that a shimmed foil bearing delays the onset speed of subsynchronous whirl motions and attenuates their amplitude in the TC. The test setup is modified to allow the TC to be driven by a diesel engine. Results consistently reveal an improved rotordynamic performance for rotors supported on shimmed bearings. The authors note that TC rotor speed versus diesel engine speed data evidences that shimmed BFBs may have slightly higher drag power losses. No results of drag torque or power loss are presented in Ref. [6].

Schiffmann and Spakovsky [24] investigate (numerically) the role of underspring stiffness, structural damping, and static load on the rotordynamic stability of a rigid rotor supported on first generation BFBs. Ref. [24] reports that decreasing the bearing underspring compliance (increasing its stiffness) and increasing the static load can significantly improve the RBS stability (critical mass) and increase the onset speed of instability while structural damping has only a marginal effect. The authors note that an increased static load affects the fluid film thickness and the pressure distribution such that the ratio of cross-coupled and direct force coefficients (stiffness and damping) decreases thereby improving stability. The authors conjecture that tailoring the fluid film pressure profile by introducing shims at specific circumferential locations (selective shimming) is a means to increase the system onset speed of instability. Furthermore, Schiffman and Spakovsky produce design guidelines and optimum shim patterns (a certain set of shims, varying in thickness, at discrete angular locations) for improved FB stability. While these optimum shim patterns promise improved rotordynamic stability

for BFB supported rotors, a single shim pattern[4] requires shims of thickness ranging from 50% to 90% of the bearing clearance. The availability of shims of very particular thickness is limited, making the shim patterns rather impractical.

Sim *et al*. [25] in recent study, discuss the effects of mechanical preload on the rotordynamic performance of a rotor supported on a pair of three pad BFBs with large radial clearances (~ 150 μm).The three pad bearing features three pairs of independent top foil and bump foil strips, spanning 120° around the bearing cartridge circumference. the mechanical preload of the three pad bearing is defined as the distance between the lobe arc and the center of the bearing. Rotor speed up and coast down tests show that as the mechanical preload increases (from 0 to 100 μm) the onset speed of instability increases 62 krpm to 70 krpm (70 μm preload), until there is no sub synchronous motion (100 μm preload). Note also that the magnitude of both the synchronous and subsynchronous whirl motions decrease with increasing preload. The sub synchronous whirl motions occur between 120 Hz and 190 Hz which is identified as the location of a system critical speed. The subsychronous whirl motions are attributed to nonlinearities in the BFB sub structure. The rotordynamic performance of the three pad bearing is compared to a similarly sized single pad BFB (100 μm preload). The single pad refers to a bearing featuring the generation I foil structure fitted into a bearing cartridge with a tri-lobe shape profile. The single pad BFB shows the lowest onset speed of instability of all the tests bearings and preload conditions, and therefore has the least favorable performance. The authors predict the bearing force coefficients and show a strong stiffening effect with increasing preload and rotor speed. While the three pad bearing shows improved rotordynamic performance, its design is complex and requiring excessive engineering man hours to design and extensive testing to validate performance.

[4] Note that an optimization process determines the thickness and location of each shim that comprises the shim pattern in Ref. [24]. As a result, each shim pattern is customized for the particular bearing and its operating conditions.

Test Bump Foil Bearing

Two types of measurements are conducted on a generation I test BFB described below: (a) drag torque measurements during the rotor speed startup, speed shut down, and while operating at a constant speed (50 krpm) and (b) dynamic load tests to identify force coefficients.

A mechanical preload is added to the BFB structure by inserting shims of known thickness between the bearing cartridge and the bump foil. Figure 1 presents a schematic view of a typical BFB and a BFB with shims added at discrete circumferential locations.

Table 1 shows the dimensions of the test bearing, test shaft, and metal shims and Figure 2 shows a photograph of a bump foil bearing with a metal shim inserted between the bearing cartridge and the bump foil layers. During loading, the bumps atop a shim are compressed before other bumps since a shim pushes the bumps toward the rotor.

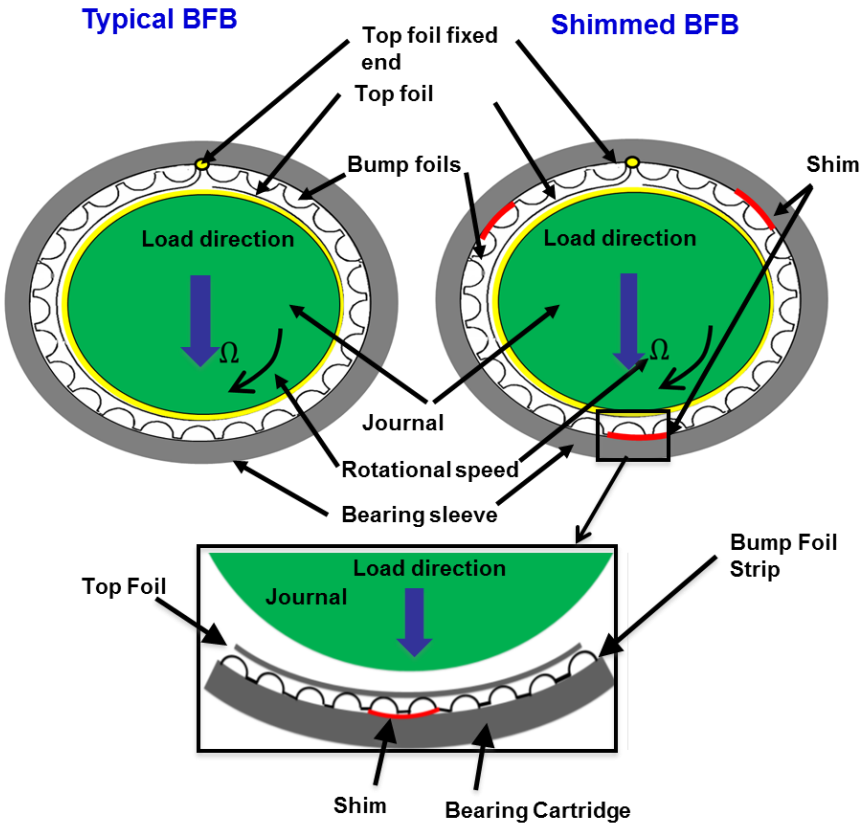

Figure 1. Schematic representation of a typical first generation bump-type foil bearing and a shimmed BFB. Inset shows a zoomed in view of the area around a shim.

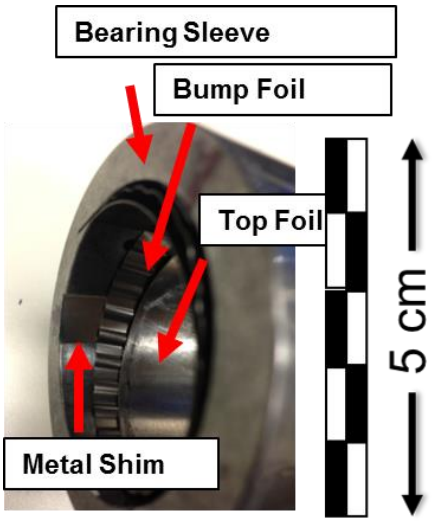

(a)

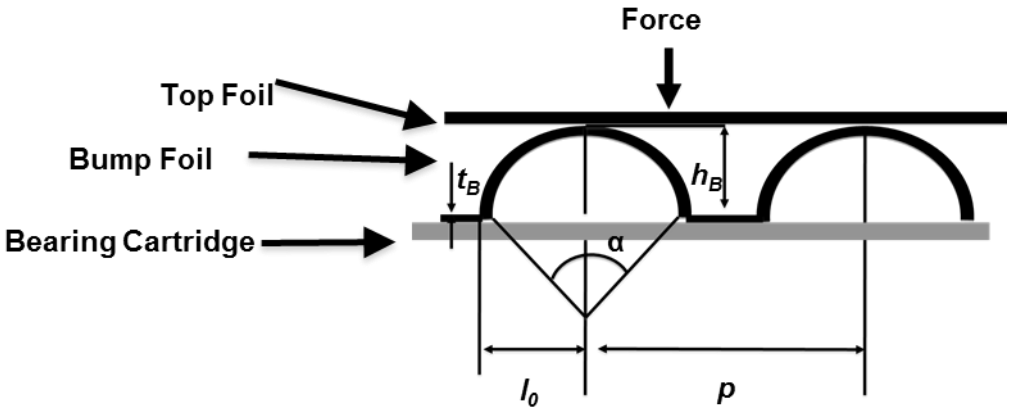

(b)

Figure 2. (a) Schematic view of a bump foil and geometric parameters, and (b) a photograph of a BFB with a metal shim layered axially through the bearing [5].

Table 1 Nominal dimensions of the test foil bearing and metal shims.

Parameters	Magnitude
Bearing cartridge outer diameter, D_O	50.74 mm
Bearing cartridge inner diameter, D_I	37.98 mm
Shaft diameter, D_s	36.5 mm
Bearing axial length, L	38.10 mm
Top foil thickness (Inconel X750), t_T	0.1 mm
Foil length , $2\pi D_I$	110 mm
Elastic modulus, E	214 GPa
Poisson's ratio, v	0.29
Number of bumps, N_B	26
Bump foil (Inconel X750)	
Thickness, t_B	0.112 mm
Pitch, s_0	4.5 mm
Length, l_B	2.5 mm
Height, h	0.50 mm
Elastic modulus, E	214 GPa
Poisson's ratio, v	0.29
Shim (AISI 4140)	
Length	38.1 mm
Thickness, t_s	0.050, 0.030 mm
Width	7.87 mm
Angular extent	11.8°
Elastic modulus, E	214 GPa
Poisson's ratio, v	0.29
Measured inner diameter of the FB (assembled), D_A	36.74 mm
Nominal FB radial clearance[5], c_{nom}	0.120 mm
Weight of test bearing and outer cartridge, W_B	10 N

The BFB[6] consists of a top foil and a single underspring layer with 26 bumps. Both foils, made of Inconel X750, are uncoated. The bearing fits into a steel cartridge that also hosts instrumentation.

[5] Determined from the bearing dimensions as $c_{nom} = 0.5\left(D_A - D_s\right)$ where D_A is the measured inner diameter of the bearing once assembled.

[6] The Korean Institute of Science and Technology (KIST) manufactured the BFB.

Figure 3 shows, for increasing shim thicknesses, the predicted bearing radial clearance relative to the nominal radial clearance (c_{nom}~120 μm) versus angular location. The clearance profile in a bearing with three equally spaced shims of known thickness, t_s, and nominal clearance, c_{nom}, is [4]

$$c_{(\theta)} = \left(1 - \frac{t_s}{2c_{nom}}\right) c_{nom} - \frac{1}{2} t_s \cos\left[\left(N_S\left(\theta - \theta_1 - \theta_p\right)\right)\right] \quad (1)$$

where θ is an arbitrary angular location, θ_1 is the angular location of the middle of a first shim (counter clockwise direction), N_s is the number of shims, and θ_p (~120°) is the angular space between shims. Figure 3 shows the bearing radial clearance relative to the nominal radial clearance (c_{nom}=120 μm) versus the angular location (θ) for instances two shim thicknesses (30 μm and 50 μm). The clearance in a bearing with shims is periodic resembling that in a tri-lobe bearing. For a bearing with both 30 μm shims and 50 μm shims, the clearance at the location of the shims reduces by 20% and 40%, respectively. The addition of increasingly thicker shims eventually would lead to a condition of interference fit of the bearing top foil with the rotor.

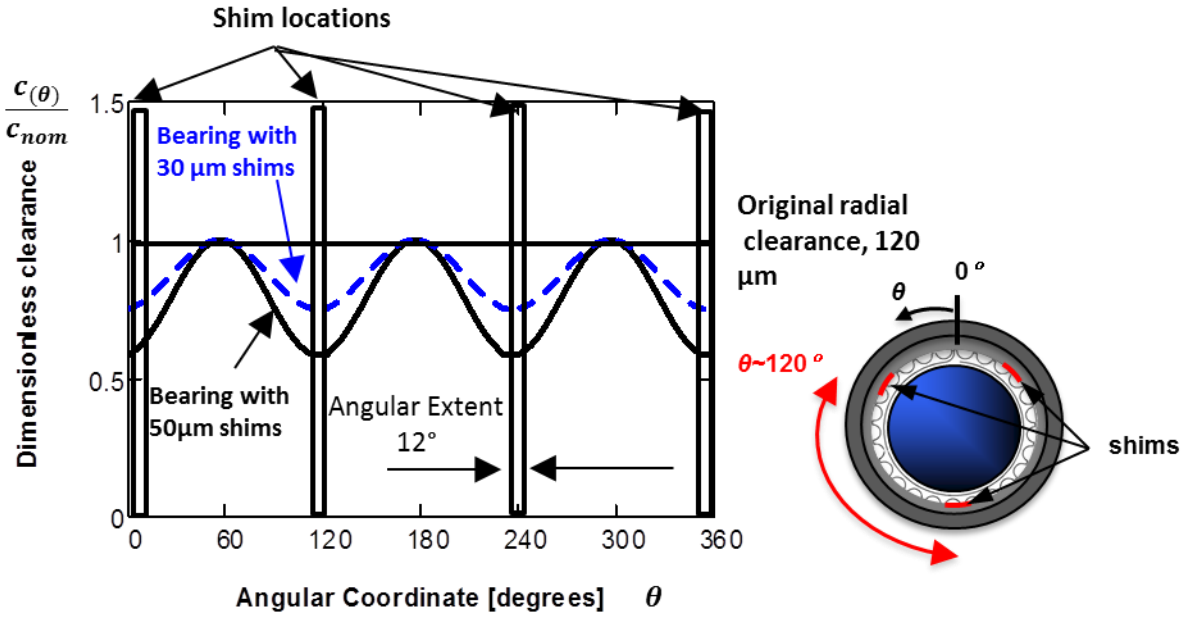

Figure 3. Dimensionless clearance profile of a bump foil bearing versus angular coordinates (θ) for two shim thicknesses (30 μm and 50 μm). Nominal radial clearance is 120 μm.

Measurement of Drag Torque in a BFB

During rotor speed startup and shut down, BFBs exhibit high drag torque due to rubbing contact with the rotor surface. Drag torque measurements aim to assess the effect of an applied static load (*W/LD*), and shim thickness (t_s), on the test element drag torque, friction factor, and bearing lift off speed. The drag torque is measured for two operating regimes; rotor speed startup (where dry friction sliding is prevalent) and rotor lift off, and airborne operation at a constant shaft speed.

Measurement of BFB *breakaway* torque

This section details the measurement of the torque needed to overcome the static friction due to contact between the rotor and bearing surfaces. This torque is termed as a *breakaway* torque. Figure 4 shows a photograph of the test setup used to measure the *breakaway* torque of the BFB. The bearing is rigidly held by a threaded steel rod and the rotor is manually rotated toward the top foil free end. An ad-hoc setup is assembled to apply vertical loads onto the BFB.

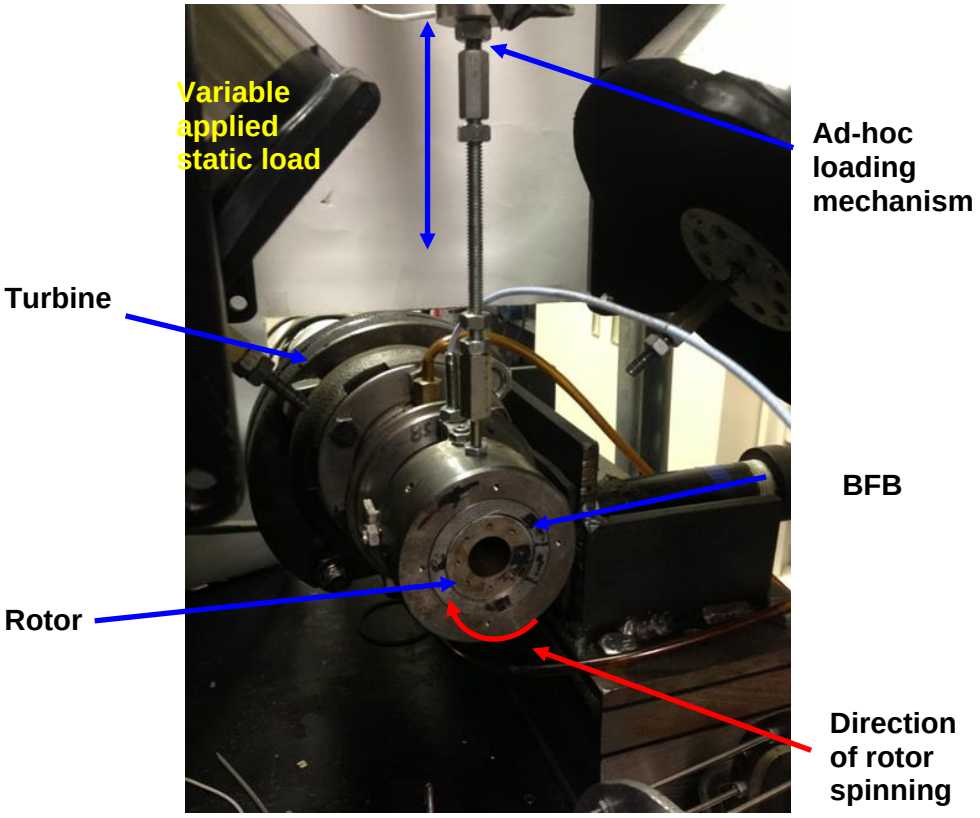

Figure 4. Photograph the test setup to measure *breakaway* torque in a BFB.

Figures 5 and 6 present schematic views of the BFB upon journal rotation. The vertical static load (W) pulls the rotor into contact with the bearing thus generating a contact pressure (P_r) on the bearing surface; ($W = \iint P_r R\cos(\theta) d\theta dz$). Note that θ is an angular coordinate around the surface of the circumference of the bearing, and z is a coordinate stretching axially. Also note that only one component of the contact pressure opposes the applied vertical load ($P_r\cos(\theta)$), while ($P_r\sin(\theta)$) when integrated over the bearing surface area, equals zero i.e., $\iint P_r R\sin(\theta) d\theta dz = 0$.

Drag shear stresses (τ) arise when the journal turns. The shear stress ($\tau \sim P_r$)[7] is prortional to the contact pressure (P_r), and when integrated over the bearing surface are, gives a drag torque ($T = \iint \tau R^2 d\theta dz$). Note that the local contact pressure (P_r), and shear stresses (τ) are vector quantities with directions as represented in Figure 6.

[7] Upon journal rotation (prior to journal lift off), the shear stress (τ) is due to friction between the shaft and the bearing inner surface. A simple balance of forces shows that $\tau = \frac{F_s}{A} = \mu_f P_r$ where μ_f is a coefficient of dry friction, F_s is a shear force, and A is the area over which the shear stresses act.

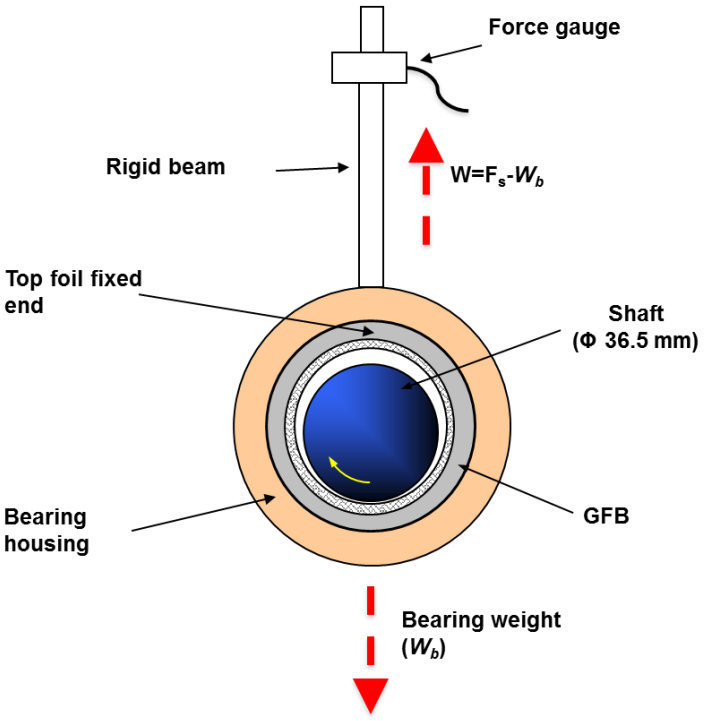

Figure 5. Schematic view of the test setup used to measure the *breakaway* drag torque of a BFB.

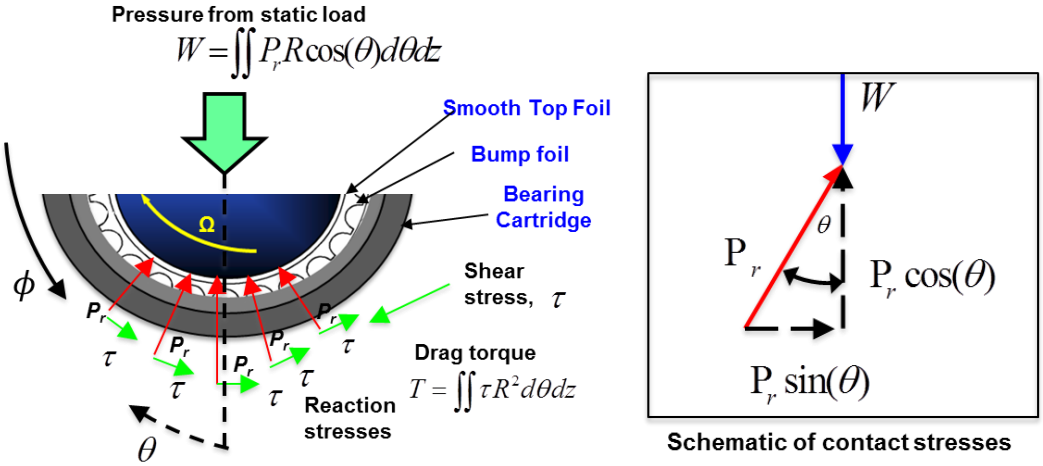

Figure 6. Schematic view of the contact stresses acting on the BFB understructure during loading and journal rotation.

A torque screwdriver (TS) (graduations: 56 N-mm, uncertainty: 28 N-mm), shown in Figure 7, is used to manually apply and measure the torque applied to the turbocharger (TC) shaft.

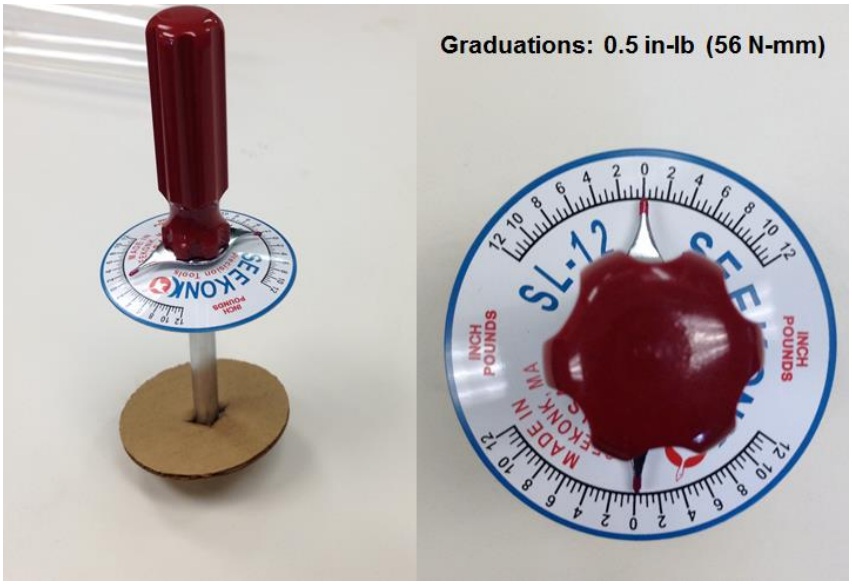

Figure 7. Photograph of the torque screwdriver.

The manually applied torque is increased until the journal turns inside the bearing. The torque is identified as a *breakaway* torque ($T_{breakaway}$). Note that the TC rotor is supported by oil lubricated ball bearings which provide an additional residual drag torque. However, this torque is small < 10 N-mm. Consult Appendix A for details.

Note from Figure 6 that the net static vertical load ($W=F_s-W_b$) is the applied static load (F_s) minus the bearing weight (W_b); while the applied torque (T_a) equals a dry-friction shear torque (T_{drag}) from the frictional contact from the BFB. Note also that the bearing foils are uncoated while the rotor surface is coated (25 µm thick) with thin dense chrome (TDC). Shims are introduced to the BFB, as discussed above, to add mechanical preload. The bearing clearance (without shims), as estimated from the bearing geometry, is ~ 120 µm (~4.7 mil) radially.

***Breakaway* friction factor of the original bearing and the bearing with shims**

Figure 8 shows the friction factor ($f=T/(RW)$) versus specific load (W/LD) for a bearing with shims of increasing thickness. Note that for specific loads below 10 kPa, the bearing friction factor decreases with specific load, and then is subsequently

constant. The friction factor increases with shim thickness. The bearing with 50 μm shims has a friction factor approximately 30% higher than the original bearing (i.e., without shims).

The increase in friction factor with specific load (*W/LD*) is due to the increase in the contact pressure (P_r) which increases the local shear stress ($\tau \sim \mu P_r$). Note that the top foil and bump foil deform (bend around the rotor) with the application of a static load. Increasing the static load thereby increases the area of contact between the rotor and the bearing which contributes to increasing the frictional shear stress. Increasing the mechanical preload increases the *breakaway* friction factor (*f=T/RW*).

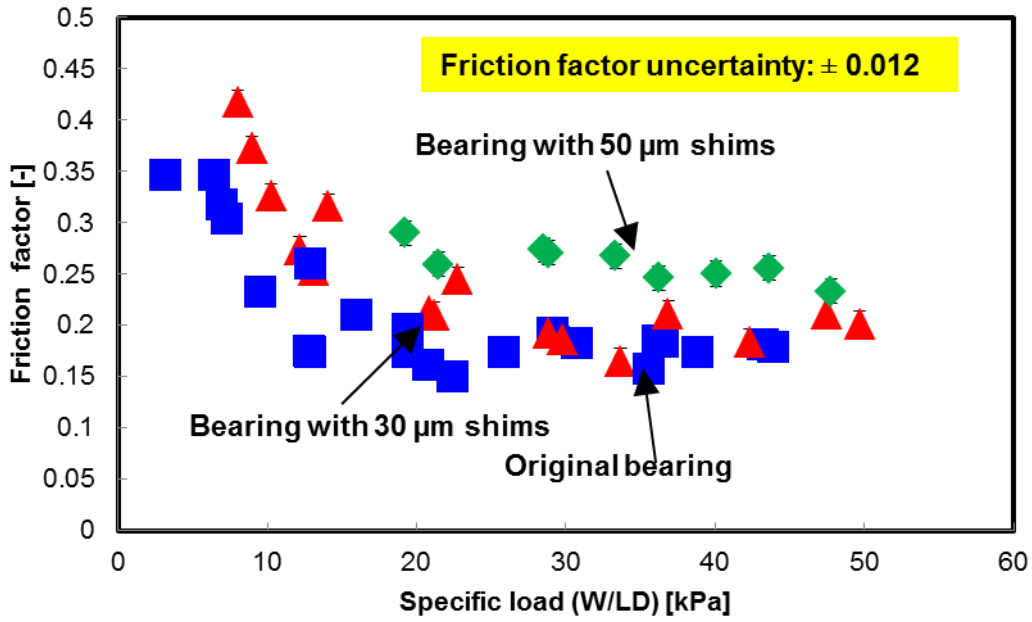

Figure 8. Friction factor (*f=T/WR*) derived from the *breakaway* drag torque versus specific load (*W/LD*) for the original bearing and a bearing with shims of thickness 30 μm and 50 μm. Stationary journal.

Test rig to measure the drag torque of a BFB atop a rotating shaft.

Figure 9 presents a schematic view of the test rig used to measure the drag torque of a generation I BFB. An ad-hoc apparatus featuring a series of ties wrapped around the bearing cartridge is assembled to apply vertical loads to the BFB. Journal rotation causes the lever arm to compress a calibrated spring. An eddy current sensor and an optical tachometer measure the journal rotational speed (Ω) and deflection of spring (δ),

respectively. The bearing drag torque $T=\delta K_s L$, with, K_s ~ 5.9 N/mm as the stiffness of the spring (uncertainty ±0.33 N/mm), and L_T (~152 mm) is the length of the lever arm. The raw drag torque data is rather noisy, thus every four torque data points are averaged to reduce scatter and smooth the results.

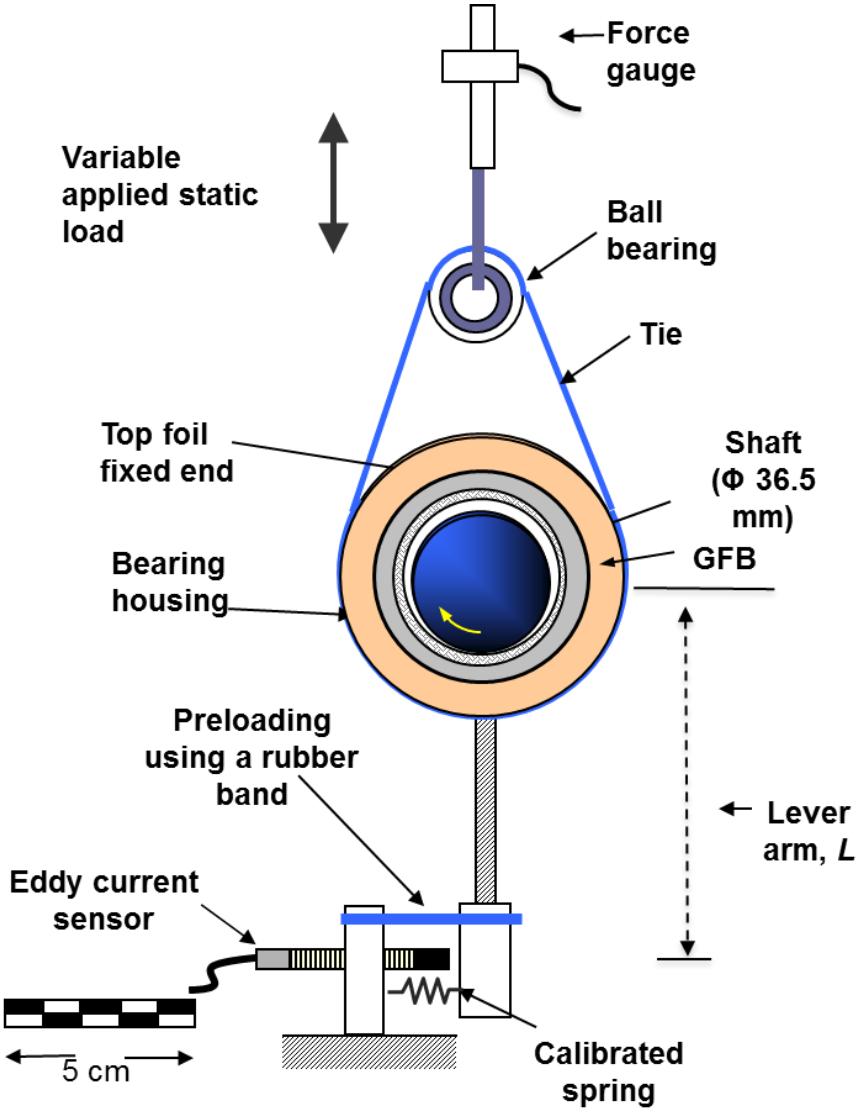

Figure 9. Schematic view of the test rig used to measure bearing drag torque [3].

Drag torque of a BFB without shims

Figure 10 shows the bearing drag torque and rotor speed versus time for the original bearing (with no shims) under a specific load *W/LD*~0 kPa. Note that there are two regions of large drag torque at low journal speeds near the journal speed start up and

shut down events. These regions of high drag torque reveal the drag torque required to both overcome dry friction between the bearing and rotor surfaces and then accelerate/decelerate the rotor. The steep drop in drag torque around 20 krpm indicates the rotor lift off rotational speed. The lift off condition denotes the transition to viscous drag as hydrodynamic pressure establishes the gas film separating the journal from the rotor (no contact) [1, 18-19,21]. Note that the drag torque during full film operation, termed as the airborne drag torque (~7 N-mm) is approximately 8% of the peak drag torque (~90 N-mm).

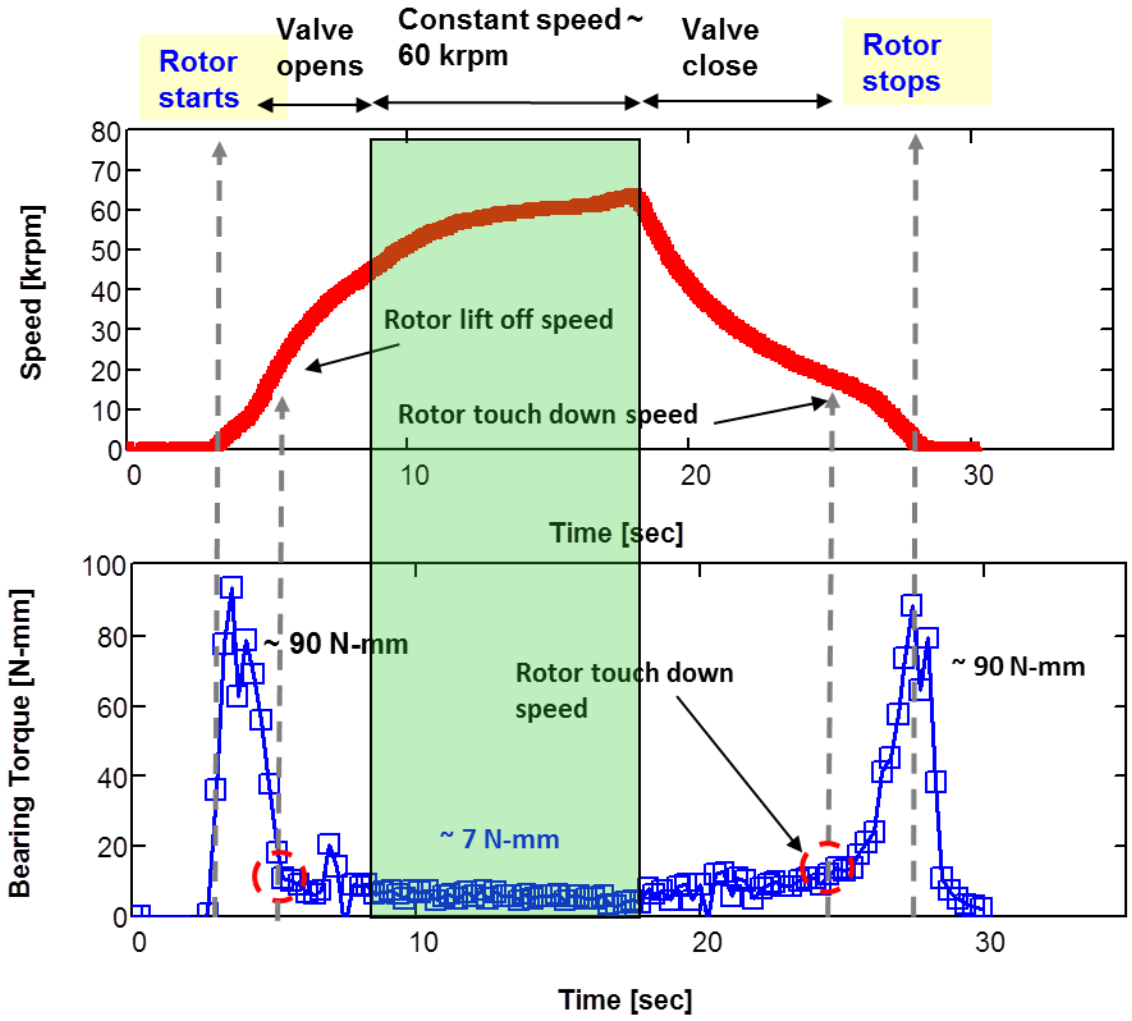

Figure 10. (Top) Bearing drag torque and (bottom) rotor speed versus time for a BFB without shims and for *W/LD* ~ 0 kPa.

For a bearing (without shims) with *W/LD* ~ 0 kPa, Figure 11 shows the bearing drag torque and rotor speed versus elapsed time as zoomed in the rotor speed startup region. Note that upon start up (once the rotor begins to spin) the equation of motion is

$$I\ddot{\theta} + T_{drag} = T_{drive} \tag{2}$$

where I is the rotor polar moment of inertia, $\ddot{\theta}$ is the acceleration of the rotor, T_{drag} is the drag torque featuring contributions from both friction and/or viscous drag, and T_{drive} is the torque applied to accelerate the rotor.

The peak startup torque to overcome static friction, or *breakaway torque*, occurs when the rotor begins to turn. Note that the *breakaway* torque (~ 40 N-mm) occurs at ~ 3s which corresponds to a torque that is not the max. torque (90 N-mm). The further increase in the torque is due to the journal accelerating while still in contact with bearing.

Importantly enough, the decrease in torque even as the rotor accelerates (between 4s and 5s in Figure 11) is due to the operator closing the air supply valve, thereby reducing the flow of compressed air supplied to the TC. This action keeps the rotor from reaching excessive speeds (>80 krpm)[8].

[8] To facilitate a expedite rotor lift off, the valve supplying air to the TC is opened rather wide, thus supplying more than enough flow to turn the turbine and accelerate the rotor. To prevent the shaft speed from reaching ~70 krpm, the valve is closed, thereby reducing the air supplied to the TC.

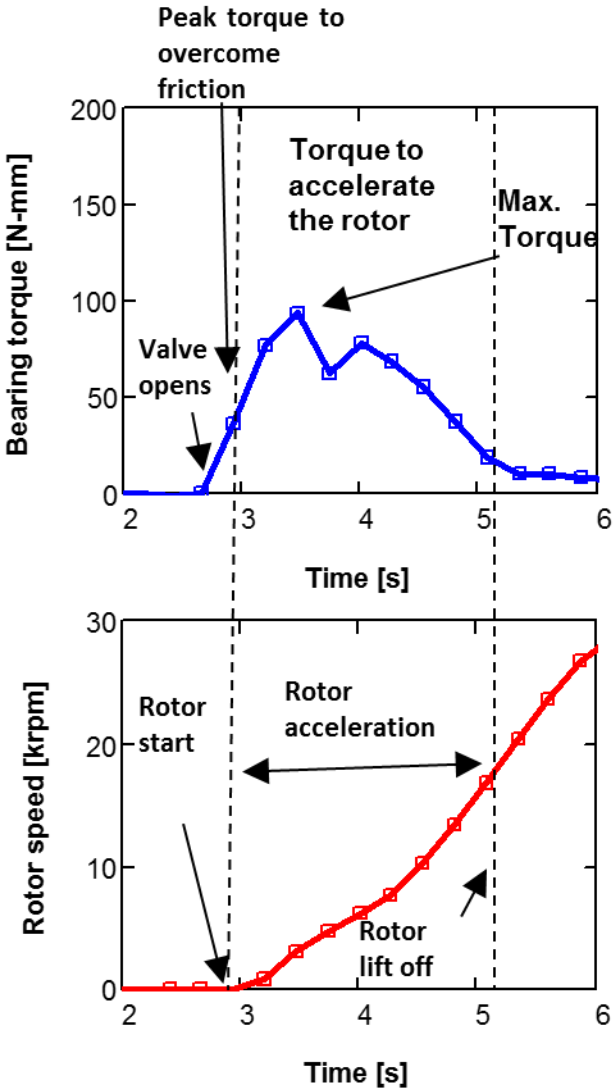

Figure 11. (Top) Bearing drag torque and (bottom) rotor speed versus time for a bearing without shims with *W/LD* ~ 0 kPa. Zoomed in on the rotor speed startup region.

Comparison of two methods of identifying the drag torque due to dry friction

Measuring the drag torque (T) during a rotor speed startup test and the *breakaway* torque ($T_{breakaway}$) presents two methods of identifying the drag torque due to rubbing contact that a bearing experiences. Clearly, recording the *breakaway* torque with a simple torque screwdriver is simpler and easier than driving the system to spin the rotor.

Figure 12 presents the bearing startup drag torque (T) and *breakaway* torque ($T_{breakaway}$), and the friction factor from the startup torque and *breakaway* torque versus specific load for the original bearing (without shims).

The drag torque (T) during startup and the *breakaway* torque dramatically increase with specific load (W/LD). In fact, the peak drag torque (T) during startup at the highest specific load (W/LD~20kPa) is 75% larger than at W/LD~0 kPa. The maximum variance in the peak start up torque measurements is ±5 N-mm. Interestingly, the startup friction factor ($f=T/RW$~0.3) remains constant with respect to specific load.

Note the friction factors identified by each method are quite similar for low loads (<10 kPa); however the difference grows with load. At specific loads W/LD>10 kPa, the friction factor ($f=T/RW$) during rotor speed startup is significantly higher (33%) than the *breakaway* friction factor ($f_{breakaway}=T_{breakaway}/RW$).

Tests with rotor speed at W/LD~20 kPa occurred after approximately 200 cycles of rotor speed startup and shut down. Post test inspection shows visible wear after only ~ 100 cycles of rotor speed startup and shut down procedures (consult Appendix B for details). Visible surface wear is likely to increase the friction factor. For example, Ref. [28] notes a 40% increase in the drag torque (and friction factor) due to surface wear and loss the of protective MoS2 coating in a (metal mesh) foil bearing.

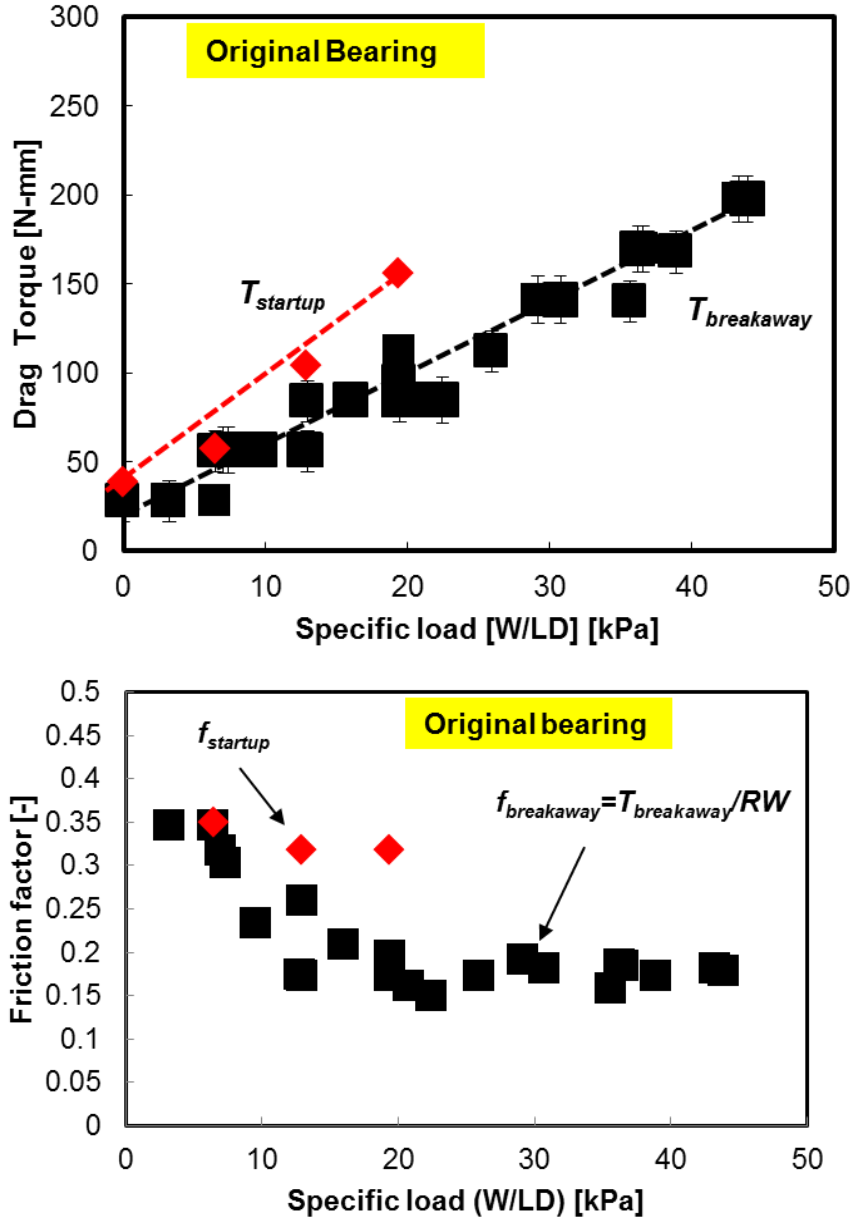

Figure 12. (top) Bearing drag torque(*T*) during speed startup and *breakaway* torque ($T_{breakaway}$) and (bottom) friction factor calculated from the start up drag torque (*f*) and *breakaway* torque ($f_{breakaway}$) versus specific load (*W/LD*) for the original bearing (without shims).

Drag torque for a shimmed BFB

Metal shims were added to the BFB according to the procedure described in the test bearing description. The metal shims effectively instill a mechanical preload (reduce the

clearance and minimum film thickness). This subsection details the effect of shimming on the torque in a generation I BFB during rotor speed startup, constant rotor speed operation, and rotor speed shutdown. The same experimental procedure, described in the section detailing the test rig to measure the airborne drag torque, is followed, and which consists of accelerating the TC journal to ~50 krpm. The test apparatus depicted in Figure 9 is used to record the bearing drag torque.

Figure 13 presents the peak startup torque (*T*) and bearing lift off speed versus static load for a bearing without shims and with shims. The bearing lift off speed is identified as the journal speed at which the bearing drag torque ceases to decrease further indicating that a minimum film thickness is generated, lifting the rotor from contact with the bearing.

The peak startup torque for the shimmed bearings increases with specific load and shim thickness (mechanical preload). The lift off speed for the original bearing increases with specific load (by 37%). As specific load (*W/LD*) increases, the hydrodynamic pressure needed to lift the bearing increases. High rotor speeds (~20 krpm) will generate a hydrodynamic pressure that lifts the rotor from contacting with the bearing, thus effectively creating a gas film thickness. To generate more hydrodynamic pressure the rotor must spin faster requiring a higher lift off speed. The tests are repeated three times for each static load. The maximum variance in the lift off speed measurements is ~3 krpm. While the lift off rotor speed for a bearing in the shimmed configurations increases with specific load (*W/LD*), the lift off speed for the bearing with 30 μm shims is 15% lower than that of the original bearing for all specific loads. The maximum variance in the lift off speed measurements for the shimmed bearings is ±2.5 krpm (also occurring at the max. specific load). Given the variance in the lift off speed measurement, the bearing with 30 μm shims show a lift off journal speed similar to the original bearing. The maximum variance in the peak startup torque measurements is 20 N-mm (which occurs at *W/LD*~20 kPa), however the average variance is ±5 N-mm (consult Appendix C for details on the uncertainty analysis).

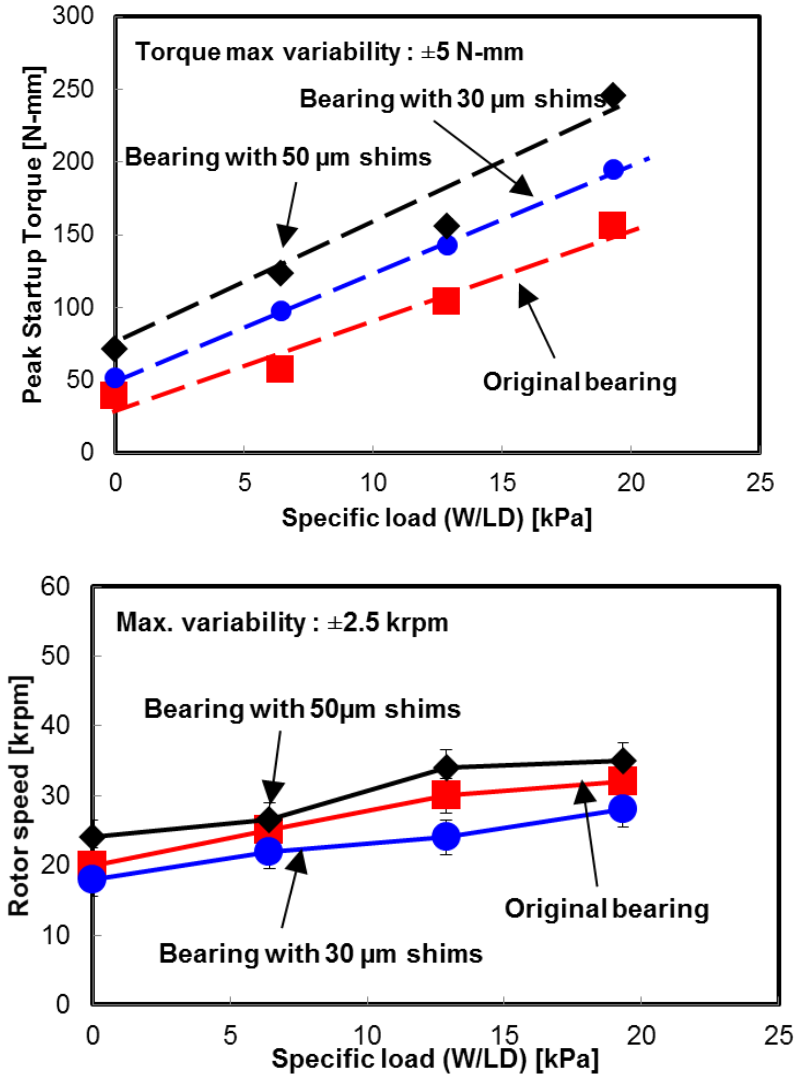

Figure 13. (top) Peak startup torque and (Bottom) lift off speed versus static vertical load for original bearing and bearing with shims of thickness 30 µm and 50 µm.

Figure 14 shows the friction factor (*f=T/(RW)*) derived from the peak startup torque versus specific load for a bearing with two shim configurations. The original bearing shows a friction coefficient $f \sim 0.30$. Also note that the friction coefficient for the original bearing does not change greatly with increasing specific loads. The friction factor for the bearings with shims is higher than the original bearing. The friction factor (*f*) increases with shim thickness and decreases with increasing specific loads. Note that at *W/LD*~20 kPa, the friction factor for the bearing with 50 µm shims is 40% higher than

the original bearing. Recall, from Figure 8, that the friction factor based on the *breakaway* torque shows that the bearing with 50μm shims has a friction factor ~34% higher than the original bearing.

Measurements from both methods (driving the TC shaft and measuring the *breakaway* torque) show roughly the same trend in the friction factor for the shimmed bearings. Recall from Figure 12, however, that the measurements from the two methods differ by 30% at *W/LD*~20 kPa.

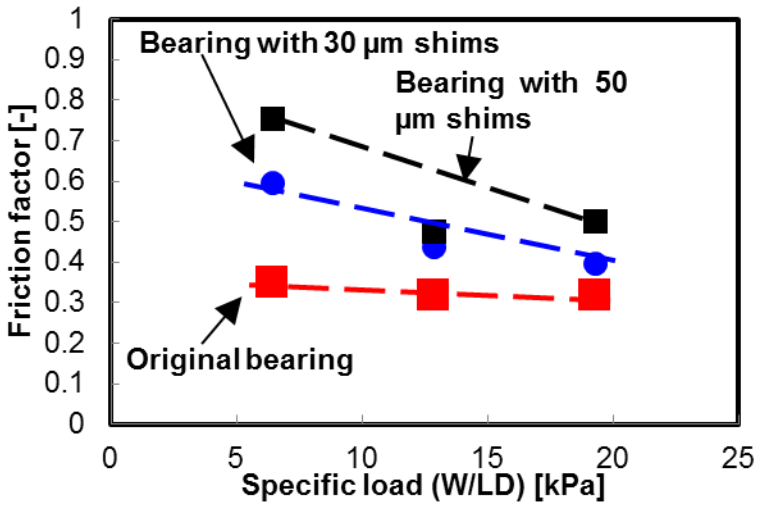

Figure 14. Dry friction factor versus specific load (*W/LD*) for the original bearing and the bearing with shim thickness of 30 μm and 50 μm.

Friction factor for a shimmed BFB while airborne (full gas film)

Figure 15 shows the friction factor ($f=T/(RW)$ versus rotor speed for the original bearing and the bearing with shims, all operating under various specific loads (*W/LD*~ 6 - 20 kPa). The friction factor of the bearing with 30 μm shims is approximately equal to that of the original bearing while the friction factor of the bearing with 50 μm shims is approximately 15% higher than that of the original bearing. While the shaft operates at 50 krpm, the static load significantly affects the friction factor. f decreases from 0.08 to 0.05 with a specific load increase from ~ 6 kPa to 20 kPa Once the rotor is lifted, the friction factor changes little with rotor speed. The uncertainty in the friction factor ($f=T/RW$) is ±0.008.

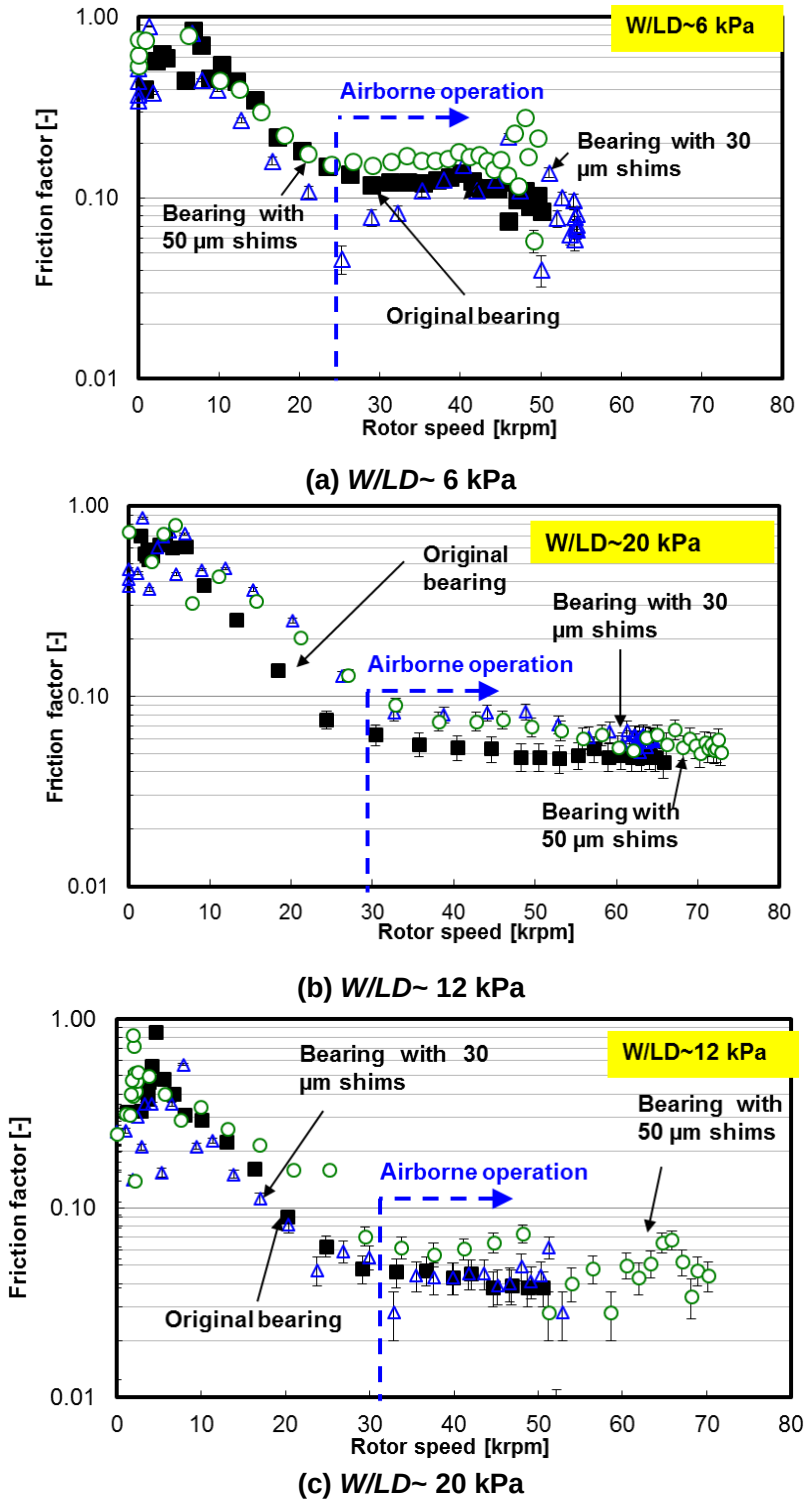

Figure 15. Friction factor (*f=T/(RW)* versus rotor speed (Ω) for a bearing with and without shims and specific loads (a) *W/LD*~6 kPa (b) 12 kPa and (c) 20 kPa. Measurements during rotor acceleration to airborne condition.

Identification of Rotordynamic Force Coefficients of a BFB with and without Shims

Bearing stiffness and damping coefficients largely determine the rotordynamic performance of BFB supported rotor-bearing systems. This section presents an experimental facility and parameter identification procedure for determining BFB force coefficients. A discussion follows on the effect of rotor speed (Ω), excitation frequency (ω), and on the force coefficients of a BFB assembled with various shim thicknesses (t_s)

Experimental Facility

Figure 4 shows the experimental setup for the dynamic load tests. The test rig is the same as used in Ref. [27]. The rig consists of a ball bearing supported turbocharger (TC) capable of shaft speeds up to 80 krpm. The compressor impeller end of the turbocharger is removed and replaced with an exposed over hanging shaft. A hollow journal (36.5mm OD) is press fit onto the shaft and secured with a nut. The test BFB is placed on the journal.

A squirrel cage, attached to a positioning table, supports the test bearing and helps to reduce misalignment of the bearing with the journal during loading. Two eddy current sensors record FB motions relative to the shaft, two accelerometers (mounted to the bearing cartridge) measure absolute acceleration, and dynamic loads cells record the excitation force. Two orthogonally positioned shakers (45° away from the vertical plane) apply sine sweep load excitations to the BFB and the resulting motions are recorded to extract dynamic force coefficients.

An in house computer data acquisition interface controls the dynamic load characteristics (amplitude and frequency) while the recording bearing relative displacements, acceleration, and applied loads.

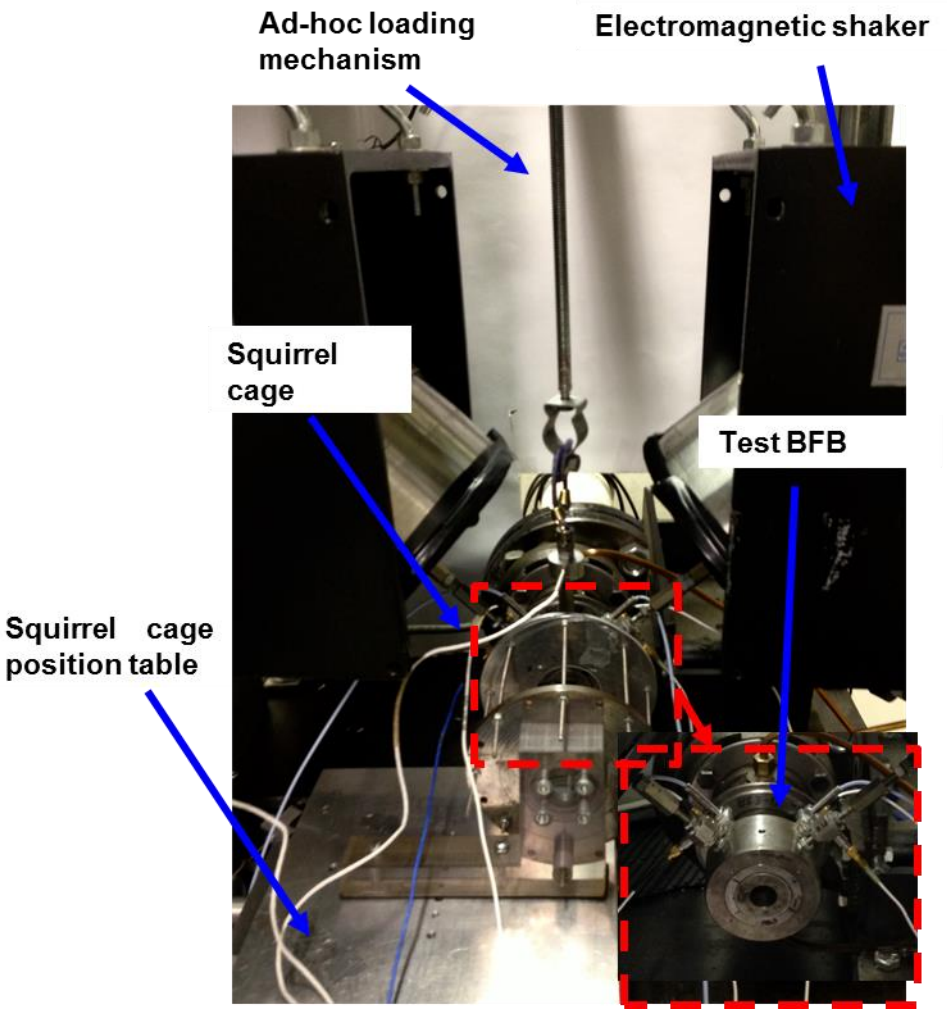

Figure 16. Experimental setup for dynamic load tests.

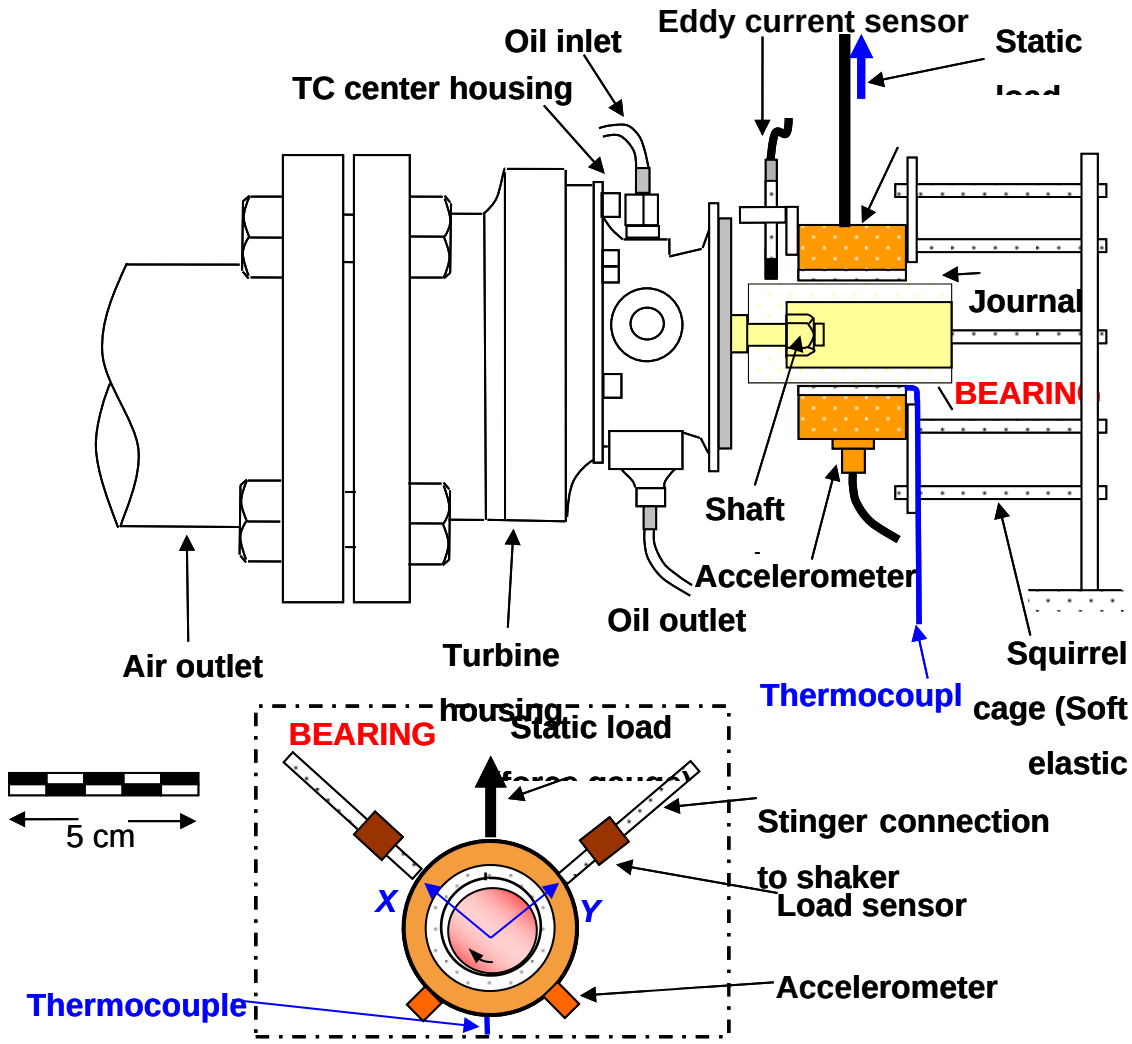

Figure 17. Schematic view representing the dynamic load test of a BFB while airborne [27].

In the various tests, three stainless steel shims, placed 120° apart from each other, are installed behind the bump foil strip and glued to the bearing inner diameter, as seen in Figure 4. One shim locates 45° from the fixed end top foil and acts as a reference for the position of the other shims. Each shim has an adhesive coating on one side that affixes it to the inner diameter of the bearing housing.

Parameter Identification Procedure

Figure 18 presents a schematic view of the test system used for parameter identification. The parameter identification methodology follows that advanced in Refs. [19,26], and is described below.

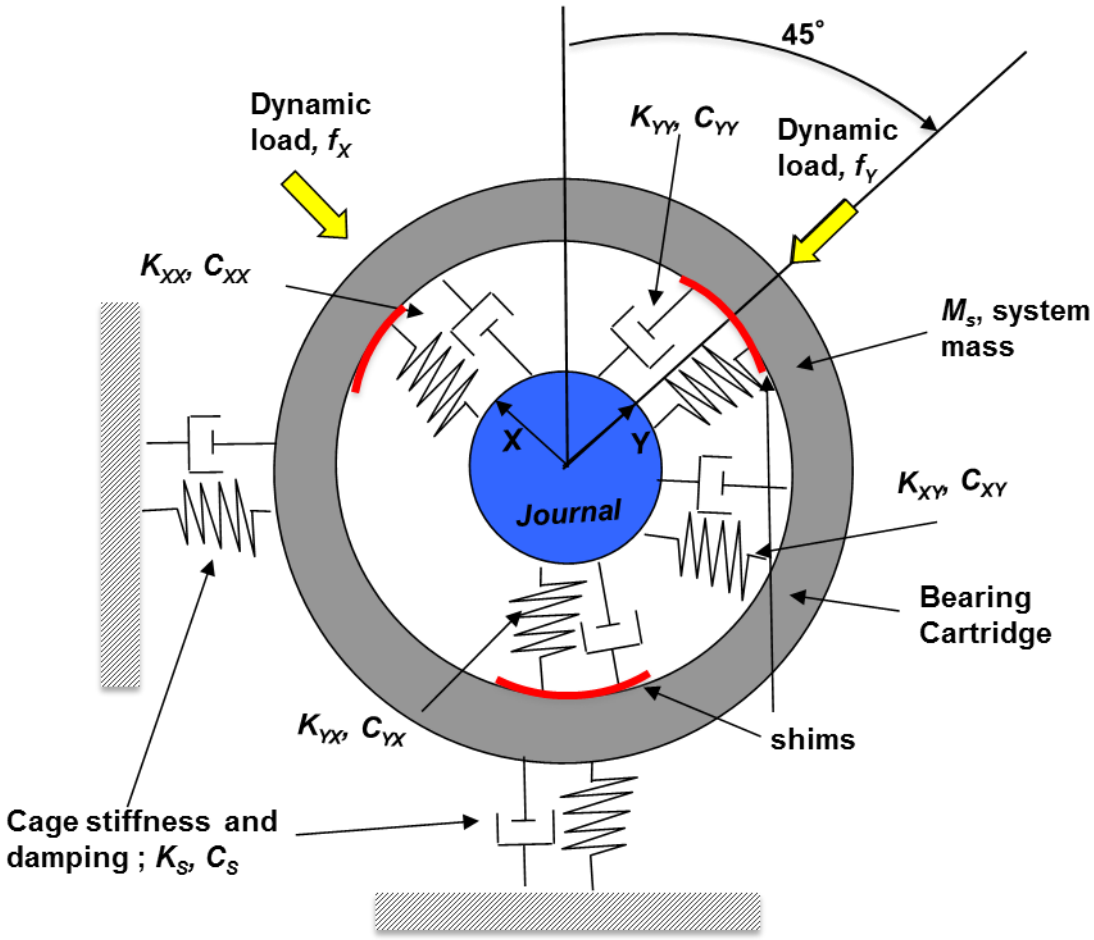

Figure 18. Schematic view representation of a BFB with idealized mechanical parameters [27].

Electromagnetic shakers apply dynamic loads with a sine sweep wave shape mathematically described as

$$F_{(t)} = \left[F_o + \Delta F t\right] \sin\left[\left(\omega_o + \Delta\omega t\right) t\right] \tag{3}$$

where F_o is a steady load amplitude, ω_o is the initial excitation frequency, and $\Delta\omega$ and ΔF designate the rates of increase in frequency and dynamic load, respectively. The

temporal changes in dynamic load (ΔF) and excitation frequency ($\Delta\omega$) are user defined, selected to maintain a constant bearing displacement amplitude relative to the shaft [19,27].

Electromagnetic shaker loads, F_X and F_Y, excite the test bearing producing its motion. The TC journal on the flexible shaft also displaces when a dynamic load is applied to the bearing. Define (x, y) and (x_j,y_j) as the absolute bearing and journal displacements, respectively. Hence, $(x', y') = (x, y) - (x_j, y_j)$ are the bearing displacements relative to the journal.

The effective system mass $(M_S)_{X,Y}$, cage stiffness $(K_S)_{X,Y}$ and cage damping coefficients $(C_{S_X})_{X,Y}$ are estimated from impact loads prior to the experiments. Consult Appendix D for details on the identification of the parameters.

The equation of motion for the bearing cartridge is

$$\begin{bmatrix} M_{S_X} & 0 \\ 0 & M_{S_Y} \end{bmatrix}\begin{Bmatrix} \ddot{x} \\ \ddot{y} \end{Bmatrix} + \begin{bmatrix} C_{S_X} & 0 \\ 0 & C_{S_Y} \end{bmatrix}\begin{Bmatrix} \dot{x} \\ \dot{y} \end{Bmatrix} + \begin{bmatrix} K_{S_X} & 0 \\ 0 & K_{S_Y} \end{bmatrix}\begin{Bmatrix} x \\ y \end{Bmatrix} + \begin{bmatrix} C_{XX} & C_{XY} \\ C_{YX} & C_{YY} \end{bmatrix}\begin{Bmatrix} \dot{x}' \\ \dot{y}' \end{Bmatrix} + \begin{bmatrix} K_{XX} & K_{XY} \\ K_{YX} & K_{YY} \end{bmatrix}\begin{Bmatrix} x' \\ y' \end{Bmatrix} = \begin{Bmatrix} F_X \\ F_Y \end{Bmatrix} \tag{4}$$

where $(K_{\alpha\beta,}\, C_{\alpha\beta})_{\alpha\beta=X,Y}$ are frequency dependent stiffness and damping coefficients.

The time domain excitation forces and resulting BFB motions are transformed into the frequency domain by applying the Discrete Fourier Transform (DFT), i.e.,

$$\bar{F}_{X(\omega)} = DFT\left(F_{X(t)}\right)\ ;\ \bar{x}'_{(\omega)} = DFT\left(x'_{(t)}\right)\ ;\ \bar{A}_{X(\omega)} = DFT\left(\ddot{x}_{(t)}\right) \tag{5}$$

and likewise for displacements and other variables along the Y direction. Recall that the DFT[$x'_{(t)}$]=$j\omega\ \bar{x}'_{(\omega)}$, where $j = \sqrt{-1}$.

Also

$$DFT\left[\dot{x}_{(t)}\right] = \frac{\bar{A}_{X(\omega)}}{j\omega},\ DFT\left[x_{(t)}\right] = -\frac{\bar{A}_{X(\omega)}}{\omega^2} \tag{6}$$

A frequency domain analysis of the equations of motion for the test bearing yields the direct and cross-coupled stiffness and damping coefficients. The frequency domain equation of motion is

$$\begin{bmatrix} K_{XX}+j\omega C_{XX} & K_{XY}+j\omega C_{XY} \\ K_{YX}+j\omega C_{YX} & K_{YY}+j\omega C_{YY} \end{bmatrix}\begin{bmatrix} \bar{x}'_{(\omega)} \\ \bar{y}'_{(\omega)} \end{bmatrix}=\begin{bmatrix} \bar{G}_{X(\omega)} \\ \bar{G}_{Y(\omega)} \end{bmatrix}$$
$$=\begin{bmatrix} \bar{F}_{X(\omega)} \\ \bar{F}_{Y(\omega)} \end{bmatrix}-\begin{bmatrix} M_{S_X}+C_{S_X}/j\omega-K_{S_X}/\omega^2 \\ M_{S_Y}+C_{S_Y}/j\omega-K_{S_Y}/\omega^2 \end{bmatrix}\begin{bmatrix} \bar{A}_{X(\omega)} \\ \bar{A}_{Y(\omega)} \end{bmatrix} \quad (7)$$

where $\left(\bar{x}'_{(\omega),}\,\bar{y}'_{(\omega)}\right)$ are the DFTs of the bearing displacements (x', y') relative to the journal, $\left(\bar{F}_{X(\omega)}, \bar{F}_{Y(\omega)}\right)$ are the DFTs of the excitation forces, and $\left(\bar{A}_{X(\omega)}, \bar{A}_{Y(\omega)}\right)$ are the DFTs of the bearing absolute accelerations.

The compact form of the equation of motion in the frequency domain equation is

$$\begin{bmatrix} H_{XX} & H_{XY} \\ H_{YX} & H_{YY} \end{bmatrix}\begin{bmatrix} \bar{x}'_{(\omega)} \\ \bar{y}'_{(\omega)} \end{bmatrix}=\begin{bmatrix} \bar{G}_{X(\omega)} \\ \bar{G}_{Y(\omega)} \end{bmatrix} \quad (8)$$

where $\mathbf{H}_{(\omega_k)}=(\mathbf{K}+j\omega_k\mathbf{C})$ is the matrix of bearing impedance coefficients at the discrete excitation frequencies (ω_k).

Two independent (load) excitations are required to determine the eight frequency dependent force coefficients. In practice, the bearing is excited by loads of the form $\mathbf{F}^X=[F_X\ 0]^T$, and $\mathbf{F}^Y=[0\ F_Y]^T$, respectively. The equations for the two sets of dynamic load excitations become

$$\begin{bmatrix} H_{XX} & H_{XY} \\ H_{YX} & H_{YY} \end{bmatrix}\begin{bmatrix} \bar{x}'^{X}_{(\omega)} & \bar{x}'^{Y}_{(\omega)} \\ \bar{y}'^{X}_{(\omega)} & \bar{y}'^{Y}_{(\omega)} \end{bmatrix}=\begin{bmatrix} \bar{G}^X_{X(\omega)} & \bar{G}^Y_{X(\omega)} \\ \bar{G}^X_{Y(\omega)} & \bar{G}^Y_{Y(\omega)} \end{bmatrix} \quad (9)$$
$$\mathbf{H}\bar{\mathbf{z}}=\bar{\mathbf{G}}$$

The first column in the $\bar{\mathbf{z}}$ matrix contains the relative bearing displacements along the *X* and *Y* axis as a electromagnetic shaker apply dynamic loads along the *X* axis

(superscripts), while the second column is the bearing displacements as the electromagnetic shakers excite the *Y* axis.

At each frequency (ω_k), the bearing impedance coefficients are calculated as $\mathbf{H}_{(\omega_k)} = \overline{\mathbf{G}}_{(\omega_k)} \overline{\mathbf{z}}^{-1}_{(\omega_k)}$, and the bearing force coefficients are extracted from

$$\{K_{\alpha\beta}\}_{(\omega_k)} = \mathrm{Re}(\{H_{\alpha\beta}\}_{\omega_k}), \quad \{C_{(\omega_k)}\}_{\alpha\beta} = \frac{\mathrm{Im}(\{H_{\alpha\beta}\}_{\omega_k})}{j\omega_k} \qquad \alpha\beta = X, Y \tag{10}$$

The bearing loss factor (γ) follows from a development in Refs. [19,27]. The proportional structural damping model is

$$\mathbf{C}\omega = \gamma\mathbf{K} \tag{11}$$

The estimation of a unique loss factor (γ) follows from equating the energy dissipated by viscous damping (E_v) to the energy dissipated by material damping (E_m) over the entire duration of the experiment (t=0-t_{end}) i.e.,

$$E_V = \int_{t=0}^{t_{end}} \dot{\mathbf{z}}^T \mathbf{C}\, \dot{\mathbf{z}}\, dt = E_M = \frac{\gamma}{\omega} \int_{t=0}^{t_{end}} \dot{\mathbf{z}}^T \mathbf{K}\, \dot{\mathbf{z}}\, dt \tag{12}$$

Thus

$$\gamma = \frac{\int_{t=0}^{t_{end}} \dot{\mathbf{z}}^T \omega\mathbf{C}\, \dot{\mathbf{z}}\, dt}{\int_{t=0}^{t_{end}} \dot{\mathbf{z}}^T \mathbf{K}\, \dot{\mathbf{z}}\, dt} \tag{13}$$

Data Analysis

An in-house DAQ program generates ten load excitation waveforms each lasting 0.2 s, and records 4,096 data samples of force, bearing displacement, and acceleration. The sampling rate is 20,480/sec for each waveform, thus 40,960 data samples (for ten waveforms) are collected.

Computational software processes the BFB response motions, applies the DFT transforming the time domain data into the frequency domain, and extracts the force coefficients according to the above procedure.

Note that a coordinate transformation[9] is used to determine the force coefficients with respect to a coordinate system ($\underline{X}$, $\underline{Y}$) where $\underline{X}$ is parallel to the vertical plane (the static load direction) and $\underline{Y}$ is horizontal. The transformation allows the knowledge of the bearing force coefficients to be understood with respect to the direction of static load ($\underline{X}$).

Figure 19 presents the sine sweep load excitation waveforms (200-400Hz), applied along the *X* and *Y* directions. Note that more mechanical energy is required to produce the same displacement amplitudes at higher frequencies, thus the dynamic load is controlled (amplitude typically increases with excitation frequency) to maintain a constant bearing displacement amplitude (relative to the journal) across the excitation frequency range.

---

[9] For example, the stiffness matrix **K** for the *X*,*Y* coordinate system takes the form $\mathbf{K}=\mathbf{P}\underline{\mathbf{K}}\mathbf{P}^{T}$, where the coordinate transformation matrix $\boldsymbol{P}=\begin{bmatrix}\cos(\varphi) & \sin(\varphi)\\ -\sin(\varphi) & \cos(\varphi)\end{bmatrix}$, where φ is the angle from the $\underline{Y}$ axis to the *Y* axis. A similar method is employed in Ref. [6].

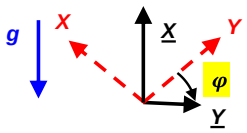

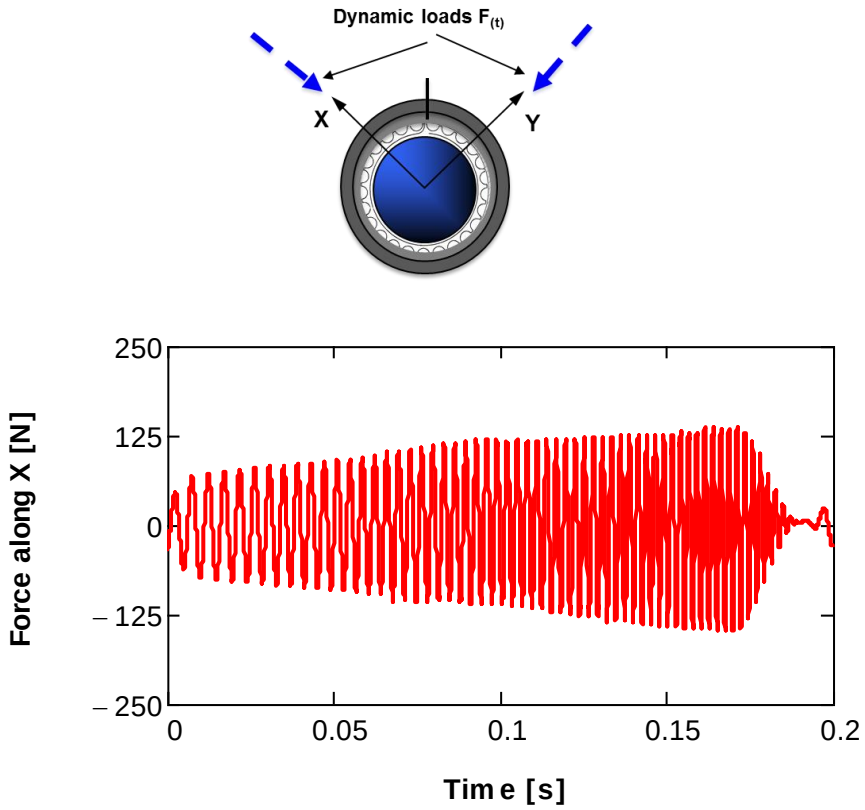

Figure 19. Typical dynamic excitation forces exerted along the *X* direction. Sine sweep loads 200-400Hz. Specific load ~ 14.3 kPa. Stationary journal.

Figure 20 presents the average (of 10 excitation waveforms) DFT amplitudes of the dynamic loads (*X* and *Y* directions) versus excitation frequency. Note that the DFT amplitudes of the force are smaller than the time domain amplitudes. The DFT amplitude is smaller than the original signal when a full period (or multiple of periods) is not sampled [29]. Given the nature of the sine sweep wave form, the excitation frequency changes before a full period (at a given frequency) is sampled. Note that Ref. [27] reports similar results.

Note, in Figure 20, that the amplitudes of the forces along the *X* and *Y* directions are not equal. To maintain a given displacement amplitude, a larger force is typically applied along the *X* axis than along the *Y* axis. This is due to the different bearing stiffness $K_{YY} \neq K_{XX}$.

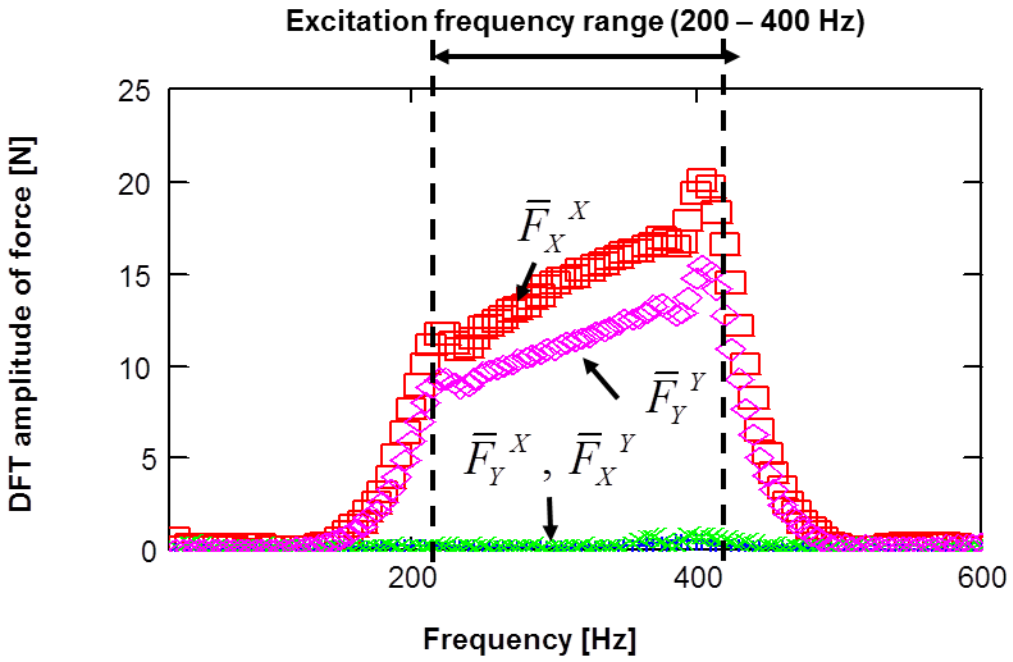

Figure 20. DFT amplitude of applied forces versus frequency. Sine sweep 200-400Hz. Average of 10 excitations. Stationary journal.

Figure 21 shows the bearing displacements relative to the shaft, *X* and *Y* directions, due to the applied dynamic loads. The ($\bar{x}'^X$, $\bar{y}'^Y$) bearing displacements are maintained at ~20 μm, while the cross directional displacements ($\bar{x}'^Y$, $\bar{y}'^X$) are ~7 μm, due to the motion of the flexible rotor supporting the bearing. For completeness Appendix E presents the bearing motion measurements with journal rotation at 50 krpm.

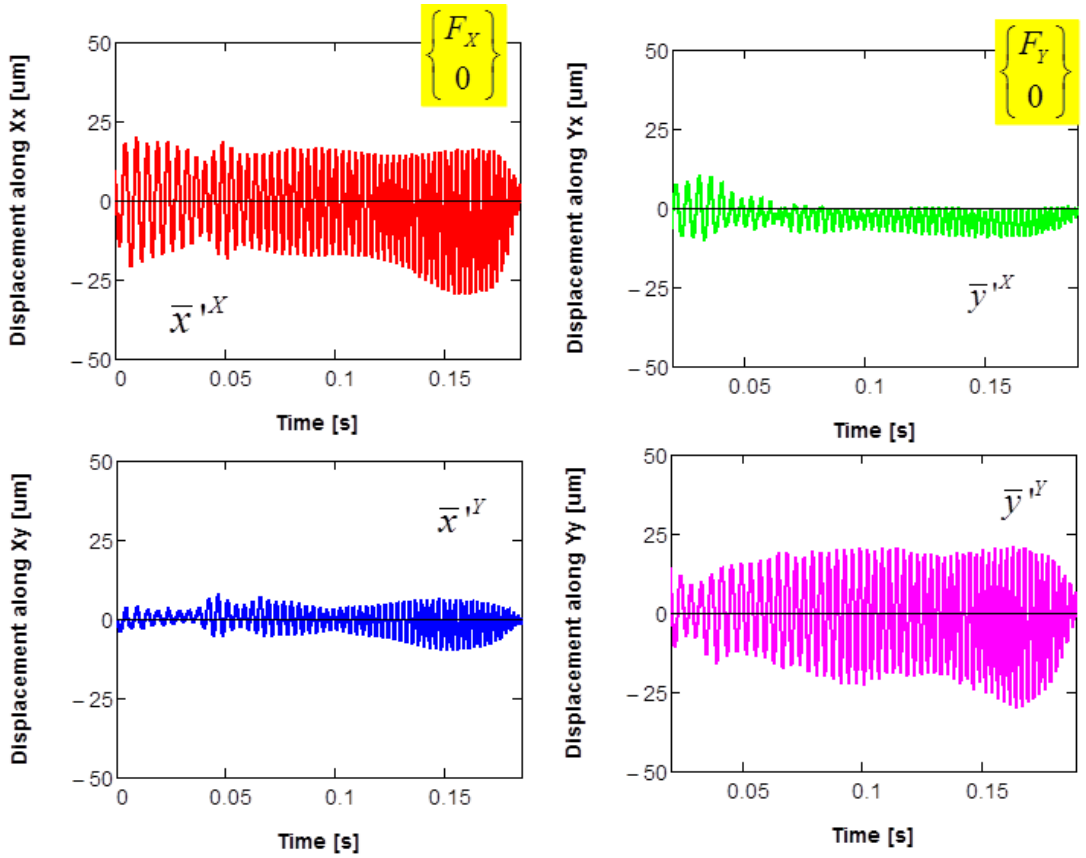

Figure 21. Direct (top) and cross directional (bottom) bearing relative displacements along *X* and *Y* directions. Applied specific load *W/LD*~ 27 kPa. Stationary journal

Figure 22 shows the DFT amplitudes of the bearing displacements (relative to the journal). The direct displacements ($\bar{x}'^{X}, \bar{y}'^{Y}$) are approximately constant over the excitation frequency range (200-400 Hz). Note that the time domain direct displacements amplitudes ($\bar{x}'^{X}, \bar{y}'^{Y}$) are ~20 μm, while the frequency domain displacement amplitudes are ~3 μm.

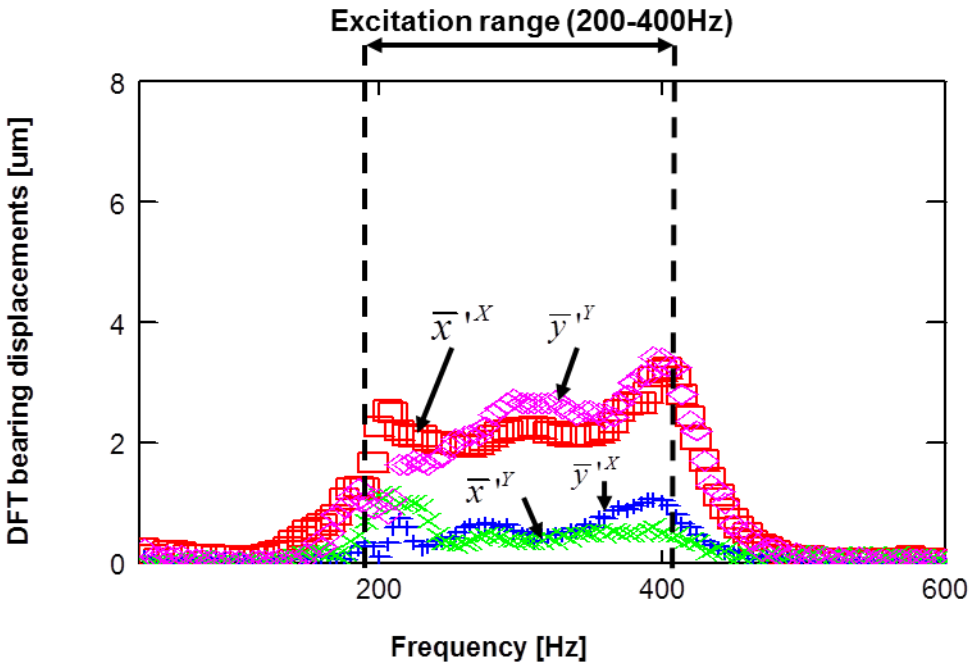

Figure 22. Average DFT amplitude of bearing displacements versus frequency. Sine sweep 200-400Hz. Average of 10 excitations. Stationary journal. Specific load ~ 27 kPa

Figure 23 shows the DFT amplitude of the bearing accelerations, *X* and *Y* directions. The bearing accelerations $(\bar{A}_X^X, \bar{A}_Y^Y))$ increase with excitation frequency in similar fashion to the dynamic excitation forces. Note that the cross accelerations $(\bar{A}_X^Y, \bar{A}_Y^X)$ are small.

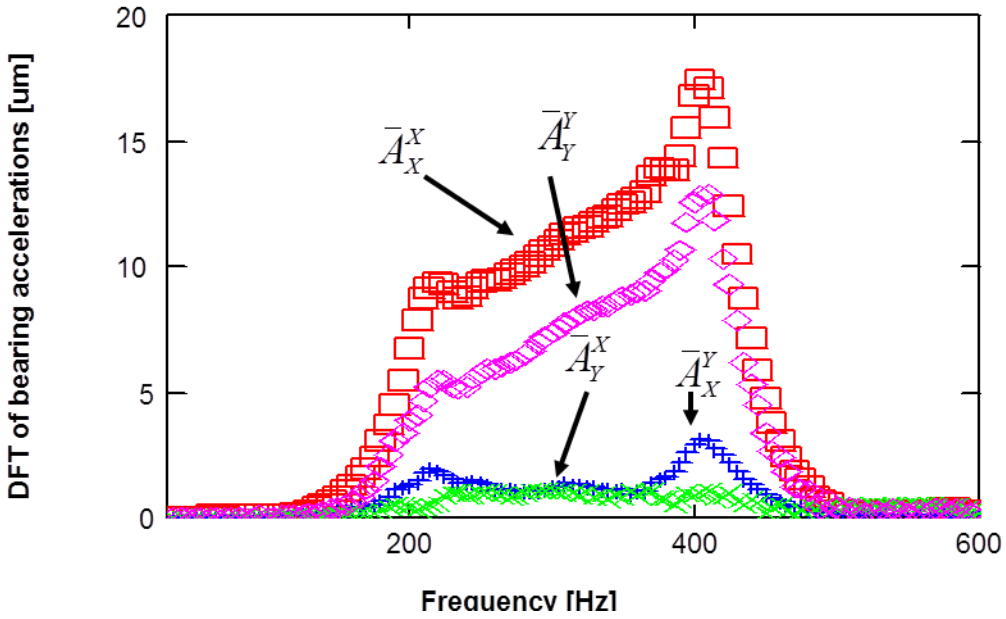

Figure 23. Average DFT amplitude of bearing absolute accelerations versus frequency. Sine sweep 200-400Hz. Average of 10 excitations. Stationary journal. Specific load of 27 kPa.

Rotordynamic Force Coefficients of a BFB without shims

During full gas film operation (with journal speed), the force coefficients of the gas film act in series with the bump foil structure. This section discusses the force coefficients of a BFB, without shims and with shims, with a stationary journal and then operating with a journal speed of ~50 krpm[10].

All of the experimental results reported in this section correspond to a dynamic displacement amplitude of 20 μm and with a static specific load *W/LD*~ 14.3 kPa. Figure 24 through 25 present the force coefficients for a bearing without shims.

Figure 24 shows the stiffness coefficients (direct and cross coupled) for the original bearing, without journal rotation and with journal rotation (~50 krpm, 833 Hz). The cross coupled stiffness coefficients ($\underline{K}_{XY}$, K_{YX}) are small for both conditions, with and without journal rotation. The direct stiffnesses ($\underline{K}_{XX}$, $\underline{K}_{YY}$) increase with excitation frequency and are largely the same for operation without or with journal rotation. The

[10] A large temperature rise (~ 30°C in one test lasting 30 s) is recorded during the tests. However, the bearing temperature is not meticulously recorded.

presence of a gas film has little effect on the BFB stiffnesses; thus indicating that the stiffness of the bump foil structure dominates the bearing stiffness. The stiffness along the static load direction ($\underline{X}$) is only slightly higher than the stiffness of the direction without static load ($\underline{Y}$) i.e., $\underline{K}_{XX} \geq \underline{K}_{YY}$.

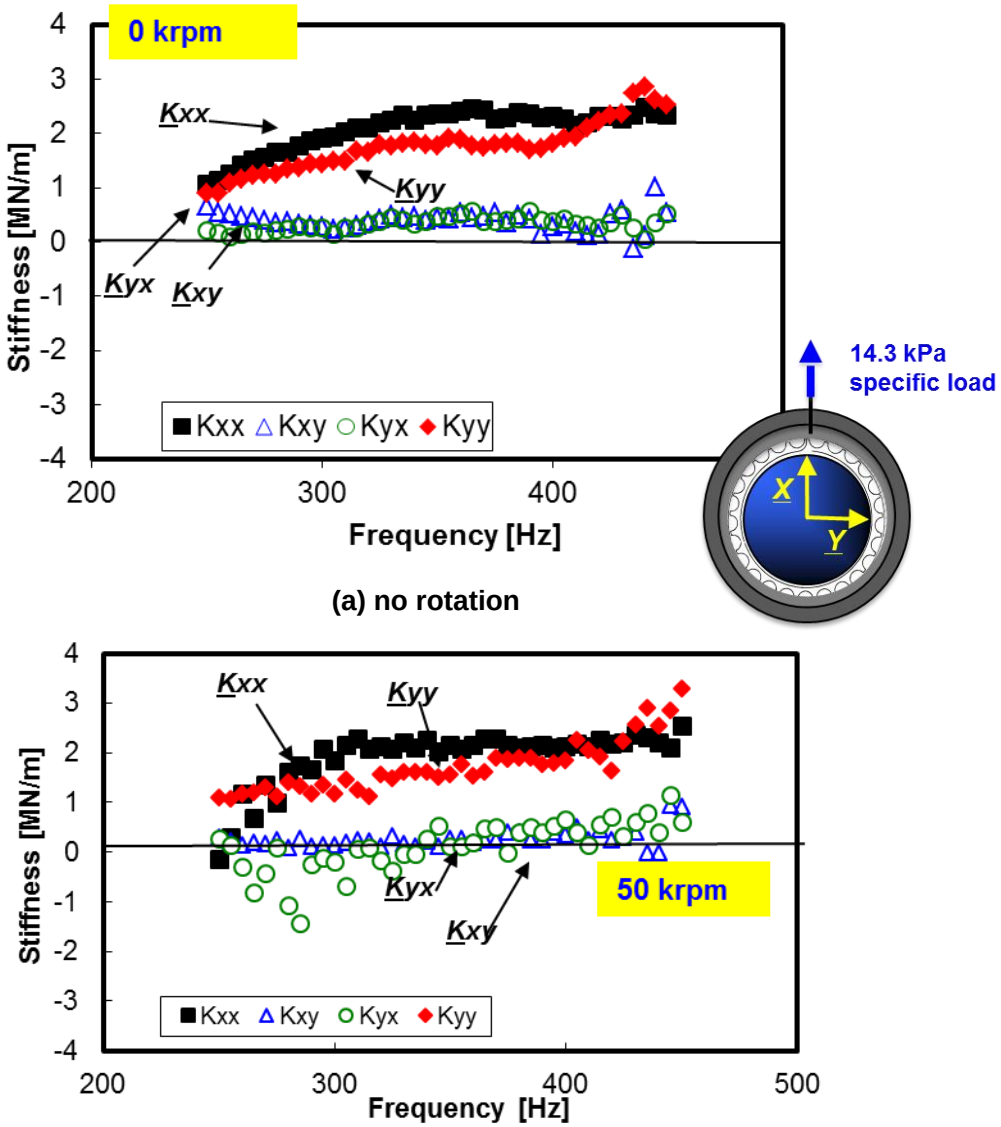

Figure 24. BFB stiffnesses ($\underline{K}_{\alpha\beta}$)$_{\alpha\beta=\underline{X},\underline{Y}}$ versus excitation frequency for original bearing (without shims). (a) no journal rotation and (b) with journal rotation (50 krpm). Results for sine sweep loads from 200-450Hz, displacement amplitude~ 20 μm, and a specific load *W/LD*~14.3kPa.

Figure 25 shows the viscous damping coefficients for the original bearing (a) stationary and (b) operating at 50 krpm. Interestingly, rotor speed has little effect on $\underline{C}_{XX}$, while $\underline{C}_{YY}$ drops when the rotor spins (50 krpm). Note that the cross coupled damping coefficients ($\underline{C}_{XY}$, $\underline{C}_{YX}$) are lower than the direct ones, and decrease for conditions with journal rotation. The steep drop in $\underline{C}_{XX}$ with frequency below 300 Hz and recall that the viscous damping coefficient may be inversely proportional to frequency [15], i.e., diminishing with frequency. Damping in the direction of the static load ($\underline{C}_{XX}$) decreases with increasing excitation frequency, while $\underline{C}_{YY}$ increases with frequency.

Table 2 presents the bearing loss factor (γ) for the original bearing stationary and operating at 50 krpm. The bearing loss factor (γ) remains largely unaffected by rotor speed and shim thickness (γ~0.39- 0.43).

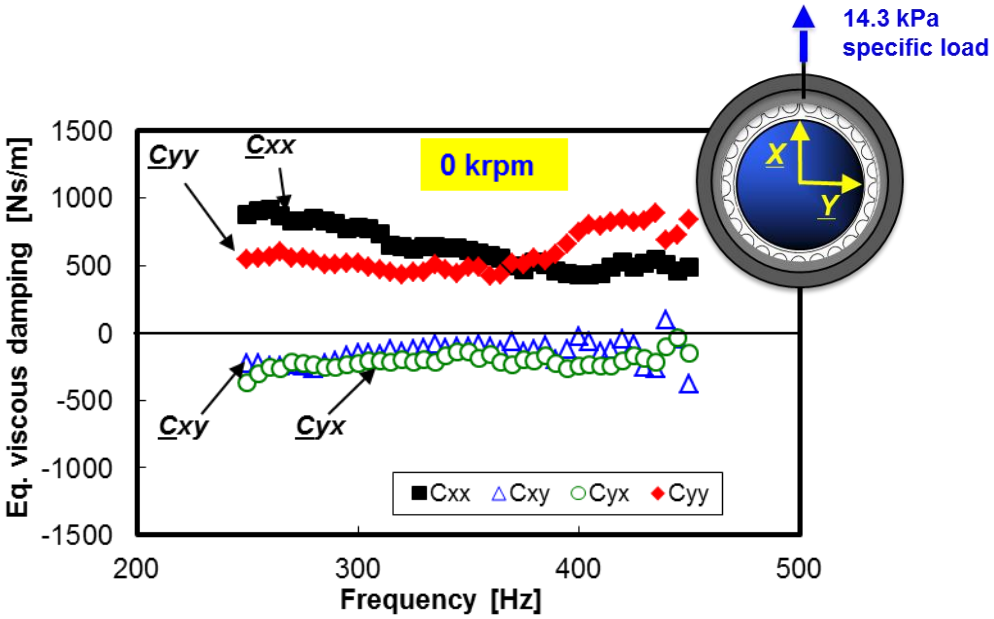

(a) no rotation

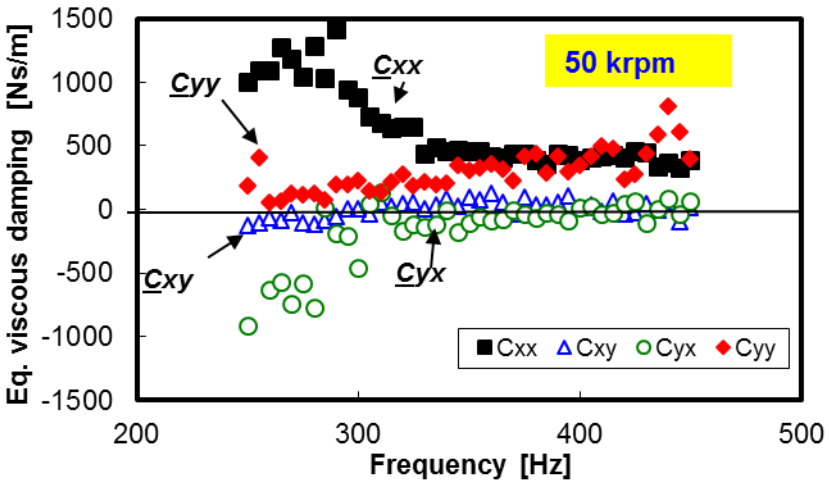

(b) 50 krpm (833 Hz)

Figure 25. BFB damping coefficients ($(\underline{C}_{\alpha\beta})_{\alpha\beta=\underline{X},\underline{Y}}$) versus excitation frequency for the original bearing (without shims). (a) no journal rotation and (b) with journal rotation (50 krpm). Results for sine sweep loads from 200-450 Hz, displacement amplitude~ 20 μm, and a specific load *W/LD*~14.3kPa.

Table 2 Loss factor for the original bearing (without shims) operating with a stationary journal and rotor speed (50 krpm).

Bearing Configuration		Loss Factor, γ
0 krpm	Original	0.39
50 krpm	Original	0.43

Note that the dynamic displacement amplitude (20 μm) is small compared to the bearing radial clearance (120 μm). The force coefficients shown serve as a benchmark to determine the effect of shimming on the BFB force coefficients. The uncertainty in the bearing stiffness and damping coefficients is 0.08 MN/m and 80 Ns/m, respectively. Consult Appendix C for details on the uncertainty analysis.

Rotordynamic Force Coefficients for a Shimmed BFB

Figure 26 through 36 show the bearing force coefficients (stiffness and damping) for the BFB configured with shim thicknesses equal to 30 μm and 50 μm, and for operation with a stationary journal and with journal rotation at 50 krpm (833 Hz).

Figure 26 shows the stiffness coefficients for the bearing with 30 μm shims. The magnitudes of $\underline{K}_{XX}$ are comparable for operation with or without journal rotation, while $\underline{K}_{YY}$ is larger when the journal is stationary than when the journal is spinning. This indicates that rotational speed has a minimal effect on $\underline{K}_{XX}$. However journal rotation reduces $\underline{K}_{YY}$. Note also that the stiffness coefficients of the BFB with 30 μm shims are roughly the same magnitude as the force coefficients of the original bearing and show the same trend with respect to excitation frequency. Interestingly, $\underline{K}_{YY}$ for the bearing with 30 μm (stationary journal) is larger (15%) than that of the original bearing. The cross-coupled stiffnesses ($\underline{K}_{XY}$, $\underline{K}_{YX}$) are smaller than the direct stiffnesses and increase with shim thickness.

When there is no journal rotation and below 325 Hz, $\underline{C}_{YY} \approx \underline{C}_{XX}$.. Above 325 Hz, $\underline{C}_{YY} \geq \underline{C}_{XX}$. However, when there is journal rotation (50 krpm) and below 370 Hz, $\underline{C}_{YY} \leq \underline{C}_{XX}$. And above 370 Hz, $\underline{C}_{YY} \approx \underline{C}_{XX}$. $\underline{C}_{YY}$ drops when there is journal rotation than without. Clearly rotor speed significantly lowers the damping along the horizontal axis ($\underline{Y}$). The direct damping coefficients of the bearing with 30 μm are slightly larger than those of

the original bearing (both stationary and operating at 50 krpm). Note that $\underline{C}_{YY}$ for the bearing with 30 μm shims (stationary journal) is 30% larger than that of the original bearing.

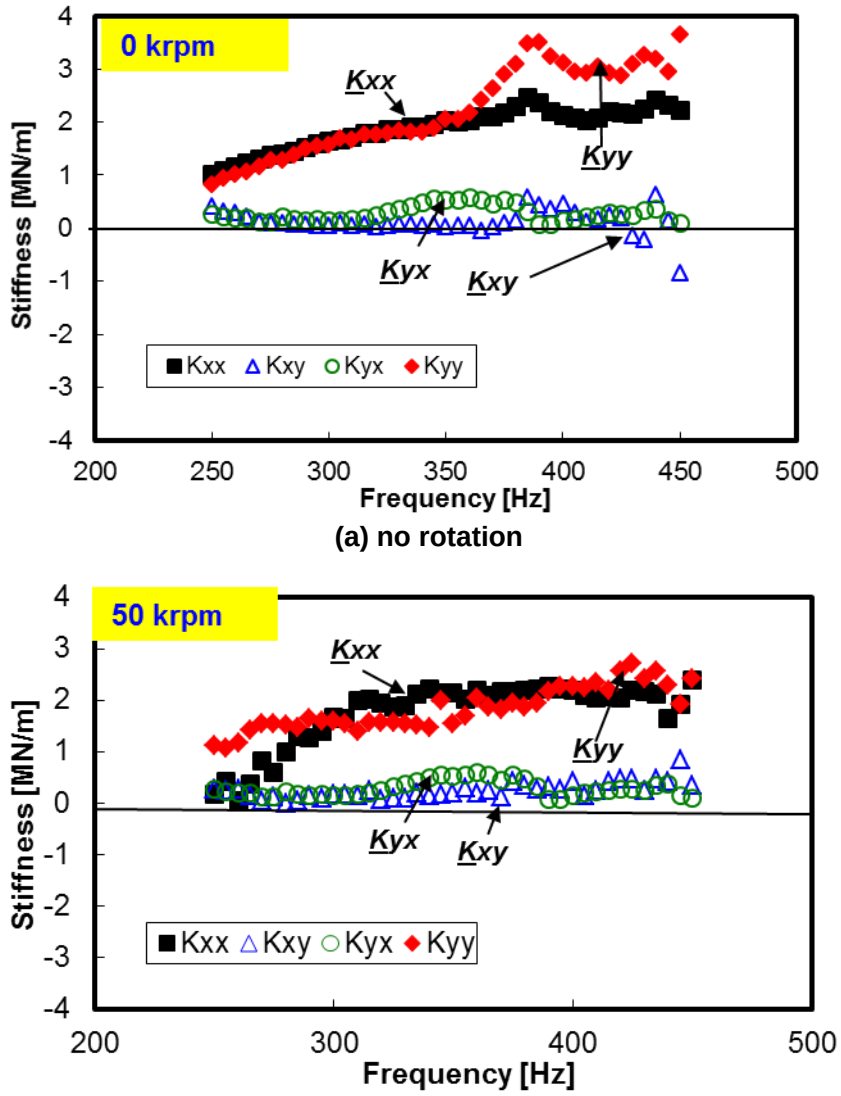

(a) no rotation

(b) 50 krpm (833 Hz)

Figure 26. BFB stiffnesses ($(\underline{K}_{\alpha\beta})_{\alpha\beta=\underline{X},\underline{Y}}$) versus excitation frequency for a bearing with 30 μm shims. (a) no journal rotation and (b) with journal rotation (50 krpm). Results for sine sweep loads from 200-450Hz, displacement amplitude~20 μm, and a specific load *W/LD*~14.3 kPa.

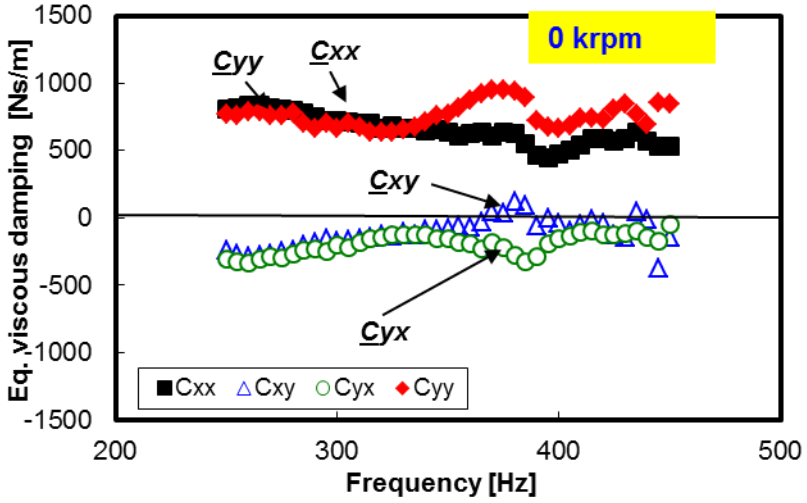

(a) no rotation

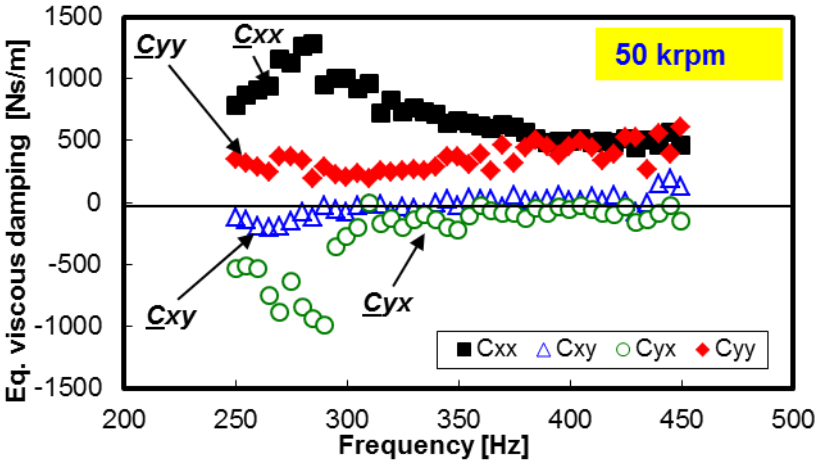

(b) 50 krpm (833 Hz)

Figure 27. BFB damping coefficients ($\underline{C}_{\alpha\beta})_{\alpha\beta=\underline{X},\underline{Y}}$ versus excitation frequency for a bearing with 30 µm shims. (a) no journal rotation and (b) with journal rotation (50 krpm). Results for sine sweep loads from 200-450 Hz, displacement amplitude~20 µm, and a specific load *W/LD*~14.3 kPa.

The stiffness coefficients of the bearing with 50 µm shims (Figure 28 through 29) have similar magnitudes as those of the bearing with 30 µm shims. Note that $\underline{K}_{YY} \approx \underline{K}_{XX}$ across the excitation frequency range (stationary journal and with journal rotation). The

direct stiffness coefficients are slightly lower for operation at 50 krpm as oppose to when the journal is stationary. When there is no journal rotation and below 370 Hz, $\underline{C}_{YY} \leq \underline{C}_{XX}$. And above 370 Hz, $\underline{C}_{YY} \approx \underline{C}_{XX}$. Note that $\underline{C}_{XX}$ of the bearing with 50μm shims is larger than that of the original bearing, while $\underline{C}_{YY}$ and the cross-coupled stiffness of the bearing with 50 μm shims are unremarkably different from those of the original bearing.

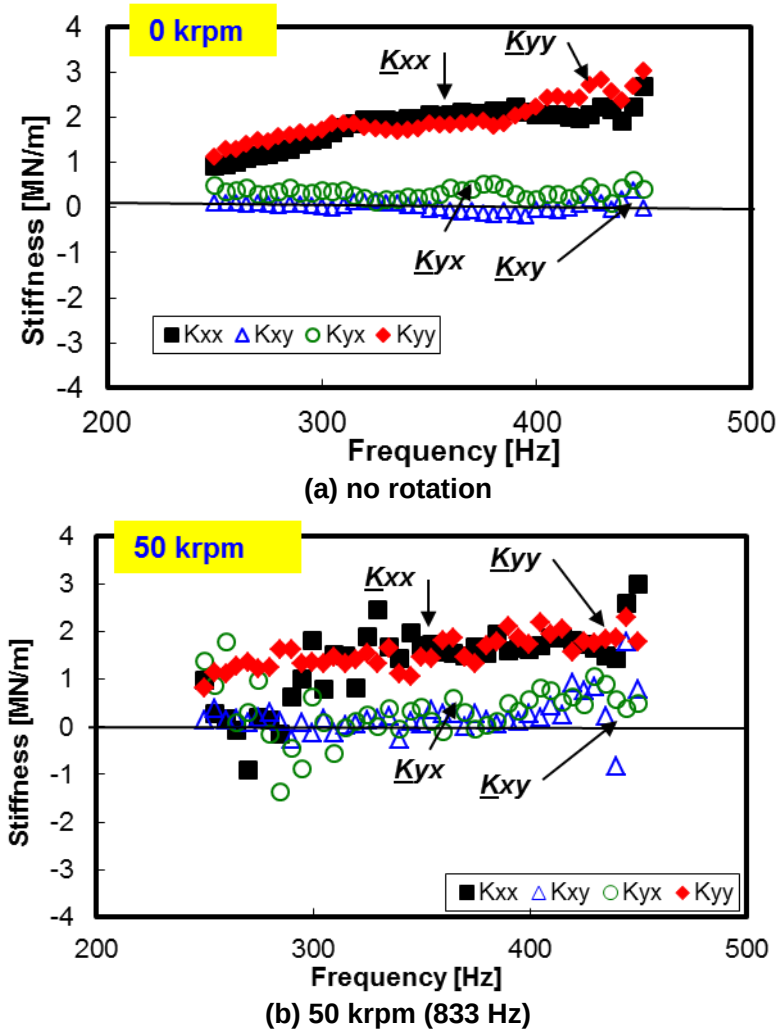

Figure 28. BFB stiffnesses ($(\underline{K}_{\alpha\beta})_{\alpha\beta=\underline{X},\underline{Y}}$) versus excitation frequency for a bearing with 50 μm shims. (a) no journal rotation and (b) with journal rotation (50 krpm). Results for sine sweep loads from 200-450Hz, displacement amplitude~ 20 μm, and a specific load *W/LD*~14.3kPa.

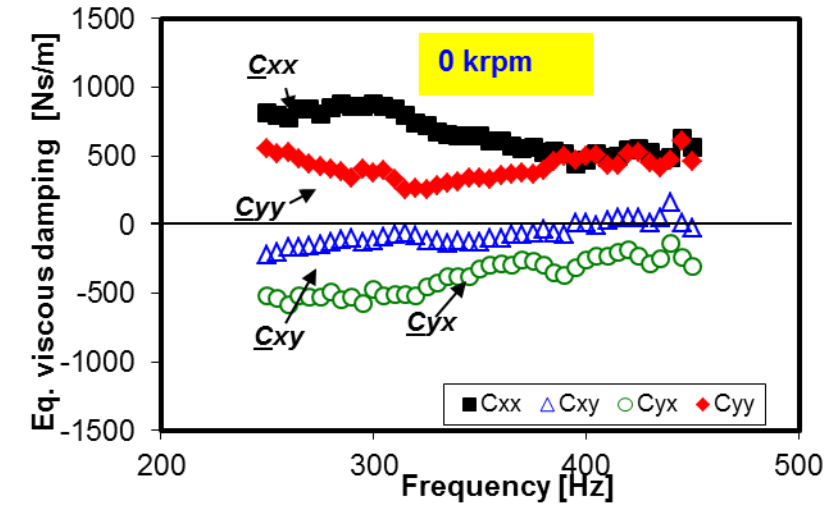

(a) no rotation

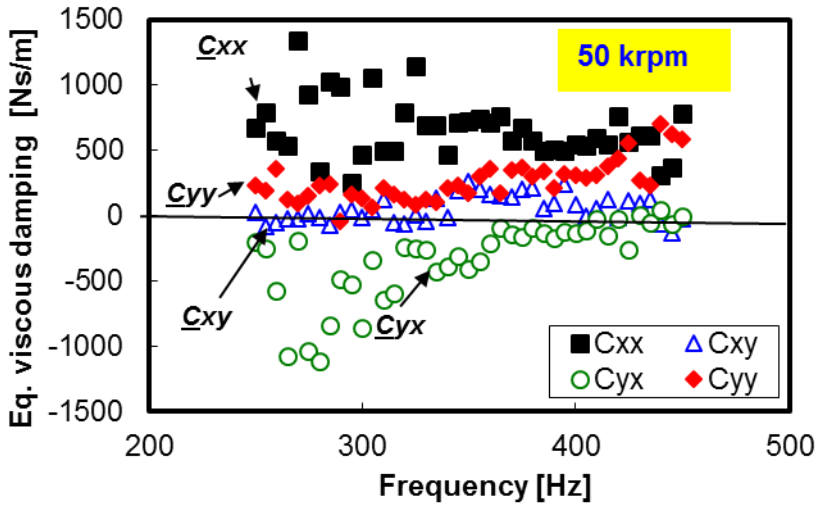

(b) 50 krpm (833 Hz)

Figure 29. BFB viscous damping coefficients ($(\underline{C}_{\alpha\beta})_{\alpha\beta=\underline{X},\underline{Y}}$) versus excitation frequency for a bearing with 50 μm shims. (a) no journal rotation and (b) with journal rotation (50 krpm). Results for sine sweep loads from 200-450Hz, displacement amplitude~ 20 μm, and a specific load *W/LD*~14.3kPa.

Table 3 presents the loss factor for the foil bearing with and without shims. Importantly enough, the bearing loss factor is largely unaffected by the shims (and rotor speed).

Table 3 Loss factor for the original bearing (without shims) and a bearing with shims of thickness 30 μm and 50 μm operating with a stationary journal and rotor speed (50 krpm).

Bearing Configuration		Loss Factor, γ
0 krpm	Original	0.39
	30 μm shims	0.48
	50 μm shims	0.39
50 krpm	Original	0.43
	30 μm shims	0.45
	50μm shims	0.43

Prior literature [3-5, 25] shows that the shimming increases the force coefficients (stiffness and damping) in both generation I and generation II BFBs. However, the results presented above suggest that shimming has only a minimal effect on the bearing stiffness coefficients and the bearing loss factor, while significantly increasing the bearing damping coefficients. It is likely that the bearing clearance is too large (or the displacement amplitude is too small) with respect to the shim thickness to appreciably increase bump deflection and the bearing stiffness.

Comparison of experimentally identified force coefficients with predictions

This section compares the experimentally estimated force coefficients to force coefficients predicted from a computational tool described in Ref. [30]. The bearing force coefficients are predicted at a shaft speed of 50 krpm over an excitation frequency range of 200 Hz - 450 Hz for the bearing dimensional parameters described in Table 2. A specific load (*W/LD*~27 kPa) is applied along the vertical axis ($\underline{X}$ axis) [11]. However, the code does not take into account the large dynamic loads (up to 143 kPa in the time domain and 14 kPa in the frequency domain) applied to the bearing. The bearing structural loss factor (γ) is assumed to be 0.8 for all predictions. The radial clearance is ~120 μm as estimated from static load tests on a BFB without shims [26]. The gas temperature is ~22°C and does not change, as the computational tool assumes an

[11] Predicted force coefficients under a specific load *W/LD* ~14.3 kPa are dramatically lower (~50%) than those estimated from experiment, thus the specific load is increased in order to recreate the test results.

isothermal condition. This is clearly a limitation to the analysis given that during TC operation, the temperature of the gas raises with time.

Table 4 Nominal dimensions and specifications for the test bearing.

Parameters	**Magnitude**
Shaft diameter, D_s	36.5 mm
Bearing axial length, L	38.10 mm
Top foil thickness (Inconel X750), t_T	0.1 mm
Foil length , $2\pi D_I$	110 mm
Elastic modulus, E	214 GPa
Poisson's ratio, v	0.29
Number of bumps, N_B	26
Bump foil (Inconel X750)	
Thickness, t_B	0.112 mm
Pitch, s_0	4.5 mm
Length, l_B	2.5 mm
Height, h	0.50 mm
Elastic modulus, E	214 GPa
Poisson's ratio, v	0.29
Shim (AISI 4140)	
Length	38.1 mm
Thickness, t_s	0.050, 0.030 mm
Width	7.87 mm
Angular extent	12°
Elastic modulus, E	214 GPa
Poisson's ratio, v	0.29
Nominal FB radial clearance[12], c_{nom}	0.12 mm
Free end bump foil stiffness, K_{ff}	21.4 GN/m^3
Fixed end bump foil stiffness, K_{fp}	39.4 GN/m^3
Applied specific load (*X axis*)	27 kPa
Lubricant supply temperature	22°C
Excitation frequency range	200-450 Hz

Figure 30 through 41 present the experimentally identified force coefficients and predicted force coefficients versus excitation frequency for a bearing without shims and

[12] The reported radial clearance of ~120 μm is estimated from the bearing geometry $c_{nom} = \frac{1}{2}(D_A - D_s)$.

with shim of thicknesses equal to 30 μm and 50 μm. The predicted $\underline{K}_{XX}$ is 30% higher than the experimentally identified $\underline{K}_{XX}$, while the predicted $\underline{K}_{YY}$ is 30% lower than that experimentally identified (uncertainty in the measured stiffness coefficients is ±0.08 MN/m). The predicted cross coupled stiffness coefficients ($\underline{K}_{XY}$, $\underline{K}_{YX}$) are larger in magnitude than those identified during the experiments. Although the predicted cross coupled stiffness coefficients ($\underline{K}_{XY}$, $\underline{K}_{YX}$) are large, they have the same sign indicating that they are structural.

Above 300 Hz, the predicted damping $\underline{C}_{XX}$ is comparable to the estimated $\underline{C}_{XX}$. Below 300 Hz the experimentally determined $\underline{C}_{XX}$ is significantly higher than predicted. Note that the experimental $\underline{C}_{YY}$ increases with excitation frequency while the predicted $\underline{C}_{YY}$ is lower and drops slightly with frequency. The predicted cross coupled damping coefficients agree quite well with the measured cross coupled damping coefficients over the excitation frequency range.

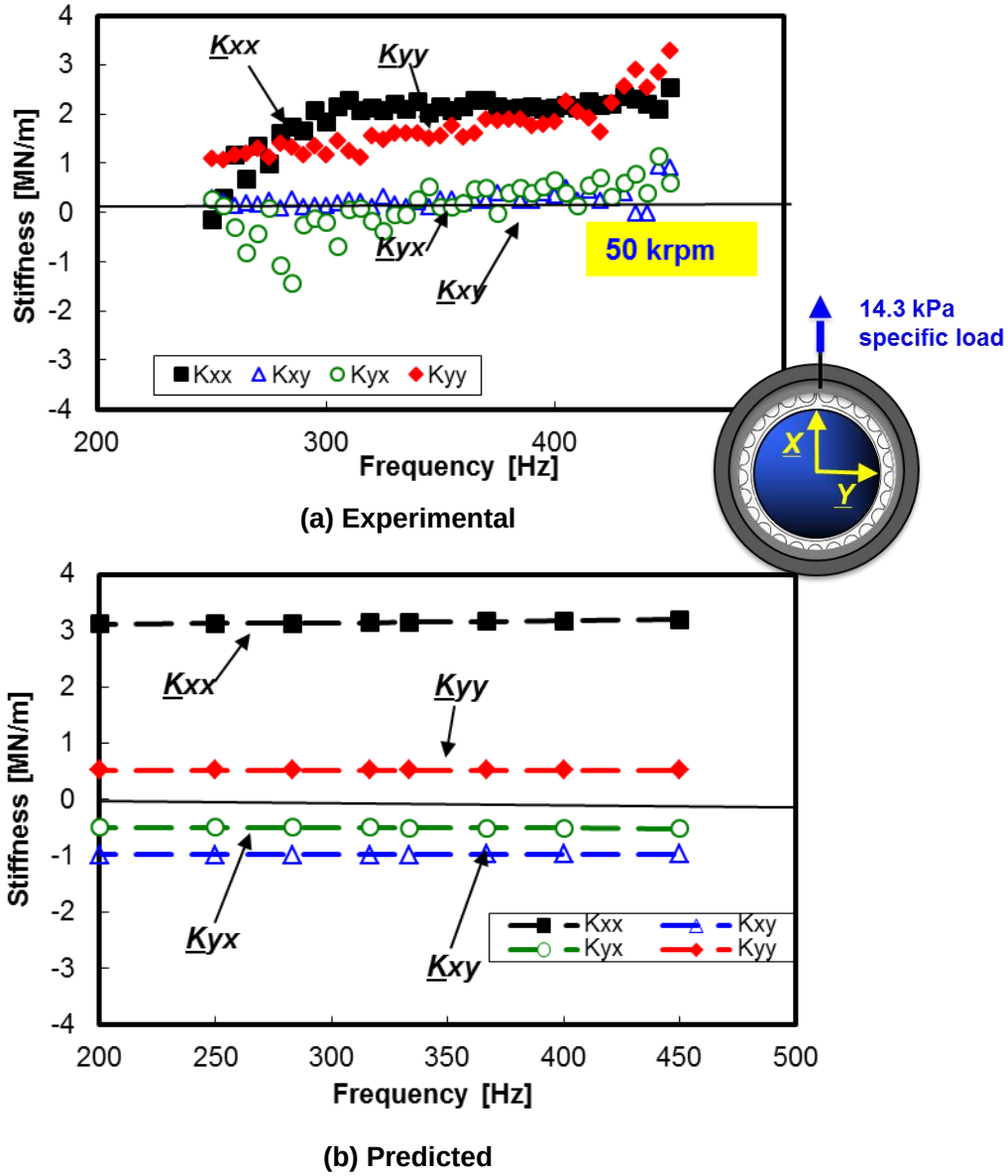

Figure 30. Stiffness coefficients versus frequency (a) measured and (b) predicted for the original bearing. Displacement amplitude~20 μm. Results for journal rotation (50 krpm) and sine sweep loads of 200-450Hz and a static load *W/LD* ~14.3 kPa. Predictions are carried out with a static load W/LD ~ 27.3 kPa.

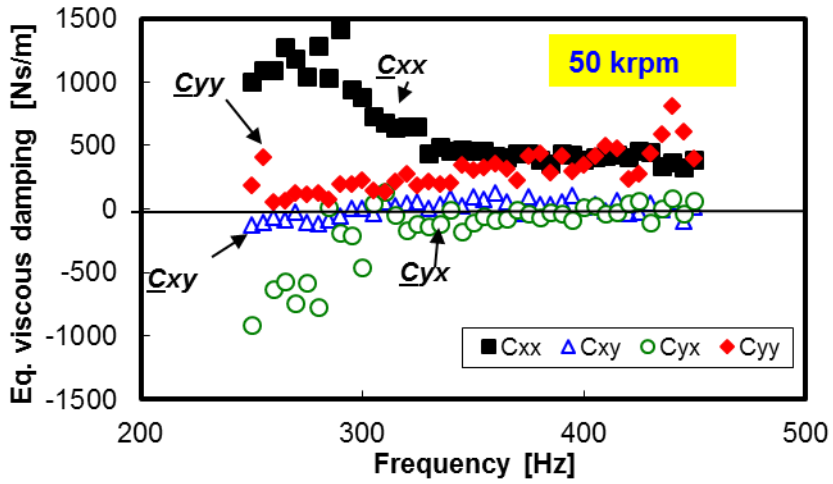

(a) Experimental

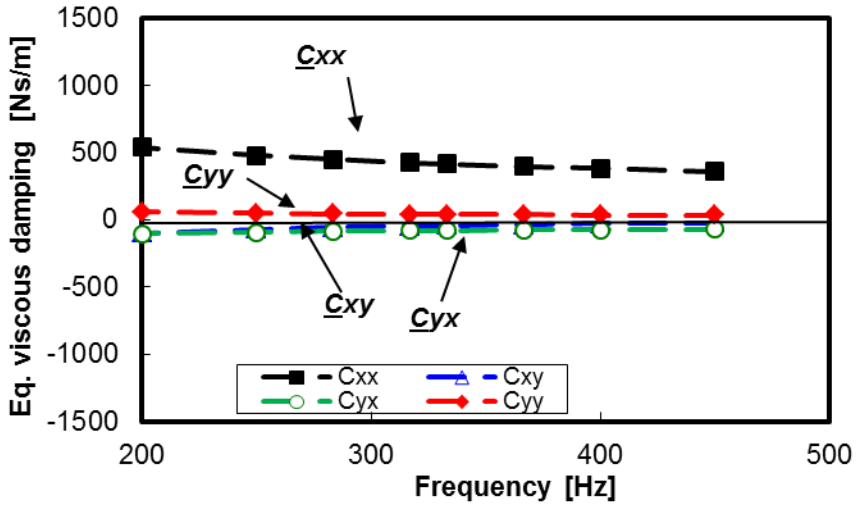

(b) Predicted

Figure 31. Damping coefficients versus frequency (a) measured and (b) predicted for the original bearing. Displacement amplitude~20 μm. Results for journal rotation (50 krpm) and sine sweep loads of 200-450Hz and a static load *W/LD* ~14.3 kPa. Predictions are carried out with a static load W/LD ~ 27.3 kPa.

The predicted $\underline{K}_{XX}$ for the bearing with 30 μm shims is still 30% larger than the experimentally identified $\underline{K}_{XX}$, however the predicted $\underline{K}_{YY}$ is within 20% of the experimental value. The experimental K_{XY} and K_{YX} are ~ 0 while the predicted K_{XY} and K_{YX} are large and negative. In general the predicted damping coefficients of the bearing

with 30 μm shims agree with the experimentally identified values. The predicted cross coupled damping coefficients, albeit small in magnitude, agree well with experimentally identified coefficients. The predicted $\underline{C}_{XX}$ agrees modestly with the experimental $\underline{C}_{XX}$, while $\underline{C}_{YY}$ is under predicted.

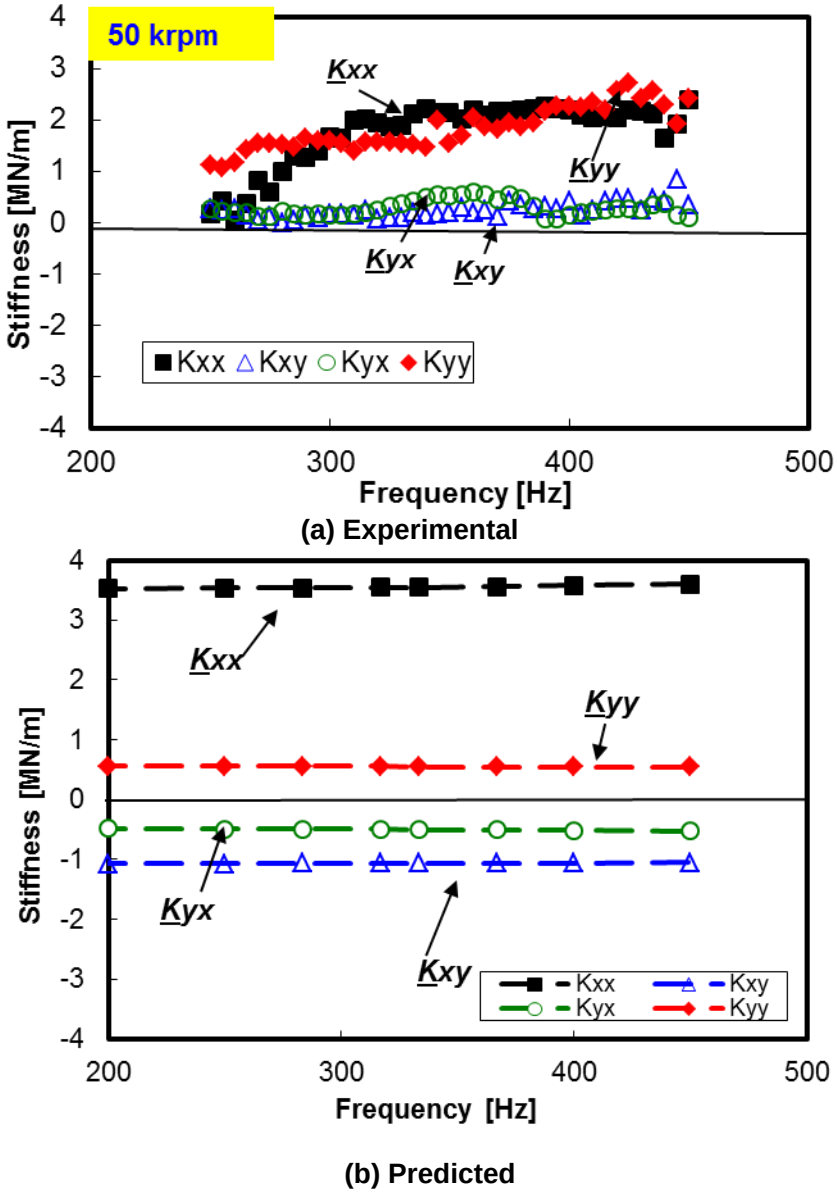

Figure 32. Stiffness coefficients versus frequency (a) measured and (b) predicted for a bearing with 30 μm shims. Experimental displacement amplitude~ 20μm. Results with journal rotation (50 krpm) and a static load W/LD ~14.3 kPa. Predictions are carried out with a static load W/LD ~ 27.3 kPa.

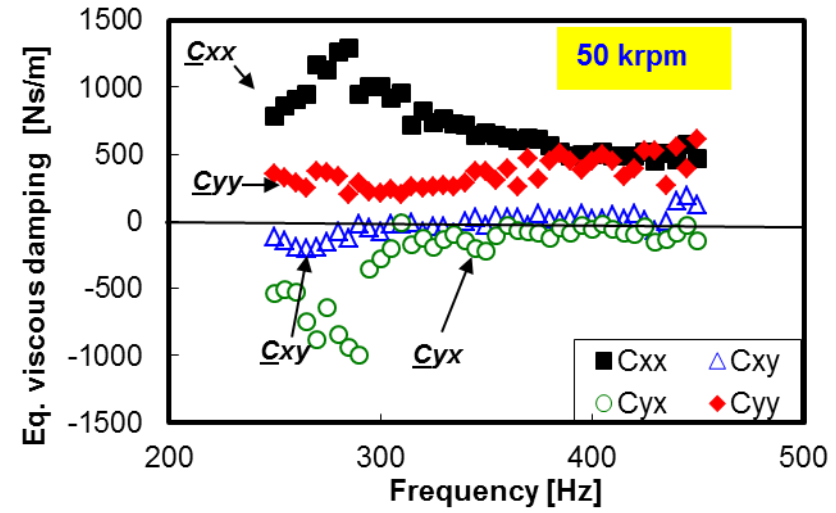

(a) Experimental

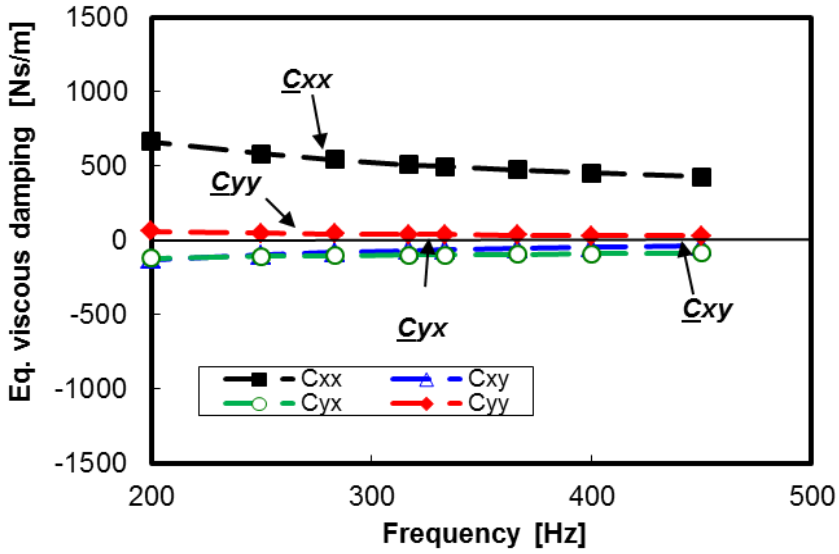

(b) Predicted

Figure 33. Damping coefficients versus frequency (a) measured and (b) predicted for bearing with 30 µm shims. Experimental displacement amplitude~ 20µm. Results for journal rotation (50 krpm) and a static load W/LD ~14.3 kPa. Predictions are carried out with a static load W/LD ~ 27.3 kPa.

Figure 34 and Figure 35 present the stiffness and damping coefficients for a bearing with 50 µm shims. The direct stiffness coefficients in the loaded direction (*X*) of the bearing with 50 µm shims is over predicted (by 40%) when compared to the experimentally identified

coefficients, however all other predicted coefficients are on the same order of magnitude as the experimental and in modest agreement. The direct and cross coupled damping coefficients for the bearing with 50 µm shims, agree reasonably well with the experimental damping coefficients across the excitation frequency range. However, the damping in the direction without a static load ($\underline{C}_{YY}$) remains constant with frequency while the predicted $\underline{C}_{YY}$ decreases with frequency.

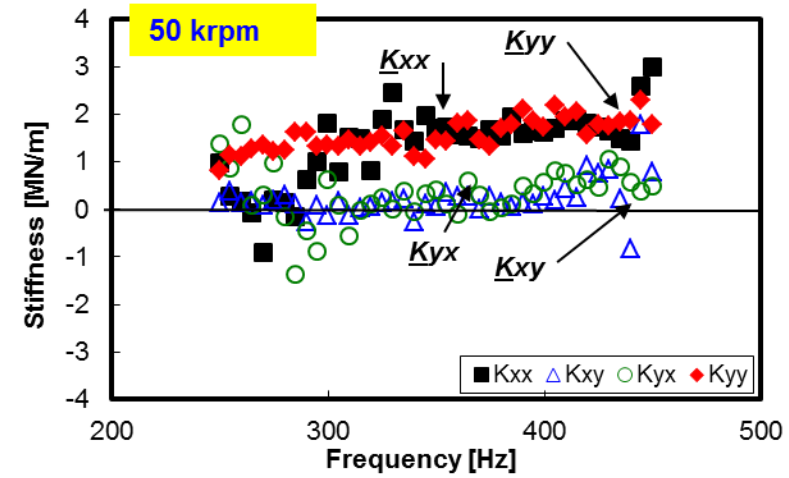

(a) Experimental

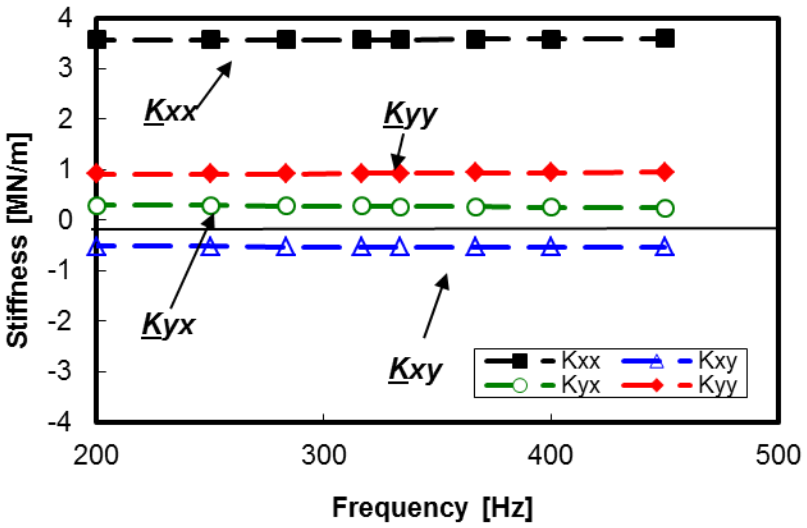

(b) Predicted

Figure 34. Stiffness coefficients versus frequency (a) measured and (b) predicted for a bearing with 50 μm shims. Specific load 27 kPa. Experimental displacement amplitude~ 20μm. Results for journal rotation (50 krpm) and a static load W/LD ~14.3 kPa. Predictions are carried out for a static load W/LD ~ 27.3 kPa.

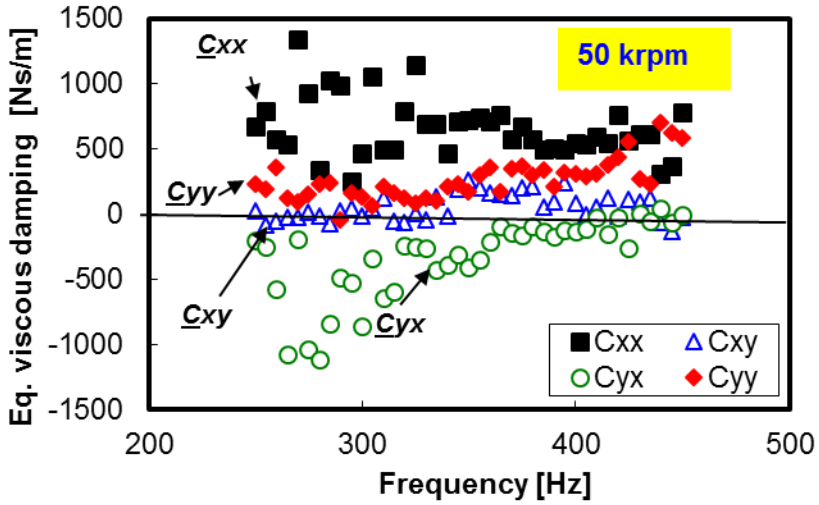

(a) Experimental

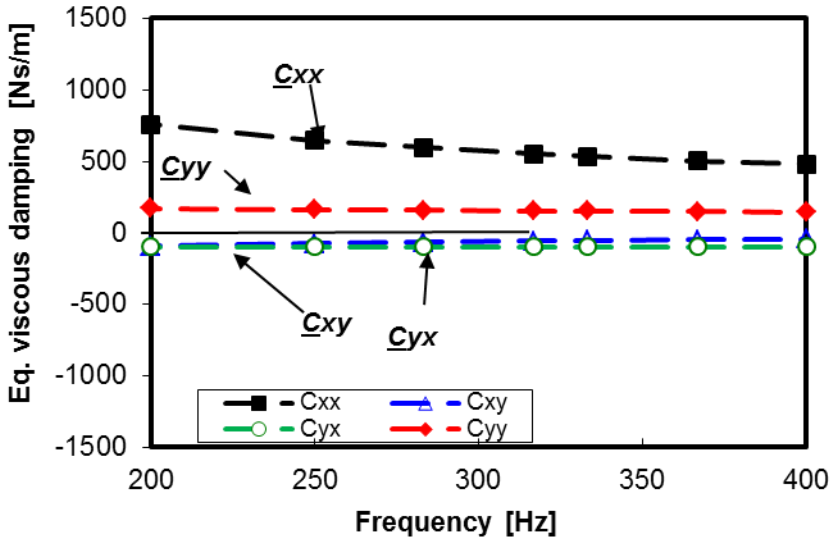

(b) Predicted

Figure 35. Damping coefficients versus frequency (a) measured and (b) predicted for bearing with 50 μm shims. Net static load ~ 20 N. Displacement amplitude~ 20μm. Results with journal rotation (50 krpm). Results for sine sweep loads of 200-450Hz and a static load W/LD ~14.3 kPa. Predictions are carried out for a static load W/LD ~ 27.3 kPa.

Ultimately, the model does, at best, a modest and imprecise job of predicting the force coefficients of a bearing (with a large clearance), with and without shims.

Figure 36 show the predicted gas pressure fields for a bearing in multiple shim configurations (i.e., with and without shims) and Figure 37 shows the dimensionless gas film pressure (P/Pa) at the bearing centerline versus angular location. Note how the presence of the shims changes the pressure gas pressure field in the BFB. The peak dimensionless pressure (P/Pa) increases (by 20%) with shim thickness due to the decrease in the clearance (c). The pressure in the original bearing drops to ambient at 230°. Note emergence of significant pressures at angular coordinates <230°, for the bearings with shims. Also note that the bearing with 50 μm shims has a steeper, narrower (occurring over a shorter angular distance) peak pressure at the bearing centerline than either the original bearing or the bearing with 30 μm shims.

Recall that the bearing force coefficients are proportional to the integration of the hydrodynamic gas pressure over the bearing surface area. Interestingly enough, each gas film pressure field (for shimmed bearings) is different, leading to force coefficients that do not vary monotonically with respect to shim thickness.

More importantly recall that the shimmed bearings, contain three equally spaced shims. As a result of the shims, the bearing has three locations of significantly reduced clearance. The minimum film thickness, or reduced clearance, typically identifies the location of more pressure generation in gas foil bearings [1]. The current bearing does not show three regions of increased pressure generation due to the shims. The bearing with the thickest shims (50 μm) only shows two regions of increased pressure generation. Indeed the large clearance causes much of the bearing not to produce significant pressure. Significant pressure is only generated near the load direction.

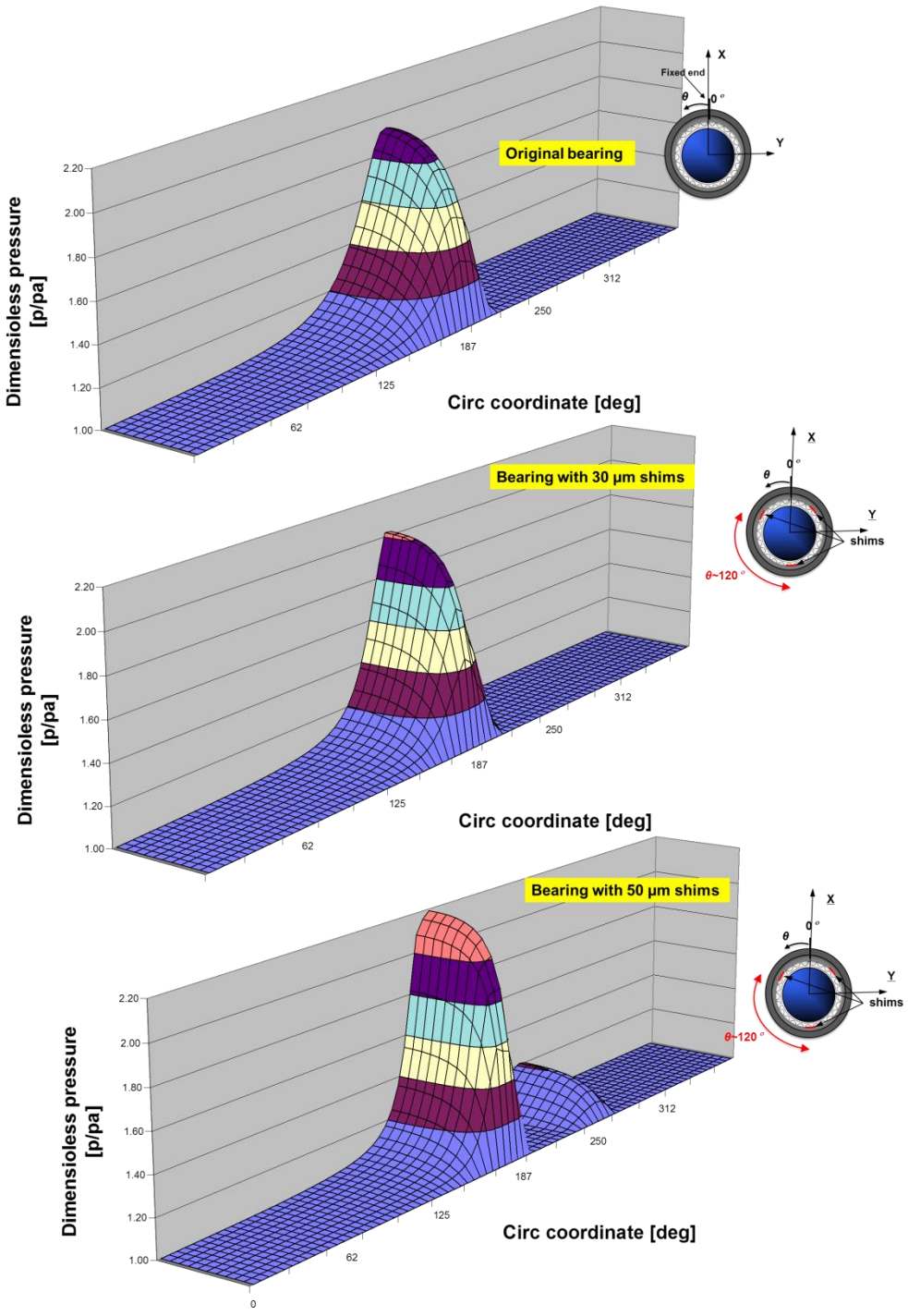

Figure 36. Predicted dimensionless pressure (*P/Pa*) field for a bearing without and and with shims (30 µm and 50 µm thick). Specific load ~ 27 kPa in the *X* axis

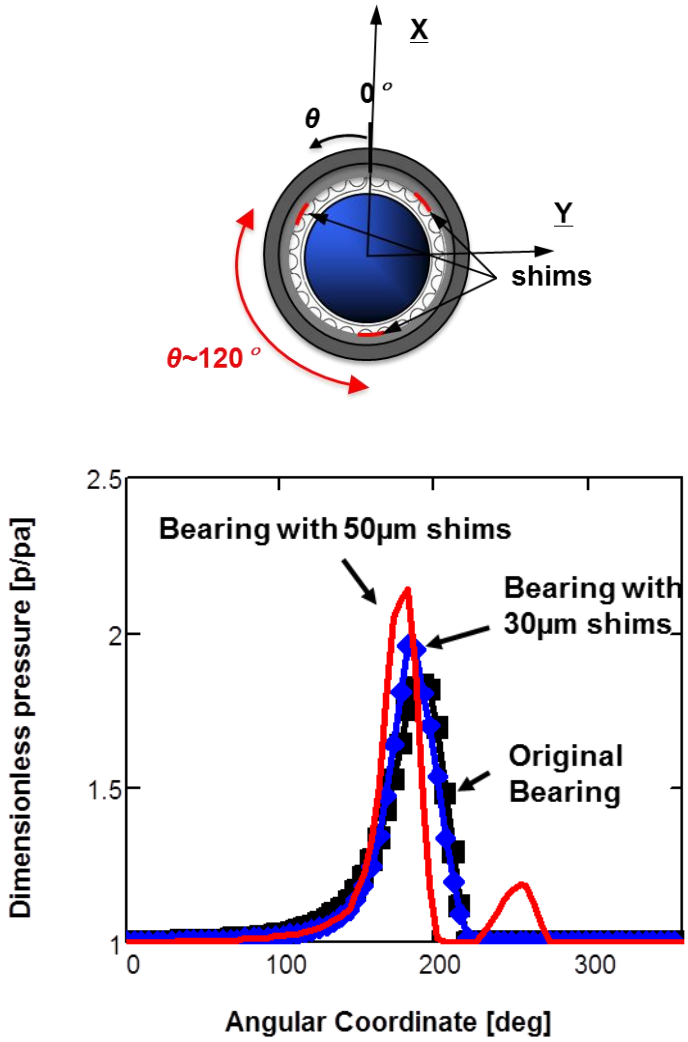

Figure 37. Predicted dimensionless pressure (P/Pa) at the bearing midplane along the circumferential coordinate. Results for a bearing without and with shims (30 µm and 50 µm). Specific load of 27 kPa in the *X* axis.

Waterfall Plots of the TC Journal Vibration

Two eddy current sensors placed as shown in Figure 38 enable the measurement of the BFB response relative to the rotating journal at a constant speed (Ω~50 krpm) for a bearing with and without shims via. The TC journal is manually accelerated to 50 krpm. Rotor vibration are recorded for all three regimes of rotor operation (startup, constant speed, and coast down) however only rotor vibration at a constant speed hold meaningful data.

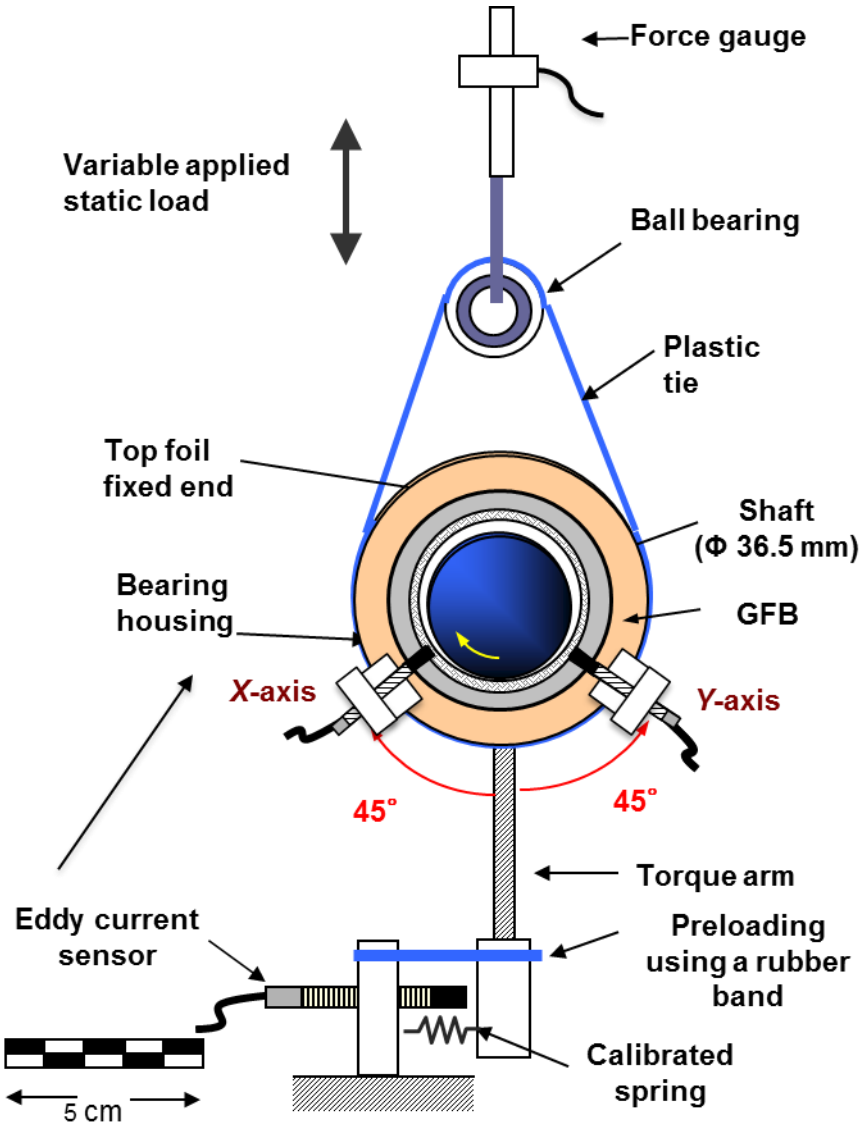

Figure 38. Schematic view of the test rig used to measure bearing drag torque and rotor vibration.

Figure 39 shows the waterfall plots of the rotor vibration for the original bearing and the same bearing with shims under a static vertical load, *W/LD*~0 kPa. The vibration amplitude upon rotor acceleration (run up and coast down) is small, however at a constant speed (~50 krpm) both synchronous and subsynchronous vibration amplitudes persist. Note also that the subsynchronous vibration amplitudes are much larger than the synchronous amplitudes and persist at ~200 Hz and are associated to rotor whirl. The whirl frequency ratio (WFR~ω_s/Ω_s) for the bearing without shims based on the waterfall plots of the rotor response is ~ 0.25. Note that ω_s is the whirl excitation frequency and Ω_s is the journal rotation frequency.

The subsynchronous vibration amplitudes (at 200 Hz) of the TC shaft when supported on the bearing with 30 μm shims are halved, while the synchronous response doubles. This result is likely due to the short duration over which the shaft maintains a constant speed 50 krpm. Indeed shaft acceleration may ameliorate the vibration amplitudes. The bearing with 50 μm shims shows no subsynchronous whirl motion, and indeed the synchronous response is less than when the shaft is supported on the bearing with 30 μm shims. Despite no significant change in the bearing stiffness, and the large nominal clearance (120 μm), the bearings with shims successfully reduce the subsychronous whirl motions exhibited by the TC shaft.

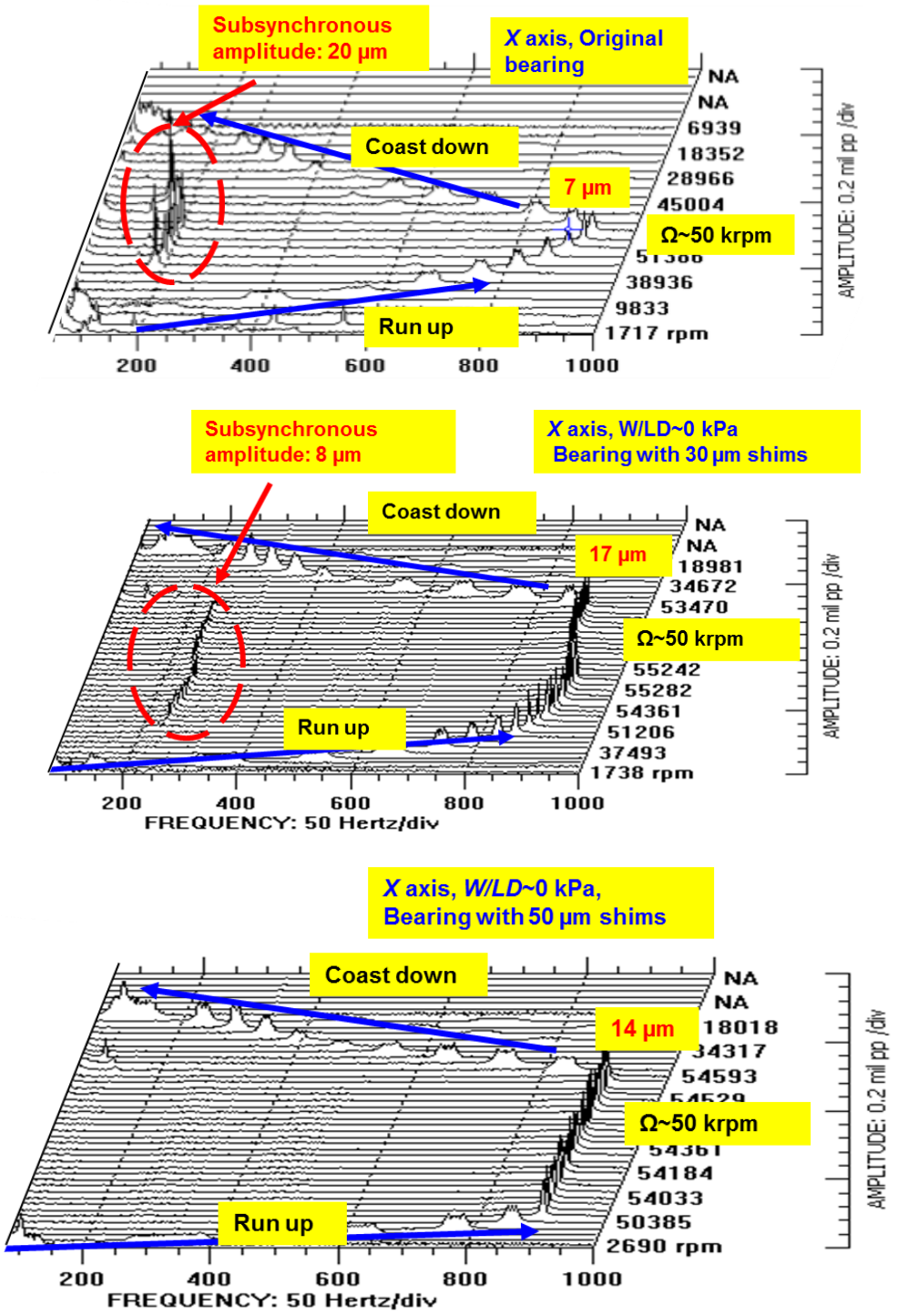

Figure 39. Waterfall plots of the rotor vibration for the (top) original bearing, (middle) a bearing with 30 µm and (bottom) 50 µm shims,(*W/LD* ~0 kPa).

Conclusions

In conclusion, this report provides an experimental assessment of the performance of a shimmed BFB (*L*=38.1 mm, *D*= 36.5mm). The bearing is tested with two shim configurations featuring shims of thickness 30 μm and 50 μm. Two types of experiments are conducted on the test bearing; measurements of drag torque from rotor startup (where dry friction sliding is prevalent) to bearing lift off, to full gas film airborne operation, and estimation of frequency dependent force coefficients (with and without journal speed and with a static specific load of 14.3 kPa acting against gravity). The analysis brings to light design characteristics, such as the shim thickness to clearance ratio, which may affect the BFB force coefficients. The major observations derived from the analysis of the results are:

From drag torque measurement of a bearing without shims,

(a) The *breakaway* friction factor (*f=T/(RW)*) decreases for *W/LD* <20 kPa and subsequently remains constant (~0.20) with respect to *W/LD* (see Figure 8).

(b) The friction factor derived from the startup drag torque of the bearing without shims is ~0.30 and changes little with increasing specific load (*W/LD*) (see Figure 14).

(c) Measurements of the start up friction factor (with journal rotation), and derivation of the friction factor agree reasonably well with the friction factor derived from the *breakaway* torque using a calibrated torque screwdriver for low loads. However at high loads (*W/LD*=20 kPa) the friction factor upon rotor startup is 30% higher than the *breakaway* friction factor. The discrepancy is likely related to top foil wear (see Figure 12).

(d) The rotor lift off speed increases linearly with specific load (*W/LD*) (see Figure 13).

From drag torque measurement of a shimmed bearing,

(e) The bearing friction factors derived from both the peak start up torque and the *breakaway* torque increase up to 40% for bearings with shims (up to a 50μm shim thickness (see Figure 13).

(f) The lift off speed for the bearing with 30 μm shims is lower than that of the original bearing while the lift off speed for the bearing with 50 μm shims is higher than that of the original bearing for all specific loads (see Figure 14).

(g) The friction factor (while airborne) of the shimmed bearings is within 15% (at *W/LD*~20 kPa) of the friction factor for the original bearing. Interestingly, the difference between the friction factor of the shimmed bearings and the original bearing decreases as the specific load increases (*W/LD*) (see Figure 15).

(h) Ultimately, adding a mechanical preload through shimming increases the bearing friction factor upon a rotor speed startup procedure, hence leading to higher drive torque requirements and an increased power loss (see Figure 14).

From the force coefficients of a bearing with and without shims with a 14.3 kPa load (flexibly applied)

(a) The force coefficients (stiffness and damping) slightly decrease for operation with journal speed due to the two spring elements being in series (bump foil stiffness and gas film stiffness).

(b) The results unanimously show that the stiffness of a BFB without shims is approximately equal to a BFB with shims. However the direct damping increases slightly with shim thickness.

(c) The bearing loss factor (γ~0.38-0.48) changes little with shim thickness and rotor speed.

(d) Shimming ultimately isn't a straight forward procedure to increase the force coefficients. External conditions like static load, and excitation frequency affect the BFB force coefficients more than the shim thickness. However note that the shim thicknesses (t_s) are quite small with respect to the bearing clearance (c) (t_s/c~0.13, and 0.21). Future research should focus on experimental force coefficient identification of shimmed bearings with $t_s/c > 0.50$.

References

[1] DellaCorte, C., 2011, "Stiffness and Damping Coefficient Estimation of Compliant Surface Gas Bearings for Oil-Free Turbomachinery," STLE Tribol. Trans., **54** (4), pp.674-684.

[2] Chen, H.M., Howarth, R., Geren, B., Theilacker, J.C., and Soyars, W.M., 2001, "Application of Foil Bearings to Helium Turbocompressors," Proceedings Of 30th Turbomachinery Symposium, Houston, TX.

[3] DellaCorte. C., Radil, K.C., Bruckner, R.J., and Howard, S.A., 2008, "Design, Fabrication, and Performance of Open Source Generation I and II Compliant Hydrodynamic Gas Foil Bearings," STLE Tribol. Trans., **51**, pp. 254-264.

[4] Kim, T. H., and San Andrés, L., 2009, "Effects of a Mechanical Preload on the DynamicForce Response of Gas Foil Bearings - Measurements and Model Predictions," STLE Tribol. Trans., **52**, pp. 569-580.

[5] Lee, Y-B., Suk, B.K., Kim, T.H., and Sim, K., 2013, "Feasibility of an Oil-Free Turbocharger Supported on Gas Foil Bearings via On-Road Tests of a Two-Liter Class Diesel Vehicle," ASME J. Eng. Gas Turbines Power, **135**, p. 052701-1.

[6] Sim, K., Lee, Y-B., Kim, T.H., and Jangwon L., 2012,"Rotordynamic Performance of Shimmed Gas Foil Bearings for Oil-Free Turbochargers", ASME J. Tribol.,**134**, p. 031102.

[7] Blok, H., and van Rossum, J. J., 1953, "The Foil Bearing – A New Departure In Hydrodynamic Lubrication," Lubr. Eng., December, pp. 316-320.

[8] Heshmat, H., Shapiro, W., and Gray., S, 1982, "Development of Foil Journal Bearings for High Load Capacity and High Speed Whirl Stability" ASME J. Tribol., 104, pp. 149-156.

[9] Heshmat, H., 1994, "Advancements in the Performance of Aerodynamic Foil Journal Bearings: High Speed and Load Capacity," ASME J. Tribol., 116, pp. 287 - 295.

[10] Bruckner, R.J., and Puleo, B.J., 2008, "Compliant Foil Journal Bearing Performance at Alternate Pressures and Temperatures," ASME Paper No. GT2008-50174.

[11] DellaCorte, C, and Valco, M., 2000, "Load Capacity Estimation of Foil Air Journal Bearing for Oil-Free Turbomachinery Applications," STLE Tribol. Trans., **43**(4). pp. 795-801.

[12] DellaCorte, C., and Bruckner, R., 2011, "Remaining Technical Challenges and Future Plans for Oil-Free Turbomachinery" ASME J. Eng. Gas Turbines Power, **133**, p. 042502-1.

[13] Kim, T.H., Breedlove, A.W., and San Andrés, L., 2009, "Characterization of a Foil Bearing Structure at Increasing Temperatures: Static Load and Dynamic Force Performance," ASME J.Tribol., **131**, p. 041703-1

[14] Rubio, D., and San Andrés, L., 2006, "Bump-Type Foil Bearing Structural Stiffness: Experiments and Predictions," ASME J. Eng. Gas Turbines Power, **128**, pp. 653-660.

[15] Rubio, D., and San Andrés, L., 2007, "Structural Stiffness, Dry-Friction Coefficient and Equivalent Viscous Damping in a Bump-Type Foil Gas Bearing" ASME J. Eng. Gas Turbines Power, **129**, pp. 494-502.

[16] Iordanoff, I., 1999, "Analysis of an Aerodynamic Compliant Foil Thrust Bearing: Method for a Rapid Design," ASME J. Tribol., **121**, pp. 816–822.

[17] Matta, P., Arghir, M., and Bonneau, O., 2009, "Experimental Analyses of a Cylindrical Air-Bearing Dynamic Coefficients," STLE Tribol. Trans., **53**,pp. 329- 339.

[18] Rudloff, L., Arghir, M., Bonneau, O., and Matta, P, 2011, "Experimental Analyses of a First Generation Foil Bearing: Startup Torque and Dynamic Coefficients," ASME J. Eng. Gas Turbines Power, **133**, p. 092501.

[19] Chirathadam, T. A., and San Andrés, L., 2012, "A Metal Mesh Foil Bearing and a Bump- Type Foil Bearing: Comparison of Performance for Two Similar Size Gas Bearings," ASME J. Eng. Gas Turbines Power, **134**, p. 102501.

[20] Conlon, M.J., Dadouche, A., Dmochowski, W.D., and Bédar, J.-P., 2010, "A Comparison of the Steady-State and Dynamic Performance of First- and Second Generation Foil Bearings," ASME Paper No. GT2010-23683.

[21] Radil, K.C., and DellaCorte, C., 2009, "A Three-Dimensional Foil Bearing Performance Map Applied to Oil-Free Turbomachinery," STLE Tribol. Trans., **53**, pp.771- 778.

[22] Kim, T.H., and San Andrés, L. 2008, "Forced Nonlinear Response of Gas Foil Bearing Supported Rotors", Tribol. Int., **41**,pp 704-715.

[23] Kim, T.H., Rubio, D., and San Andrés, L., 2007, "Rotordynamic Performance of a Rotor Supported on Bump Type Foil Gas Bearings: Experiments and Predictions," ASME J. Eng. Gas Turbines Power, **129**, pp. 850-857.

[24] Schiffmann, F., and Spakovszky, Z.S., 2013, "Foil Bearing Design Guidelines for Improved Stability," ASME J.Tribol., **135**, p.011103

[25] Sim, K., Koo, B., Lee, J.S., and Kim, T.H., 2014,"Effects of Mechanical Preload on the Rotordynamic Performance of a Rotor Supported on 3 Pad Gas Foil Bearings", ASME Paper No. GT2014-25849

[26] San Andrés, L., and Norsworthy, J., 2013,"Identification of Structural Stiffness and Material Loss Factor in a Shimmed (Generation One) Bump-Type Foil Bearing," TRC-B&C-04-13, Annual Progress Report to the Turbomachinery Research Consortium, May.

[27] Chirathadam, T.A., 2012, "Metal Mesh Foil Bearings: Prediction and Measurement of Static and Dynamic Performance Characteristics," Ph.D Thesis, Texas A&M University, College Station, TX.

[28] Chirathadam, T. A., Kim, T.H, Ryu, K., and San Andrés, L., 2010, "Measurements of Drag Torque, Lift-Off Journal Speed and Temperature in a Metal Mesh Foil Bearing," ASME J. Eng. Gas Turbines Power, **132**(11), p. 112503.

[29] James, J. F., 2002, *A Student's Guide to Fourier Transforms; With Applications in Physics and Engineering* , Cambridge, New York, pp. 2-8.

[30] Kim, T.H., and San Andrés, L., 2008, "Heavily Loaded Gas Foil Bearings: A Model Anchored to Test Data," ASME J. Eng. Gas Turbines Power, **130**, p.012504.

Appendix A: Drag Torque of the TC Ball Bearings

The drag torque from the ball bearings is identified for increasing static vertical loads prior to measuring the *breakaway* torque of the BFB. Figure A.1 shows a schematic view of the test rig used to measure the drag torque of the TC ball bearing.

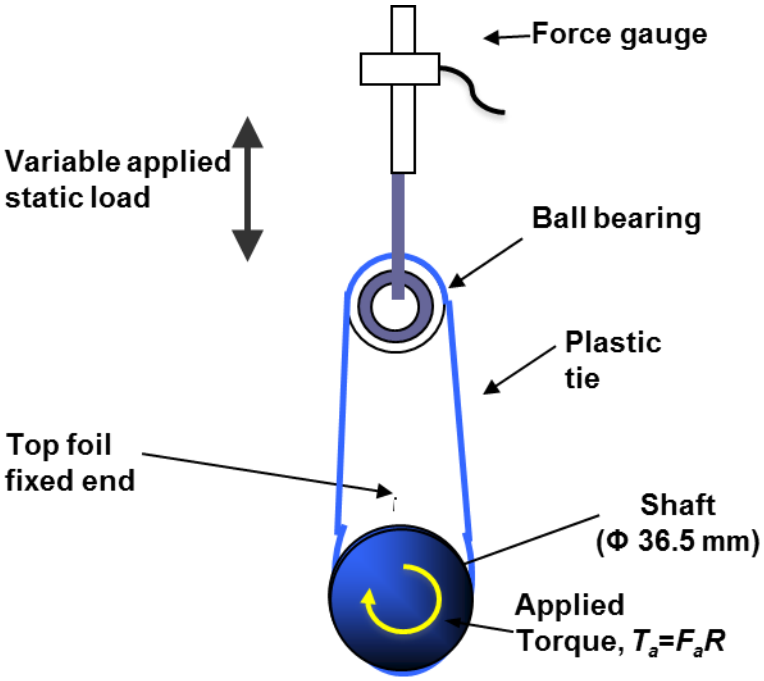

Figure A 1. Schematic view of the test rig to measure the TC ball bearing drag torque. Torque is applied to the TC shaft via a torque screwdriver

Figure A.2 presents the drag torque of the TC ball bearing versus static vertical load. The TC ball bearing drag torque increases linearly with static load. The presence of lubricant flow has a minimal effect on the drag torque of the TC ball bearing. During operation only a small amount of lubricant (at ambient temperature ~22°C) flows through the ball bearing, hence a small amount of lubricant does not affect the TC ball bearing drag torque. Also note that the highest load applied to the test bearing is 20 N thus the maximum ball bearing drag torque is <10 N-mm.

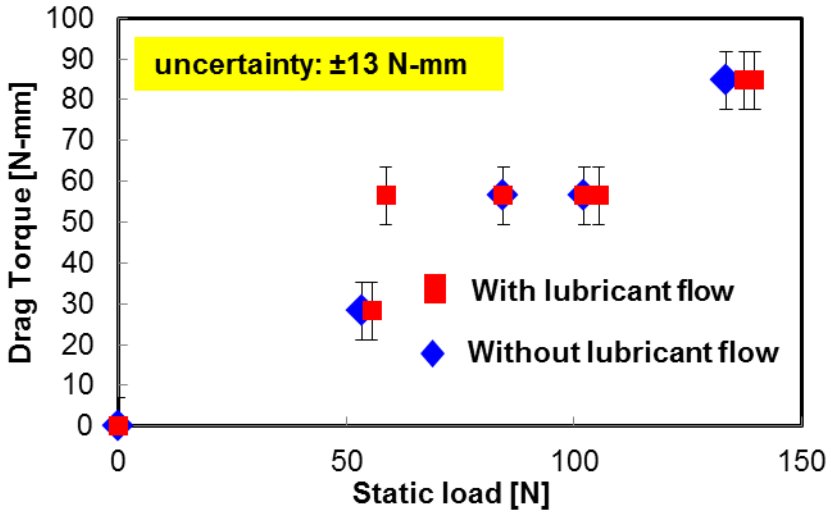

Figure A 2. TC ball bearing drag torque versus static vertical load with and without oil lubricant flow. Uncertainty ±28 N-mm.

Appendix B: Post Test Equipment Inspection

100 start stop cycles are conducted on the rotor bearing system discussed in the main text. As previously discussed, wear on the rotor outer surface and bearing inner surface occurs due to rubbing between bearing and rotor surfaces upon start up and shut down. Figure B.1 shows pictures of the rotor and bearing surfaces before and after ~100 cycles of rotor start and stop. The rotor outer surface and bearing inner surface show wear from abrasion. The bearing suffers the most wear at the location where the static load forces the bearing and rotor to be in contact, which happens to be the location of the minimum film thickness, and the highest stiffness.

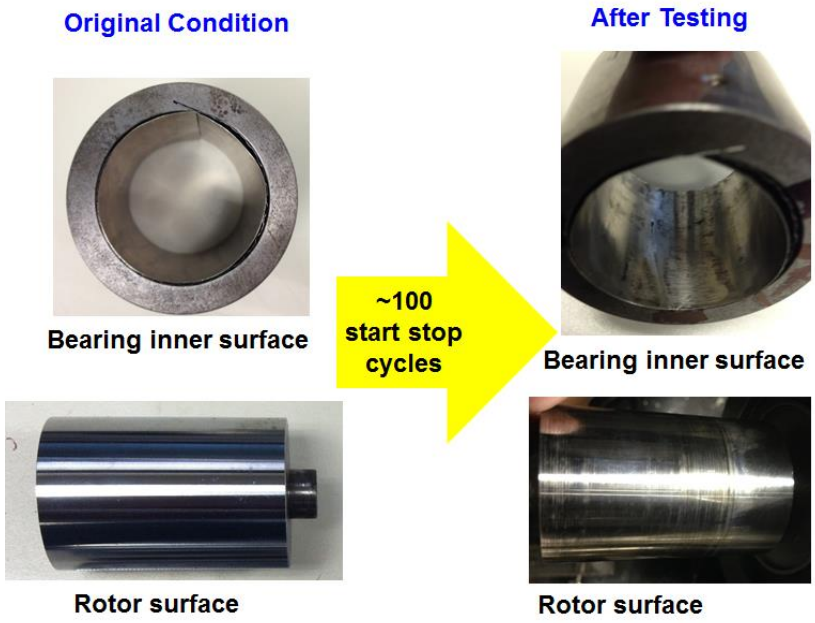

Figure B 1. Photographs of the bearing and rotor inner surfaces before and after ~100 cycles of rotor start and stop

Appendix C: Uncertainty and Variability

This section outlines the calculation of uncertainty and discussion of variability in the drag torque measurements and the experimentally identified BFB force coefficients. The instrument uncertainty of the accelerometers, load cells, and eddy current sensors is 1% linearity.

Uncertainty in the drag torque measurements

The uncertainty in drag torque ($T=\delta K_s L_T$) measurements is due to the uncertainty in the measurement of position (δ), the spring stiffness (K_s), and the measurement of the torque arm (L_T). The torque arm is measured with calipers, uncertainty~ ±.0001mm (U_L). The uncertainty in the position measurement is ±0.70 µm (U_x). The spring stiffness is estimated from load deflection tests. The spring stiffness is identified as the slope of the load deflection curve, which is linear. The uncertainty in the spring stiffness is (±0.33 N/mm). The Cline-McClintock method of evaluating measurement uncertainty delivers a general uncertainty formulation for a function of multiple variables ($r=f(x_1, x_2,\ldots\ldots,x_n)$). The general equation for the uncertainty of a function with multiple variables is

$$Ur = \sqrt{\left(\frac{\partial r}{\partial x_1}U_{x_1}\right)^2 + \left(\frac{\partial r}{\partial x_2}U_{x_2}\right)^2 + \ldots + \left(\frac{\partial r}{\partial x_n}U_{x_n}\right)^2} \qquad \text{(E.1)}$$

Using the above equation, the uncertainty of the drag torque (U_T) is identified from the following equation.

$$\left(\frac{U_T}{T}\right)^2 = \left(\frac{U_x}{x}\right)^2 + \left(\frac{U_K}{K}\right)^2 + \left(\frac{U_{L_T}}{L_T}\right)^2$$

From this equation the uncertainty in the measured drag torque is ±1 N-mm.

Variability in the drag torque measurements

Drag torque measurements are conducted for a bearing with i) no shims and ii) with shims (30µm, and 50µm). The bearing drag torque is recorded for rotor speeds up to 50 krpm. To determine the variability of the drag torque measurements, at least three tests are conducted for each test condition (static load, and shim thickness). Figure C.1 shows the drag torque results and their variability for three tests for a bearing with and

without shims (*W/LD*~0 kPa). The variability of the drag torque measurements prior to lift off (< 20 krpm) is difficult to access, however the variability of the drag torque measurements after lift off is identified. The maximum variability occurs for test conducted on the bearing with 50 µm shims, ~ 80 N-mm. The drag torque results agree very well between individual tests and show very little variance, thereby demonstrating reliable repeatable results.

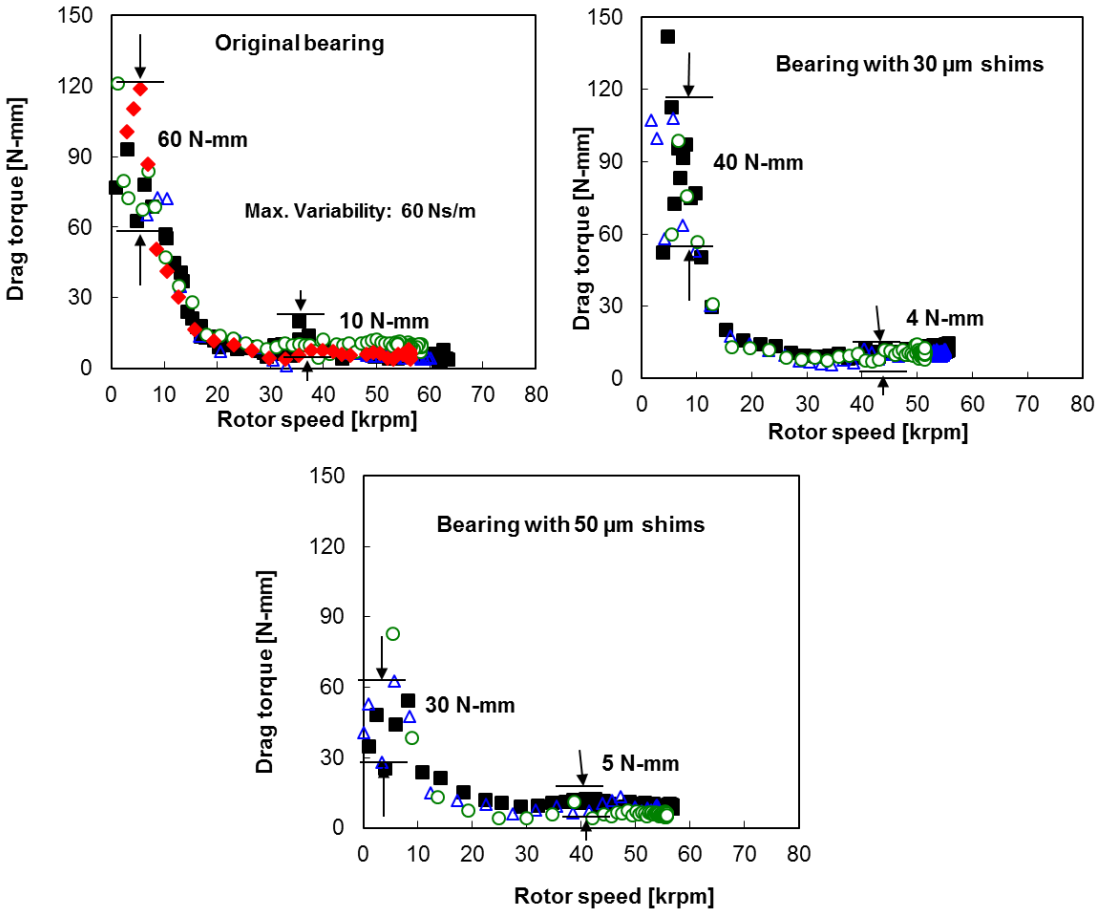

Figure C 1. Bearing drag torque (*T*) versus rotor speed (Ω) for a bearing with and without shims for a static load, *W/LD*~0 kPa. Results for at least three tests are shown

Uncertainty in the force coefficients

The uncertainty analysis of the bearing force coefficients follows a procedure used in Ref. [27]. Uncertainty in the bearing force coefficients arises from the instrumentation uncertainty in the measurements of bearing cartridge acceleration, bearing relative displacement and excitation force. The relationship between the measured signals and the bearing impedances ($H_{\alpha\beta} = K_{\alpha\beta} + j\omega C_{\alpha\beta}$; $\alpha, \beta = X, Y$) in the *X* direction is

$$H_{XX}\bar{x}'^{X} + H_{XY}\bar{y}'^{X} = \bar{G}_X{}^X = \bar{F}_X{}^X - \left(M_{S_X} + {C_{S_X}}/{j\omega} - {K_{S_X}}/{\omega^2} \right) \bar{A}_X{}^X \tag{15}$$

Assuming the uncertainties of the two terms on the left hand side (LHS) of Eqn. are approximately equal, the uncertainty in H_{XX} is computed using Eqn. E.1

$$\left(\frac{U_{H_{XX}}}{H_{XX}} \right) = \frac{1}{\sqrt{2}} \sqrt{ \left(\frac{U_{G_X^X}}{G_X^X} \right)^2 + \left(\frac{U_{\bar{x}'^X}}{\bar{x}'^X} \right)^2 } \tag{E.1}$$

The fractional uncertainties in the dynamic load ($\frac{U_F}{F}$), acceleration ($\frac{U_{A_X}}{A_X} = \frac{U_{A_Y}}{A_Y}$) and the excitation frequency ($\frac{U_\omega}{\omega}$) are less than 0.02, 0.01, and 0.05 respectively. The resulting maximum uncertainty in the stiffness and damping coefficients is ±0.08 MN/m and ± 80 Ns/m, respectively.

Variability in the force coefficients

A minimum of three tests are conducted for each test condition to asses and verify the repeatability of the identification process. Figures C.2 and C.3 show the bearing stiffness and damping coefficients for four repeated tests versus excitation frequency. The tests are conducted on a bearing without shims, with approximately 40N load acting down (with gravity) on the bearing. Also note that these tests correspond to tests with no journal rotation.

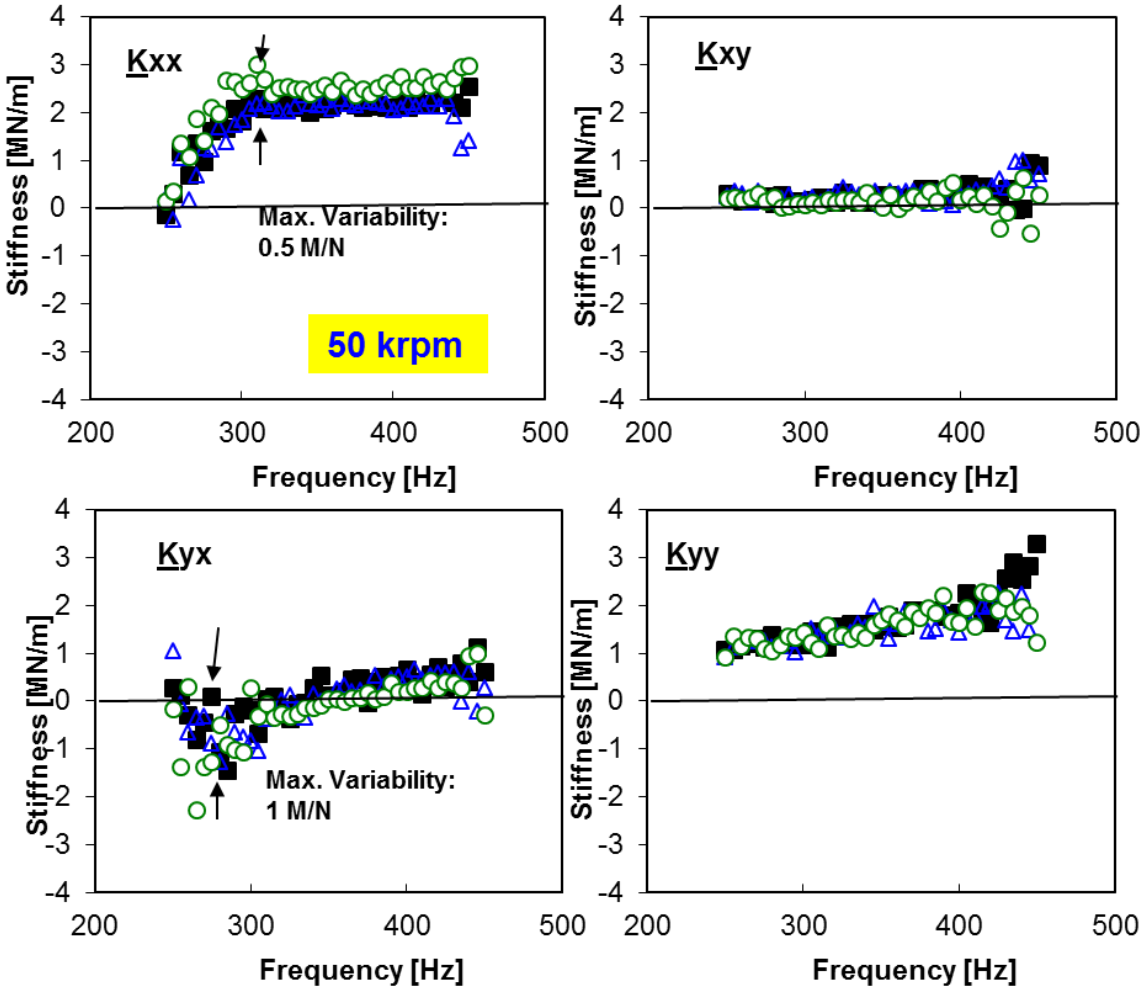

Figure C 2. Test sets 1 – 4: Identified BFB stiffness coefficients ($\underline{K}_{XX}$, $\underline{K}_{YY}$, $\underline{K}_{XY}$,$\underline{K}_{YX}$) versus frequency. Applied static load *W/LD* ~ 14.3 kPa. Journal spinning at 50 krpm.

The maximum variability in the K_{XX}, K_{XY}, K_{YX}, and K_{YY} are 0.4 MN/m, ~0.1 MN/m, 0.2 MN/m and ~ 0 MN/m respectively; while for C_{XX}, C_{XY}, C_{YX}, and C_{YY} are 200 Ns/m, 40 Ns/m, 200 Ns/m and 60 Ns/m, respectively. The test data indicates that there is considerable variability in the identified damping coefficients however the variability in the stiffness coefficients is quite low.

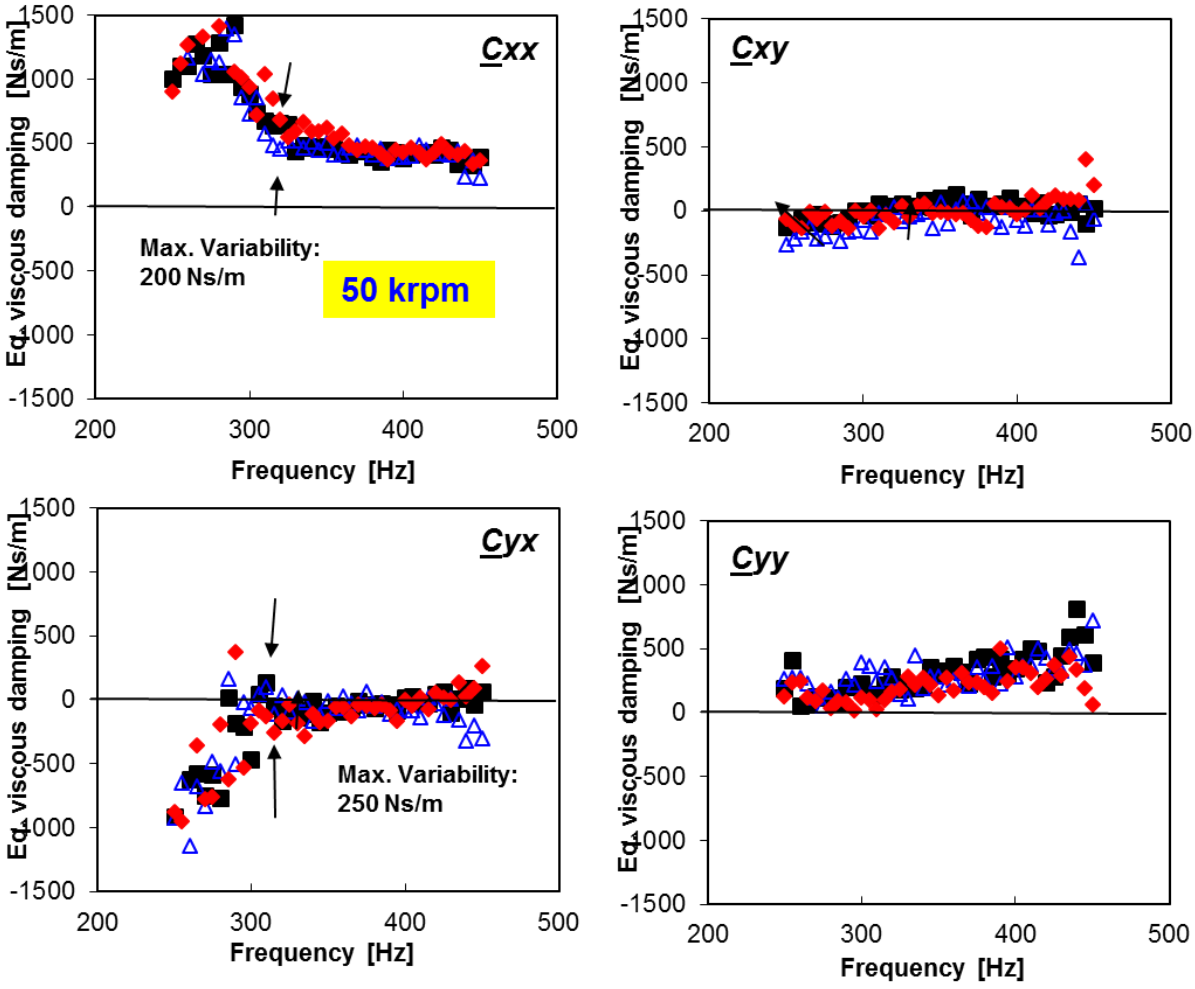

Figure C 3.Test sets 1-4: Identified BFB damping coefficients ($\underline{C}_{XX}$, $\underline{C}_{YY}$, $\underline{C}_{XY}$, $\underline{C}_{YX}$) versus frequency. Applied static load *W/LD* ~ 14.3 kPa. Journal spinning at 50krpm.

Appendix D: Estimation of the Squirrel Cage Structural Parameters

As note previously, the test BFB is held by a soft elastic structure (squirrel cage) comprised of 8 thin steel rods arranged in a circular pattern. The radial stiffness and damping coefficients of the elastic structure must be determined first. Figure D.1 shows a photograph of the squirrel cage and bearing to which impact loads are applied. Note that the bearing is not resting atop the rotor during impact tests.

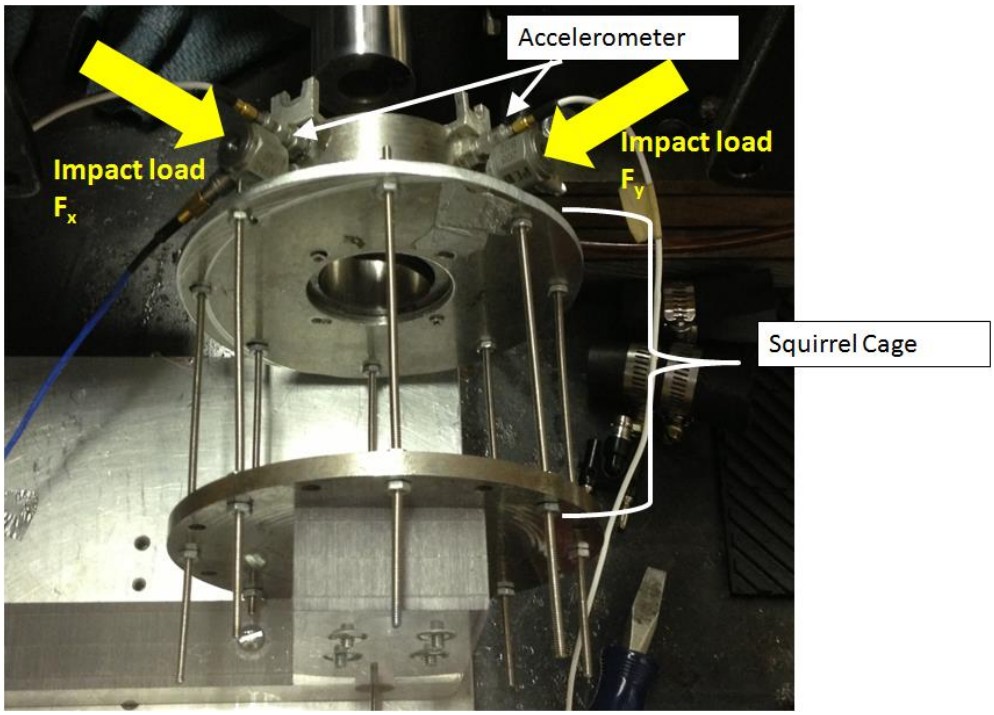

Figure D 1. Top view of the squirrel cage and bearing to be impact tested.

Figure D.2 shows the typical impact excitation loads (F_X, F_Y) exciting the FB and squirrel cage assembly and the resulting FB acceleration in the X and Y directions (a_X, a_Y). The excitations are applied orthogonal to each other. Figure D.3 shows the bearing accelerations in the frequency domain. The results demonstrate a lightly damped system with a natural frequency at ~ 20 Hz. Results also evidence low structural cross coupling.

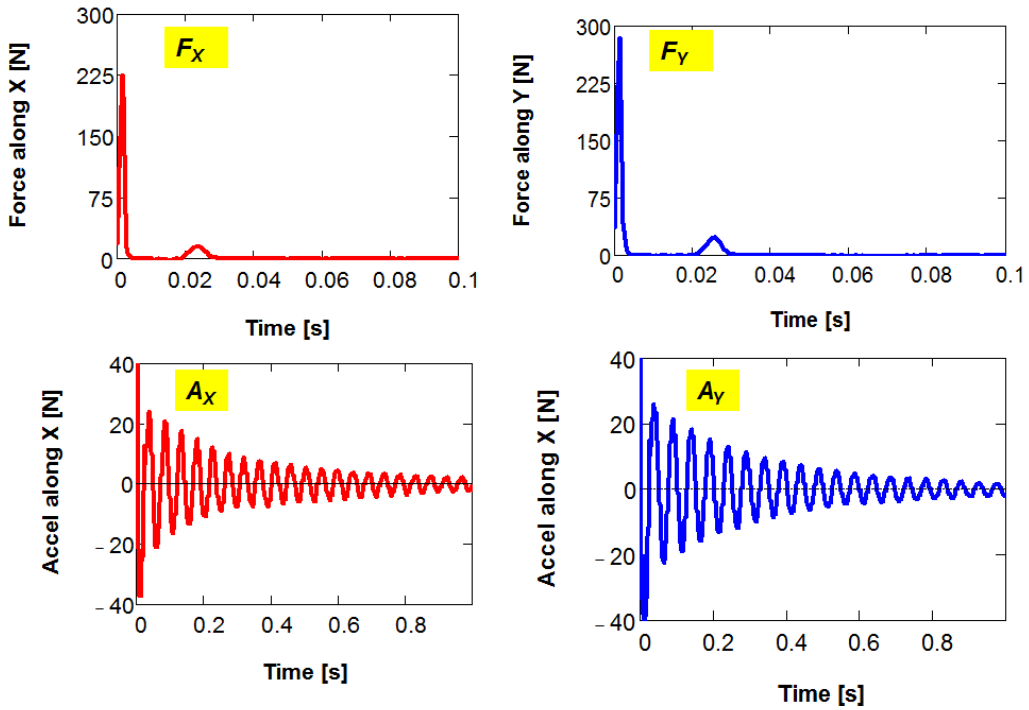

Figure D 2. (top) Impact loads and (bottom) recorded bearing accelerations, *X* and *Y* directions, versus time. No contact with journal.

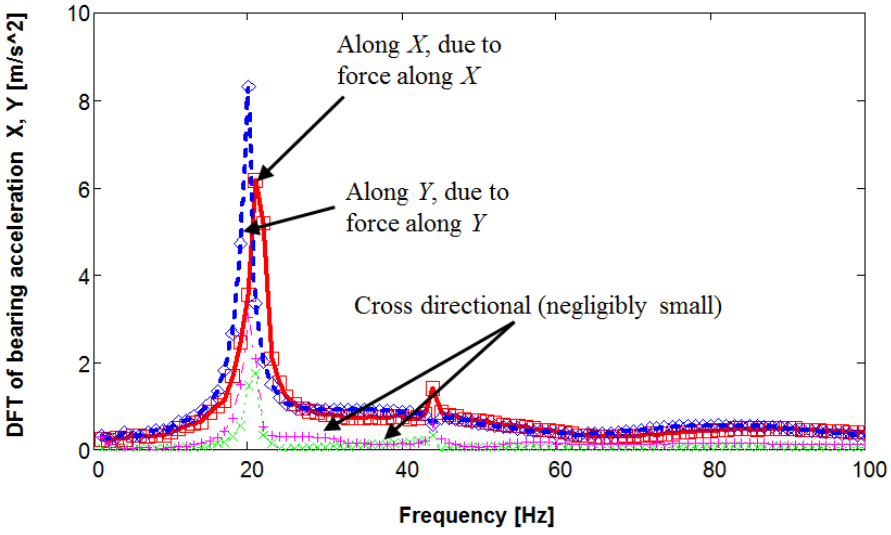

Figure D 3. Discrete Fourier Transform amplitudes of accelerations along *X* and *Y* directions due to impact loads on the bearing and elastic support structure assembly.

Since there is little structural cross coupling, the bearing and elastic structure behave as a single degree of freedom system along each direction. The system is characterized by a system mass (M_S), stiffness (K_S) and viscous damping (C_S) coefficients along each direction (X,Y). The measurements of acceleration and impact load are used to extract the structural parameters according to a nonlinear curve fit of the accelerance function. The accelerance function along the X direction is

$$\left\| \left[\frac{a_{X(\omega)}}{F_{X(\omega)}} \right] \right\| = \frac{\omega^2}{\left\{ \left(K_{S_X} - \omega^2 M_{S_X} \right)^2 + \left(\omega C_{S_X} \right)^2 \right\}^{1/2}} \tag{17}$$

where ω denotes frequency. Figure E.4 shows the recorded accelerance function $\left| a_{X(\omega)} / F_{X(\omega)} \right|$ and its curve fit equation. The identified mass is M_{S_X} = 1.5 kg and includes the mass of the bearing, and the squirrel cage structure moved during excitation. The identified structural stiffness K_{S_X} = 26 kN/m, and the damping coefficient C_{S_X} = 8.2 Ns/m. The goodness to fit is R^2 = 0.92 for the frequency range (0-300Hz).

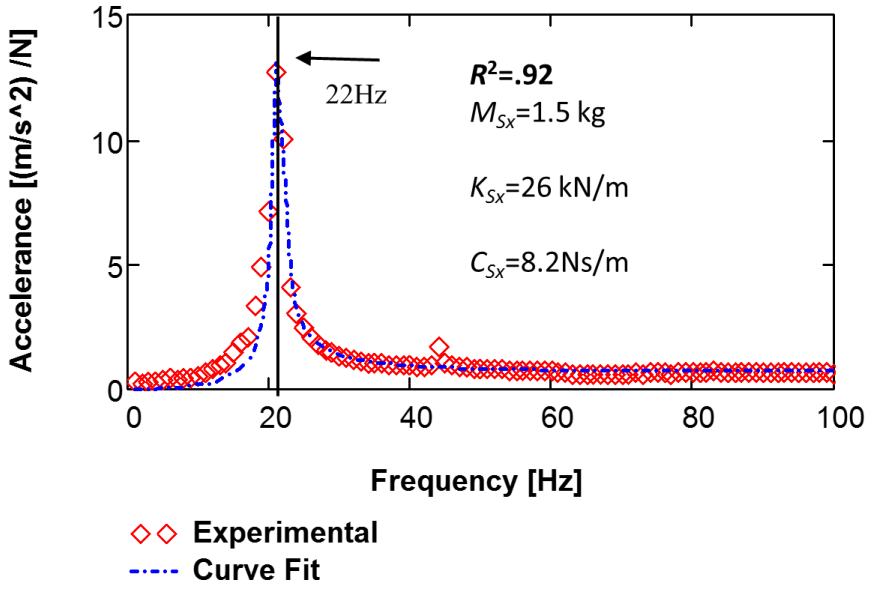

Figure D 4. Accelerance $|a_X/F_X|$ and curve fit to identify parameters of bearing elastic support structure.

Likewise Figure D.5 shows the recorded accelerance function $\left|a_{Y(\omega)}/F_{Y(\omega)}\right|$ and its curve fit equation. The identified parameters include the identified mass is M_{S_Y} = 1.7 kg .The identified structural stiffness K_{S_Y} = 26 kN/m, and damping coefficient C_{S_Y} = 3.2 Ns/m, and the goodness to fit is R^2 = 0.95 for the frequency range (0-300Hz).

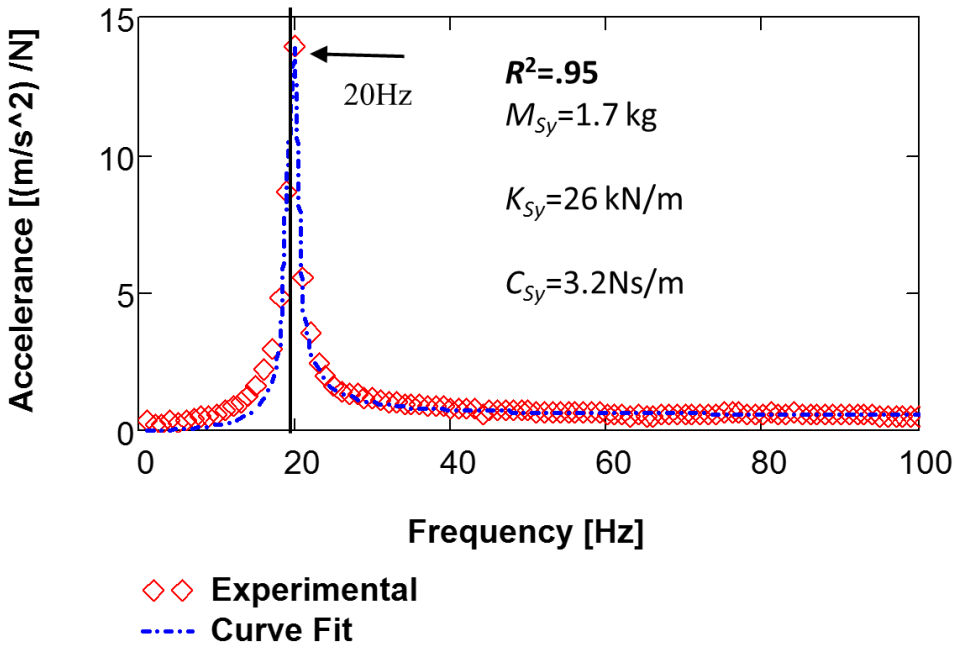

Figure D 5. Accelerance $|a_Y/F_Y|$ and curve fit to identify parameters of bearing elastic support structure.

The identified bearing structural coefficients along *X* and *Y* directions, listed in Table F.1, are similar however the system is not isotropic. The uncertainty in the identified parameters is due to the uncertainties in the load cell (1% linearity), and accelerometer (1% linearity). The variability (among three independent tests) in the K_{S_Y}, C_{S_Y} M_{S_Y} is 3.9 kN/m, 2 Ns/m, and 0.1kg respectively. The variability in K_{S_X}, C_{S_X}, M_{S_X} is 6kN/m, 1.9 Ns/m, 0.2kg respectively (also among three independent tests). The mass of the bearing as measured from a scale is 1.2kg. Note that the damping ratios identified are quite small especially for along the *Y* direction.

Table D 1. Measured Mechanical parameters for bearing and elastic support structure

	Y direction	*X* direction	
Stiffness, K_S	26±2	24±3	kN/m
Mass, M_S	1.7±0.1	1.5±0.05	kg
Damping, C_S	3.2±1	8.2±1	N.s/m
Natural frequency	20±0.5	22±0.5	Hz
Damping ratio	0.01	0.021	-
R^2	0.92	0.95	-

Appendix E: Measurements of BFB acceleration and displacement with rotor speed (50 krpm)

Figures E.1 through E.3 show the bearing motions (time and frequency domain bearing relative displacements and frequency domain bearing absolute accelerations) versus excitation frequency for tests conducted on a bearing without shims under a specific load *W/LD*~14.3 kPa and for journal operation at 50 krpm.

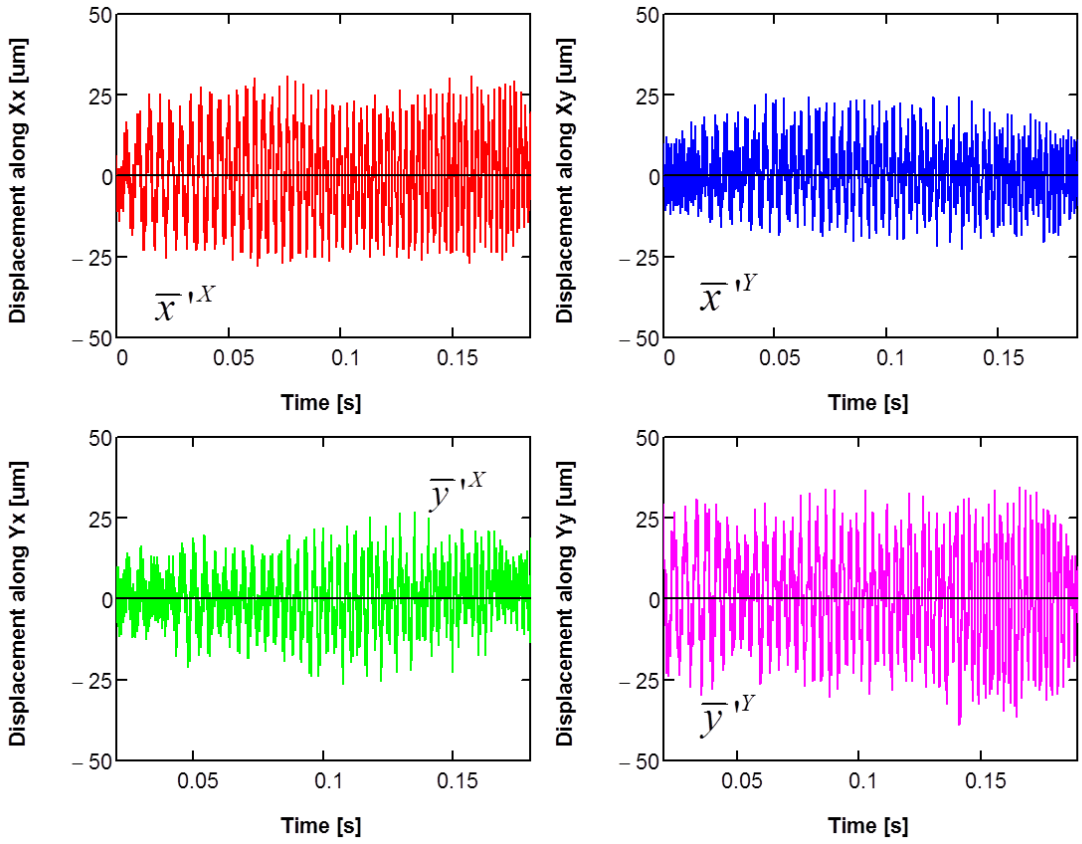

Figure E 1. Direct (top) and cross directional (bottom) bearing relative displacements along *X* and *Y* directions. Applied specific load W/LD~ 14.3 kPa. Journal spinning at 50 krpm

The direct bearing displacements are maintained at ~ 20 µm across the excitation frequency. The cross coupled bearing displacements are ~10 µm.

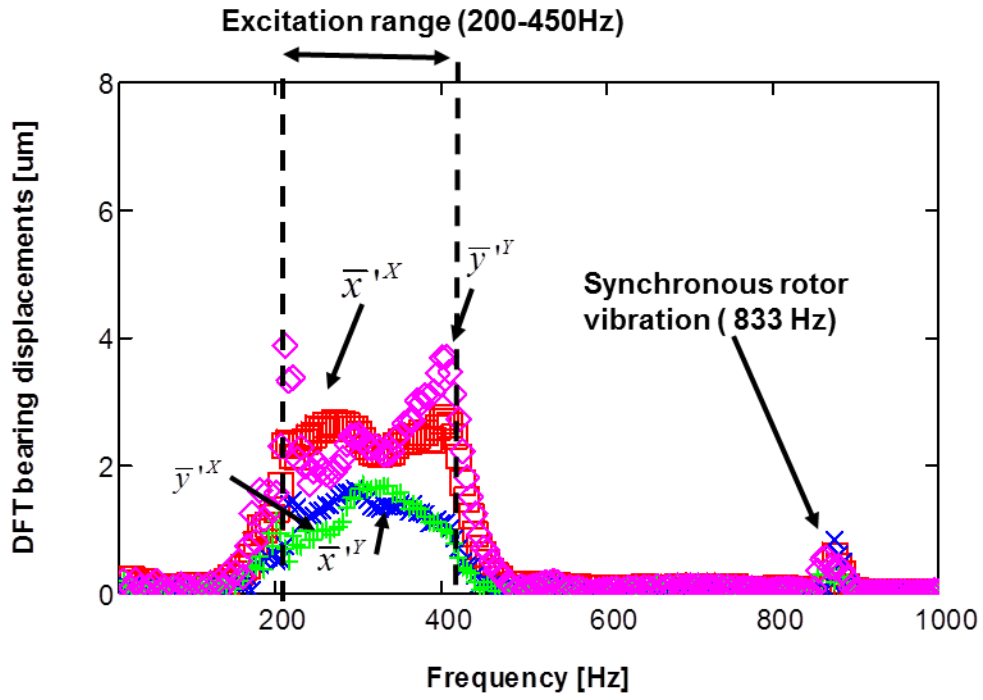

Figure E 2. Average DFT amplitude of bearing displacements versus frequency. Sine sweep 200-400Hz. Average of 10 excitations. Rotor speed ~ 50 krpm. Specific load ~ 14.3 kPa

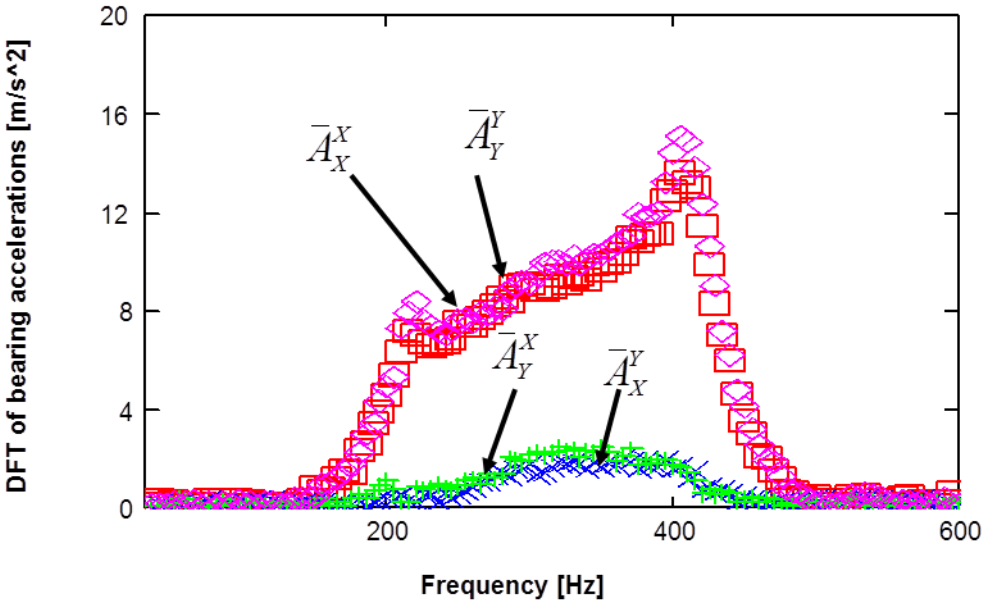

Figure E 3. Average DFT amplitude of bearing absolute accelerations versus frequency. Sine sweep 200-400Hz. Average of 10 excitations. Rotor speed ~ 50 krpm. Specific load of 14.3 kPa.